

# Strong Hydrogen Bonds in Anion-Solvent Clusters: Structural and Thermochemical Properties

by

Robert John Nieckarz

A thesis  
presented to the University of Waterloo  
in fulfillment of the  
thesis requirement for the degree of  
Doctor of Philosophy  
in  
Chemistry

Waterloo, Ontario, Canada, 2008

© Robert John Nieckarz 2008

## **Author's Declaration**

I hereby declare that I am the sole author of this thesis. This is a true copy of the thesis, including any required final revisions, as accepted by my examiners.

I understand that my thesis may be made electronically available to the public.

## Abstract

Insight into the effect of secondary interactions, fluorination, as well as substituent effects on strong ionic hydrogen bonds has been acquired through studies of  $\text{FHF}^-$ ,  $\text{NF}_n\text{H}_{3-n}\cdots\text{F}^-$  ( $n = 0..2$ ) and  $[\text{M}-\text{H}]^-$  ( $\text{M} = \text{Glycine, Alanine, Valine, Serine}$ ) clustered with  $\text{ROH}$  ( $\text{R} = \text{H, CH}_3, \text{C}_2\text{H}_5$ ). Excellent agreement was observed between thermochemical values obtained from high pressure mass spectrometry measurements and those predicted from MP2(full)/6-311++G(d,p)//B3LYP/6-311++G(d,p) calculations.

In the examination of the clustering of  $\text{FHF}^-$ , a strong correlation between the hydrogen bond strength and the gas phase acidity of the solvent was observed. In addition, several interesting observations on various structural and thermochemical properties were made for each of the three solvents. Upon formation of clusters with water, it was found that the large entropic advantage of one particular structure, which was not the most enthalpically favored, was significant enough to make it the predominant species within the ion source. In the case of methanol solvation, no evidence of secondary interaction of the methyl group and any other moiety could be found. The structural details revealed from calculations of the ethanol-solvated clusters indicate that secondary interactions between the terminal methyl group and  $\text{FHF}^-$  had an impact on the length of both the FHF and OHF bonds present.

In an attempt to gain insight into the effects of fluorination on hydrogen bonding, clusters of  $\text{NF}_n\text{H}_{3-n}$  ( $n = 0..2$ ) and  $\text{F}^-$  have been computationally investigated. The hydrogen bond energy in  $\text{NH}_3\cdots\text{F}^-$ ,  $\text{NFH}_2\cdots\text{F}^-$  and  $\text{NF}_2\text{H}\cdots\text{F}^-$  were calculated to be  $-67.9 \text{ kJ}\cdot\text{mol}^{-1}$ ,  $-120.2 \text{ kJ}\cdot\text{mol}^{-1}$  and  $-181.2 \text{ kJ}\cdot\text{mol}^{-1}$ , respectively, and clearly show the effect of fluorination on hydrogen bond strength in amine-fluoride systems. The change in enthalpy and entropy for

the clustering of methanol to  $\text{NF}_2\text{H}\cdots\text{F}^-$  to form the fluoride bound dimer of methanol and difluoramine has been measured *via* high pressure mass spectrometry to be  $-68.3 \text{ kJ}\cdot\text{mol}^{-1}$  and  $-90.5 \text{ J}\cdot\text{K}^{-1}\cdot\text{mol}^{-1}$ . These values are in excellent agreement with the calculated analogues,  $-70.9 \text{ kJ}\cdot\text{mol}^{-1}$  and  $-88.5 \text{ J}\cdot\text{K}^{-1}\cdot\text{mol}^{-1}$ .

Finally, an examination of the thermochemical properties associated with the formation of a hydrogen bond linkage between protic solvents and deprotonated amino acids has been performed. In addition to observations of the effect of side chain substitution, a comparison between measured and calculated properties has provided insight into the thermochemical effects arising from the isomeric nature of this clustering system. A new theoretical model describing the impact of a distribution of isomers on thermochemical measurements made *via* high pressure mass spectrometry is given. When this new model was applied, and the distribution of isomers correctly accounted for, the measured values of  $\Delta H^\circ$ ,  $\Delta S^\circ$  and  $\Delta G_{298}^\circ$  consistently agreed, to a very high degree of accuracy, with those predicted by MP2(full)/6-311++G(d,p)//B3LYP/6-311++G(d,p) calculations. As well, IR spectra for the clustering of deprotonated glycine with ROH have been calculated and analyzed to demonstrate the ability of techniques such as IRMPD to identify the presence of a distribution of isomers.

## Acknowledgements

The expression “thank you” is often used in the Acknowledgement section of a thesis, but sometimes those two words are just not enough to express the gratitude felt as a result of the generosity of others. How do you thank someone who has guided and mentored you through some of the most challenging years of your life? How do you thank those people who have loved and supported you through the good and the bad? How do you thank someone who would literally drive any distance to be with you? The answer to all of these questions, as it turns out, is quite simple... start naming names and use bold and italics fonts when referring to them as much as possible!!

Firstly, I must single out my supervisor, **Terry McMahon**, to whom I will be forever indebted to on account of his never-ending generosity and faith. I have had more opportunities than any graduate student could ever hope or wish for, whether it be travel to prestigious international conferences, 50+ hour work marathons in far-off research labs, not to mention the opportunity to learn more about the insides of a mass spectrometer than any person should ever have to know! **Thank you, Terry**, for showing me what science is really about and for taking a chance on me when no funding agency would!

During these past five years of data collection I have developed a long list of names of people whose contributions have truly been indispensable. I must thank **Chad, Opal, Nathan, Melissa** and **Matt W.** for their enthusiasm and tireless efforts in helping to get “one more point” or find “one more structure”. Without your help it would have been another five years! I would also like to **thank** my incredibly talented **advisory committee** for the wisdom and guidance they have imparted to me over the years, not to mention a most humble “thank-you-in-advance” for what will hopefully be a pleasant defense. Because without your help it would have been another five years!!! I must also **thank** the always-helpful **Cathy, Janice, Lisa** and other **administrative staff**, who never hesitated to help in any way possible. Without your help it would have been impossible to finish!

There have been many people in Waterloo that have made grad school into what I’m sure will be some of the best years of my life. No lab or conference will ever be the same

without the combination of ***Travis***, ***Rick***, ***Ronghu***, ***Matt F.***, ***Chad***, ***Jon*** and ***Kris***. A special ***thanks*** must be given to ***Rick*** for being a true friend, labmate and housemate and for always helping me out whenever needed. Outside of the lab there have truly been too many great people to list all of the names, but without each of you this experience just would not have been the same. ***Andrew***, ***Kristy***, ***Mak***, ***Jay*** and ***Mike*** to name only a few, and to everyone else, I trust that you know who you are!

There are many people outside of Waterloo that deserve equally-important recognition for the help they have given me. I would like to ***thank*** my ***Mom*** and ***Dad*** for the unconditional love and support that they have shown me all of my life. From the early years, when they literally dragged me to school kicking and screaming, to the more recent years, when they were begging me to hurry up and finally graduate, they have always been there to encourage and guide me in making the right decisions. ***Thank you*** for always being there! A special “***thank you***” must be given to my sister, ***Lisa***, who has always been a role model to me and a tough act to follow! ***Thanks, Lisa***, for raising the bar! An equally important “***thank you***” must be given to ***Jason*** for keeping Lisa grounded when she launches up and over the bar and soars off into her own world! ***Thank you, thank you, thank you!*** To my grandparents who have taught me the value of hard work, and my aunts, uncles, and cousins, who have always supported, encouraged, and humored me while I enthusiastically explain what it is that I do, and perhaps most importantly, always spice things up around the holidays. ***Thank you!*** To the ***Benson***, ***Gorewich*** and ***Hamstra*** clans: ***thank you*** for always being so welcoming of me and for being so understanding of me while I ate you out of house and home! ***Thank you*** to ***David*** for your extreme generosity. Big White and all of the bike rides have definitely helped to drop the stress level over the last few years.

Finally, I must give ***thanks*** to my best friend and girlfriend, ***Jen***, who has truly made the whole experience worthwhile. She has always been there to make me laugh and smile during the best of times and the worst of times, and has been more than supportive during the writing of this thesis. To a co-operative ***Jen***: ***Thank you*** for all of the love you have given me.

**- To My Parents -**

## Table of Contents

List of Figures .....	xi
List of Tables .....	xvii
List of Abbreviations .....	xix
Chapter 1 Introduction .....	1
1.1 General Introduction.....	1
1.2 Thermochemical Properties of Systems in Equilibrium.....	4
Chapter 2 Experiment and Theory .....	9
2.1 Pulsed-Ionization High Pressure Mass Spectrometry .....	12
2.2 Quantum Chemical Calculations.....	26
2.2.1 Electronic Structure Calculations .....	26
2.2.2 Describing Anionic Systems with Hydrogen Bonding.....	39
Chapter 3 Investigations of Strong Hydrogen Bonding in $(ROH)_n \cdots FHF^-$ ( $n = 1, 2$ and $R = H, CH_3, C_2H_5$ ) Clusters <i>via</i> High Pressure Mass Spectrometry and Quantum Calculations.....	43
3.1 Introduction .....	43
3.2 Experimental Methods .....	45
3.3 Results and Discussion .....	49
3.3.1 Step-wise Solvation of $FHF^-$ by $H_2O$ .....	49

3.3.2 Step-wise Solvation of FHF <sup>-</sup> by CH <sub>3</sub> OH .....	58
3.3.3 Step-wise Solvation of FHF <sup>-</sup> by C <sub>2</sub> H <sub>5</sub> OH.....	61
3.3.4 Summary of Thermochemical and Geometric Trends.....	66
3.4 Conclusions .....	71

#### Chapter 4 Strong and Very Strong Hydrogen Bonding in Fluoro-amine –

Fluoride Systems .....	72
4.1 Introduction .....	72
4.2 Experimental .....	74
4.3 Results and Discussion .....	79
4.3.1 Thermochemical Data.....	79
4.3.2 Structural Aspects of Cluster Formation.....	89
4.4 Conclusion.....	92

#### Chapter 5 Effects of Isomerization on the Measured Thermochemical Properties

of Deprotonated Amino Acid/Protic-Solvent Clusters.....	94
5.1 Introduction .....	94
5.2 Experimental .....	97
5.3 Results and Discussion .....	104
5.3.1 Clustering of Deprotonated Glycine with ROH.....	105
5.3.2 Clustering of Deprotonated Alanine, Valine and Serine with ROH .....	121
5.3.3 Thermochemical Trends .....	129
5.3.4 Simulated IR Spectra for Deprotonated Glycine Clustered with ROH .....	140
5.4 Conclusion.....	145

Chapter 6 Summary .....	148
References .....	157
Appendices .....	158
Appendix A : Sample GAUSSIAN Input Files.....	159
Appendix B : MathCad Worksheet – Expected Observable Thermochemical Values for an Isomeric Distribution of a Cluster Ion.....	162
Appendix C : C++ Program Code – Extracting Infrared Frequencies and Intensities from a GAUSSIAN Output File .....	164
Appendix D : MathCad Worksheet – Application of Lorentzian Line-Shape Function to the Vibrational Line Spectrum of a Single or Distribution of Isomers .....	168

## List of Figures

Figure 2.1: Schematic diagram of the home-built pulsed-ionization high pressure ion source and ion acceleration and focusing optics found at the University of Waterloo .....	14
Figure 2.2: Schematic diagram of MM8-80 mass analyzer, with an 80° magnetic sector and an 8 cm radius of orbit fixed by the presence of entrance and exit slits. Magnetic field, $B$ , is oriented into the plane of the page. The resulting Lorentz force, $F$ , acts in a perpendicular fashion to both the incident trajectory of a positive ion with a speed, $v$ , and the magnetic field.....	17
Figure 2.3: Typical intensity-time profiles shown on a logarithmic intensity scale. Ions $A^-$ and $AB^-$ correspond to species involved in the equilibrium clustering reaction such that ion $A^-$ and a neutral B cluster together to form ion $AB^-$ . ....	19
Figure 2.4: Typical normalized intensity-time profiles for the clustering of $A^-$ with B to form $AB^-$ . The two profiles becoming parallel within 0.5 ms of ion formation indicates a rapid establishment of equilibrium.....	22
Figure 3.1: Typical $\log_{10}(\text{intensity})$ -time profiles for the ion clusters of $\text{FHF}^-$ with one and two water molecules. <i>Inset:</i> Normalized intensity-time profiles.....	48
Figure 3.2: van't Hoff plots for the sequential clustering of one and two water, methanol and ethanol molecules to $\text{FHF}^-$ .....	50

Figure 3.3: Structures and geometric properties of $\text{FHF}^- \cdots (\text{H}_2\text{O})_n$ clusters, $n = 1$ and 2.....	53
Figure 3.4: Structures and geometric properties of $\text{FHF}^- \cdots (\text{CH}_3\text{OH})_n$ clusters, $n = 1$ and 2.....	60
Figure 3.5: Structures and geometric properties of $\text{FHF}^- \cdots (\text{C}_2\text{H}_5\text{OH})_n$ clusters, $n = 1$ and 2.....	63
Figure 3.6: Measured and calculated ergonicity of stepwise formation reactions for $(\text{ROH})_n \cdots \text{FHF}^-$ as a function of the gas phase acidity of ROH ( $n = 1$ and 2; R = H, CH <sub>3</sub> , C <sub>2</sub> H <sub>5</sub> ). Gas-phase acidities for H <sub>2</sub> O, CH <sub>3</sub> OH and C <sub>2</sub> H <sub>5</sub> OH were obtained from ref <sup>82</sup> , ref <sup>57</sup> and ref <sup>57</sup> , respectively.....	67
Figure 3.7: Calculated F-F bond distances in $(\text{ROH})_n \cdots \text{FHF}^-$ clusters ( $n = 1$ and 2; R = H, CH <sub>3</sub> , C <sub>2</sub> H <sub>5</sub> ) plotted against the gas phase acidity of ROH. Note, only F-F distances for the most ergonomically favorable species are plotted. Gas-phase acidities for H <sub>2</sub> O, CH <sub>3</sub> OH and C <sub>2</sub> H <sub>5</sub> OH were obtained from ref <sup>82</sup> , ref <sup>57</sup> and ref <sup>57</sup> , respectively.....	69
Figure 3.8: Calculated F-O bond distances in $(\text{ROH})_n \cdots \text{FHF}^-$ clusters ( $n = 1$ and 2; R = H, CH <sub>3</sub> , C <sub>2</sub> H <sub>5</sub> ) plotted against the gas phase acidity of ROH. Note, only F-O distances for the most ergonomically favorable species are plotted. In the case of the doubly solvated clusters, the C <sub>2</sub> symmetry of these clusters reduces the discussion of two separate OHF hydrogen bonds to that of one identical pair ( <i>via</i> an 180° rotation) of OHF bonds. Gas-phase acidities for H <sub>2</sub> O, CH <sub>3</sub> OH and C <sub>2</sub> H <sub>5</sub> OH were obtained from ref <sup>82</sup> , ref <sup>57</sup> and ref <sup>57</sup> , respectively.....	70

Figure 4.1: Structure of NF <sub>2</sub> H as determined from microwave spectroscopy by Lide. <sup>87</sup>	73
Figure 4.2: Time-intensity profiles for NF <sub>2</sub> H···F <sup>-</sup> and NF <sub>2</sub> H···F <sup>-</sup> ···CH <sub>3</sub> OH at 117 °C and P <sub>CH<sub>3</sub>OH</sub> = 7.45 millitorr. Each profile is the result of the summation of ion intensity after 7000 electron gun pulses.	77
Figure 4.3: Normalized time-intensity profiles for NF <sub>2</sub> H···F <sup>-</sup> and NF <sub>2</sub> H···F <sup>-</sup> ···CH <sub>3</sub> OH. Equilibrium is established 0.5 ms after ionization and lasts until 3 ms after ionization. The apparent divergence observed after 4 ms is an artifact of low signal intensity and is not an indication that the system is not at equilibrium.	78
Figure 4.4: van't Hoff plot collected over a 92 degree temperature range from 55 °C to 147 °C for clustering of NF <sub>2</sub> H···F <sup>-</sup> with CH <sub>3</sub> OH. Error bars on each data point indicate standard deviation of 6-10 repetitive measurements of K <sub>eq</sub> at each temperature.	80
Figure 4.5: Optimized geometries obtained from B3LYP/6-311++G(d,p) calculations: (I) NF <sub>2</sub> H (II) NF <sub>2</sub> H···F <sup>-</sup> (III) CH <sub>3</sub> OH (IV) CH <sub>3</sub> OH···F <sup>-</sup> (V) Fluoride bound dimer of CH <sub>3</sub> OH and NF <sub>2</sub> H. All distances are in Å and bond angles are in degrees.	81
Figure 4.6: Calculated reaction profile for the formation of CH <sub>3</sub> OH···F <sup>-</sup> ···NF <sub>2</sub> H clusters using B3LYP/6-311++G(d,p). Two pathways, each consisting of two steps, are shown.	83
Figure 4.7: Optimized geometries obtained from B3LYP/6-311++G(d,p) calculations: (I) NH <sub>3</sub> ···F <sup>-</sup> (II) NFH <sub>2</sub> ···F <sup>-</sup> (III) NF <sub>2</sub> H···F <sup>-</sup> .	84

Figure 4.8: Plot of fluoride binding enthalpy ( $\Delta H_{FBE}$ ) versus enthalpy of deprotonation ( $\Delta H_{acid}$ ) demonstrates the effect of fluorine substitution on hydrogen bond strength in the $NF_nH_{3-n}\cdots F^-$ system. Electronic energies//optimized geometries obtained from MP2(full)/6-311++G(d,p) // B3LYP/6-311++G(d,p) calculations. ....	87
Figure 5.1: Typical $\log_{10}(\text{Intensity})$ – Time profiles for the clustering of deprotonated glycine with an ROH solvent. Inset: normalized Intensity-Time profiles.....	100
Figure 5.2: van't Hoff Plots for the clustering of $NH_2CH_2COO^-$ with $H_2O$ , $CH_3OH$ and $C_2H_5OH$ .....	106
Figure 5.3: van't Hoff Plots for the clustering of $NH_2CH(CH_3)COO^-$ with $H_2O$ , $CH_3OH$ and $C_2H_5OH$ .....	107
Figure 5.4: van't Hoff Plots for the clustering of $NH_2CH(CH(CH_3)_2)COO^-$ with $H_2O$ , $CH_3OH$ and $C_2H_5OH$ . ....	108
Figure 5.5: van't Hoff Plots for the clustering o f $NH_2CH(CH_2OH)COO^-$ with $H_2O$ , $CH_3OH$ and $C_2H_5OH$ .....	109
Figure 5.6: Lowest energy structures obtained using MP2(full)/6-311++G(d,p) // B3LYP/6-311++G(d,p), for the attachment of ROH to the carboxylate or amine moiety of $NH_2CH_2COO^-$ . Distances are in units of angstroms. ....	111
Figure 5.7: Isomeric forms obtained using MP2(full)/6-311++G(d,p) // B3LYP/6-311++G(d,p), for the attachment of ROH to the carboxylate moiety of $NH_2CH_2COO^-$ . Distances are in units of angstroms.....	114

Figure 5.8: Potential energy profiles for the A) rotational transformation from 4IV to 4III and B) translational transformation from 3I to both 4I and 4II, at 298K. All optimized structures and transition states were calculated *via* MP2(full)/6-311++G(d,p) // B3LYP/6-311++G(d,p). ..... 116

Figure 5.9: Relative isomer distribution for A) water, B) methanol and C) ethanol clustered to deprotonated glycine at the maximum and minimum experimental temperatures. The isomer number refers to an isomers rank from lowest  $\Delta G_{298,calc}^\circ$ , (1), to highest within each clustering system..... 118

Figure 5.10: Lowest energy structures obtained using MP2(full)/6-311++G(d,p) // B3LYP/6-311++G(d,p), for the attachment of ROH to the carboxylate or amine moiety of  $\text{NH}_2\text{CH}(\text{CH}_3)\text{COO}^-$ . Distances are in units of angstroms. .... 122

Figure 5.11: Lowest energy structures obtained using MP2(full)/6-311++G(d,p) // B3LYP/6-311++G(d,p), for the attachment of ROH to the carboxylate or amine moiety of  $\text{NH}_2\text{CH}(\text{CH}(\text{CH}_3)_2)\text{COO}^-$ . Distances are in units of angstroms. .... 123

Figure 5.12: Lowest energy structures obtained using MP2(full)/6-311++G(d,p) // B3LYP/6-311++G(d,p), for the attachment of ROH to the carboxylate or amine moiety of  $\text{NH}_2\text{CH}(\text{CH}_2\text{OH})\text{COO}^-$ . Distances are in units of angstroms. .... 124

Figure 5.13: Negative free energy change (298 K) as a function of the gas-phase acidity of solvent molecule, for the formation of clusters of deprotonated glycine with ROH. .... 130

Figure 5.14: Negative free energy change (298 K) as a function of the gas-phase acidity of solvent molecule, for the formation of clusters of deprotonated alanine with ROH .....	131
Figure 5.15: Negative free energy change (298 K) as a function of the gas-phase acidity of solvent molecule, for the formation of clusters of deprotonated valine with ROH .....	132
Figure 5.16: Negative free energy change (298 K) as a function of the gas-phase acidity of solvent molecule, for the formation of clusters of deprotonated serine with ROH .....	133
Figure 5.17: Lowest energy structures obtained using MP2(full)/6-311++G(d,p) // B3LYP/6-311++G(d,p), for the attachment of ROH to $\text{CH}_3\text{COO}^-$ . Distances are in units of angstroms. ....	135
Figure 5.18: Negative ergonicity associated with the formation of $\text{ROH}\cdots[\text{M}-\text{H}]^-$ clusters at 298 K plotted as a function of the enthalpy of deprotonation ( $\text{M} = \text{Gly, Ala, Val, Ser}$ ). ....	139
Figure 5.19: Simulated spectrum for a distribution of isomers at 298 K. Deprotonated glycine clustered with water.....	141
Figure 5.20: Simulated spectrum for a distribution of isomers at 298 K. Deprotonated glycine clustered with methanol.....	142
Figure 5.21: Simulated spectrum for a distribution of isomers at 298 K. Deprotonated glycine clustered with ethanol.....	143

## List of Tables

Table 2-1: Validating the Choice of Method and Basis Set From a Comparison to Literature for Select Anionic Hydrogen Bonding Systems .....	42
Table 3-1: Measured and Calculated Thermochemical Properties for Examined Clustering Processes. ....	51
Table 3-2: Summary of Important Geometric Properties of FHF <sup>-</sup> and Several Solvated FHF <sup>-</sup> Clusters. ....	54
Table 3-3: Calculated and Measured Thermochemical Properties of Various Isomers of (ROH) <sub>n</sub> ⋯FHF <sup>-</sup> .....	57
Table 4-1: Summary of thermodynamic data pertaining to equilibrium reactions studied .....	86
Table 4-2: Calculated and literature values of $\Delta H_{rxn}^\circ$ (kJ·mol <sup>-1</sup> ) for $\text{NF}_n\text{H}_{3-n} \rightleftharpoons \text{NF}_n\text{H}_{2-n}^- + \text{H}^+$ using B3LYP/6-311++G(d,p) geometry optimizations and MP2(full)/6-311++G(d,p) electronic energy.....	88
Table 5-1: Thermochemical Properties for the Formation of ROH ⋯ [M – H] <sup>-</sup> (M = Gly, Ala, Val, Ser; R = H, CH <sub>3</sub> , C <sub>2</sub> H <sub>5</sub> ) determined via High Pressure Mass Spectrometry.....	110
Table 5-2: Measured and Calculated Thermochemical Properties for the Formation of ROH ⋯ [Gly – H] <sup>-</sup> , R = H, CH <sub>3</sub> , C <sub>2</sub> H <sub>5</sub> .....	112

Table 5-3: Calculated Thermochemical Properties for Higher Energy Isomers of ROH ... [Gly - H] <sup>-</sup> , R = H, CH <sub>3</sub> , C <sub>2</sub> H <sub>5</sub> obtained using MP2(full)/6- 311++G(d,p)//B3LYP/6-311++G(d,p) .....	115
Table 5-4: Estimate of the number of isomers of the cluster ion, N, compared to the number found to be feasible from electronic structure calculations, N <sub>observed</sub> . ΔS° values are reported in J·K <sup>-1</sup> ·mol <sup>-1</sup> .....	120
Table 5-5: Measured and Calculated Thermochemical Properties for the Formation of ROH ... [Ala - H] <sup>-</sup> , R = H, CH <sub>3</sub> , C <sub>2</sub> H <sub>5</sub> .....	125
Table 5-6: Measured and Calculated Thermochemical Properties for the Formation of ROH ... [Val - H] <sup>-</sup> , R = H, CH <sub>3</sub> , C <sub>2</sub> H <sub>5</sub> .....	126
Table 5-7: Measured and Calculated Thermochemical Properties for the Formation of ROH ... [Ser - H] <sup>-</sup> , R = H, CH <sub>3</sub> , C <sub>2</sub> H <sub>5</sub> .....	127
Table 5-8: Thermochemical Properties for the Clustering of Acetate with ROH, R = H, CH <sub>3</sub> , C <sub>2</sub> H <sub>5</sub> .....	136

## List of Abbreviations

$\Delta$	change in
$\Delta_{acid} G^\circ$	gas phase acidity, standard Gibbs free energy of deprotonation
$\Delta G_{calc,T}^\circ$	calculated standard Gibbs free energy change of a reaction
$\Delta G_{exp,T}^\circ$	measured standard Gibbs free energy change of a reaction
$\Delta G_{rxn,T}^\circ$	standard Gibbs free energy change of a reaction
$\Delta H_{acid}^\circ$	enthalpy change for loss of a proton
$\Delta H_{FBE}^\circ$	enthalpy change for loss of fluoride
$\Delta H_{calc}^\circ$	calculated standard enthalpy change of a reaction
$\Delta H_{exp}^\circ$	measured standard enthalpy change of a reaction
$\Delta H_{rxn}^\circ$	standard enthalpy change of a reaction
$\Delta S_{mix}^\circ$	entropy of mixing
$\Delta S_{calc}^\circ$	calculated standard entropy change of a reaction
$\Delta S_{exp}^\circ$	measured standard entropy change of a reaction
$\Delta S_{rxn}^\circ$	standard entropy change of a reaction
B3LYP	Becke-style three parameter density functional theory utilizing the electron correlation functional of Lee, Yang and Parr
CEM	channeltron electron multiplier
CID	collision induced dissociation
DFT	density functional theory
DNA	deoxyribonucleic acid
FT-ICR	Fourier transform ion cyclotron resonance

HF	Hartree-Fock
HPMS	high pressure mass spectrometry
ICR	ion cyclotron resonance
IR	infrared
IRMPD	infrared multi-photon dissociation
MCS	multi-channel scalar
MP2	second order Møller-Plesset perturbation theory
msi	most stable isomer
NMR	nuclear magnetic resonance
PC	personal computer
PHPMS	pulsed-ionization high pressure mass spectrometry
SSHB	short strong hydrogen bond
UV	ultraviolet
ZPE	zero point energy

# **Chapter 1**

## **Introduction**

### **1.1 General Introduction**

There is no denying the absolute importance of hydrogen bonding in the description of a large number of chemical and biological systems, and as such, several reports and reviews of the fundamental nature of this important bonding mechanism have been performed.<sup>1-19</sup>

These intermolecular interactions govern many important processes, such as the base pairing of DNA and secondary structure of proteins, and have great influence over the bulk properties of many substances, such as the high boiling point of water. Since many of these processes (or properties) may occur in (or can be attributed to) the condensed phases, it can often be difficult to distinguish those effects resulting from the formation of hydrogen bonds and those arising from solvent (or matrix) effects. As a complement to the large body of condensed phase data, investigations of hydrogen bonding are quite often performed in the gas phase since unique insight into the true nature of ion/molecule hydrogen bonding can be obtained in an unperturbed manner, without the complicating effects of solvents. Moreover, the unique instrumentation available to the gas-phase chemist allows for the “growing” of hydrogen-bonded clusters in a stepwise fashion, such that the effects arising from the sequential addition of solvent molecules to a cluster can be investigated.

The history of the study of hydrogen bonding dates back to the beginning of the twentieth century, when in 1902 Werner first revealed the structure of “ammoniumhydroxyde” to be the hydrogen bonded complex of ammonia and water.<sup>6</sup> Over the subsequent two decades more and more instances of the unique hydrogen bridge began to

surface, until in 1920 Latimer and Rodebush formulated the first definition of a hydrogen bond as being the condition that arises when a hydrogen nucleus is held between 2 octets.<sup>6</sup> Upon the introduction of quantum mechanics to the study of intermolecular interactions, further insight into the true nature of hydrogen bonding was obtained. During the infancy of its quantum mechanical description, hydrogen bonding was viewed as a process governed by the electrostatic interaction between a proton-donating polar bond, X-H, and an electronegative species Y. In an attempt to be rigorous, Pauling described an X-H...Y interaction as consisting of no more than one covalent bond, and that the force of attraction between X and Y is largely ionic.<sup>2</sup> While this model provided a reasonable description of hydrogen bonding between sufficiently electronegative species, such as in the classic case of water, a slightly broader description of the hydrogen bond is now widely accepted. In general, when a covalently-bound hydrogen forms a second interaction to an electron donating species, a hydrogen bond is considered to have been formed.<sup>13</sup>

Under the umbrella of this much broader definition, interactions ranging in magnitude from the van der Waals regime ( $10^{-1}$ - $10^0$  kJ·mol<sup>-1</sup>) up to the covalent regime ( $>10^2$  kJ·mol<sup>-1</sup>) can be labeled to be of the hydrogen bond variety. For example, interactions in which a CH moiety acts as the proton donating XH group typically fall into the category of weak hydrogen bonds. Those hydrogen bonds formed between neutral molecules, or when  $\pi$  or  $\sigma$  electrons act as the proton-accepting Y site, can be described as being in the normal hydrogen bond strength regime. Charge assisted hydrogen bonds, such as those found to involve ions, almost always fall into the category of strong hydrogen bonds. In fact, the strong hydrogen bonds can even be stronger than a covalently bound counterpart. For

instance, the strongest experimentally determined hydrogen bond strength is that of the prototypical  $\text{FHF}^-$ , for which Wentholt and Squires determined a value of  $192 \text{ kJ}\cdot\text{mol}^{-1}$  for the dissociation into  $\text{F}^-$  and  $\text{HF}$ .<sup>20</sup> In contrast, the dissociation energy associated with the covalent bond found in  $\text{F}_2$  has been determined to be  $157 \text{ kJ}\cdot\text{mol}^{-1}$ .<sup>21</sup> It is the objective of this thesis to investigate the various thermochemical and structural properties associated with the clustering of anions with protic solvents, and thus, the formation of strong hydrogen bonds.

Several relationships between the strength of a hydrogen bond and the physical properties of the involved species have been noted. Knowledge of the dipole moment strength of  $\text{XH}$ , polarizability of  $\text{Y}$ , electronegativity of  $\text{X}$  and  $\text{Y}$  to name only a few, can help one achieve an *a priori* estimate of the relative strength of a bond. Perhaps the best indicators of this type are the gas-phase acidity and basicity of  $\text{XH}$  and  $\text{Y}$ . These relationships were first reported by Yamdagni and Kebarle, as observed in their high pressure mass spectrometry study of hydrogen bond strengths to anionic species.<sup>22</sup> To understand these relationships, an  $\text{X}-\text{H}\cdots\text{Y}$  hydrogen bonded complex can be considered to be bridged *via* the proton-donating  $\text{X}-\text{H}$  moiety and a proton-accepting  $\text{Y}$  moiety. It was observed that if the acid strength\* of the solvent,  $\text{X}-\text{H}$ , increases while the basicity of  $\text{Y}$  remains constant, the measured bond strength for the resulting hydrogen bond will increase. Likewise, if the acid strength of  $\text{X}-\text{H}$  remains constant while the basicity of  $\text{Y}$  increases, the hydrogen bond is once again observed to strengthen. On the other hand, an *a posteriori* estimate of hydrogen-bond strength can be made from an inspection of changes in the physical properties of the

---

\* Note that in this thesis the term acid strength denotes proton donating ability. This is to be differentiated from the thermochemical definition of acidity, which is the free energy associated with deprotonation of an acid,  $\text{AH}$ , such that a higher value of acidity denotes a lower acid strength.

newly formed cluster. Most notably, a shortening of the X-Y distance, a lengthening of the X-H distance, an approach of the ratio of XH distance to the HY distance to unity, an approach of the XHY bond angle towards linearity, a red shift in the frequency of the observed proton vibration, and a shift in the proton nuclear magnetic resonance (NMR) signals to lower magnetic field all indicate an increase in the strength of a hydrogen bond.<sup>13</sup>

In this thesis an examination of many of the above relations are performed. More specifically, prototypical, biologically important, or essentially novel hydrogen-bonded systems formed through equilibrium clustering reactions are examined, both experimentally and computationally. In the first system examined, the prototypical strong-hydrogen-bonded species FHF<sup>-</sup> is clustered through hydrogen bonds with a series of protic solvents. In the second system presented, the effects of fluorine substitution and competitive clustering on charge assisted NH...F bonds are examined. Finally, the biologically-important deprotonated amino acids are clustered to a series of protic solvents, providing a wealth of detail on the nature of these interactions, as well as the effects of a distribution of isomeric clusters on measured thermochemical values. However, before a discussion of these systems can be presented, rigor demands that an overview of equilibrium clustering reactions and their associated thermochemical properties, as well as the various approaches to their study, be given.

## **1.2 Thermochemical Properties of Systems in Equilibrium**

One method of studying the thermochemical properties of a hydrogen bond is through the examination of an association reaction in the gas phase, such as the one depicted in Eq.

1.1. In this general reaction A<sup>-</sup> and B can interact through any intermolecular force, including the hydrogen bond, and can be thought of as being in equilibrium when the forward rate of reaction is equal to the backward rate of reaction. In perhaps a more rigorous definition, a state of equilibrium is said to have been reached when the sum of the stoichiometrically-weighted chemical potentials of the products is equal to the sum of the stoichiometrically-weighted chemical potentials of the reactants, as in Eq. 1.2. Here  $v_x$  and  $\mu_x$  are the stoichiometric co-efficient and chemical potential of component  $x$ . The chemical potential, Eq. 1.3, is equal to the chemical potential of a substance in its standard state,  $\mu_i^\circ$ , plus a factor of  $RT\ln(a_j)$ , where  $R$  is the ideal gas constant,  $T$  is the temperature of the system and  $a_x$  is the activity of component  $x$ . Upon substitution of Eq. 1.3 into Eq. 1.2, followed by rearrangement, Eq. 1.4 is obtained, which, as soon to be shown, is a very useful expression.



$$\sum_{products} v_j \mu_j - \sum_{reactants} v_i \mu_i = 0 \quad 1.2$$

$$\mu_i = \mu_i^\circ + RT\ln(a_j) \quad 1.3$$

$$\sum_{products} v_j \mu_j^\circ - \sum_{reactants} v_i \mu_i^\circ = -RT \left[ \ln \left( \frac{\prod_{products} (a_j^{v_j})}{\prod_{reactants} (a_i^{v_i})} \right) \right] \quad 1.4$$

At equilibrium, the ratio of products ( $\Pi$ ) within the logarithm in Eq. 1.4 is a constant and is thus named the equilibrium constant, Eq. 1.5. For the ideal gas-phase equilibrium association reaction of Eq. 1.1  $a_j = P_j/P_o$ , where  $P_j$  is the partial pressure of component  $j$  and  $P_o$  is the standard reference pressure of gases ( $P_o = 1$  bar), the equilibrium constant can be expressed as Eq. 1.6.

$$K_{eq} = \frac{\prod_{products}(a_j^{v_j})}{\prod_{reactants}(a_i^{v_i})} \quad 1.5$$

$$K_{eq} = \frac{P_{AB^-}}{P_{A^-} \cdot P_B} \cdot P_o \quad 1.6$$

In addition, in Eq. 1.2, it should also be pointed out that the product of  $v_i$  and  $\mu_i$  is equal to the Gibbs free energy,  $G_i$  for component  $i$ . To elaborate, the Gibbs free energy is also related to the enthalpy,  $H_i$ , and entropy,  $S_i$ , of component  $i$ , Eq. 1.7. By taking the difference in Gibbs free energy between products and reactants for a reaction of interest, a measure of the total amount of useful work<sup>†</sup> that is possible is obtained, Eq. 1.8. The enthalpy of a component has a similar interpretation, but does not include the effects of entropy. More explicitly, enthalpy is defined as the total internal energy of component  $i$ ,  $U_i$ , plus the product of pressure and volume. A change in the enthalpy of a reaction can be interpreted as a measure of the energy absorbed or released, after only the effects of pressure-

---

<sup>†</sup> The term “useful work” denotes the total amount of energy that is absorbed or released from a reaction, after changes in internal energy, entropy and PV-work have been accounted for.

volume work have been accounted for. The entropy term is a bit harder to define, but one interpretation of its meaning is that it represents the number of different ways of distributing a system into equal representations of a given state, per unit of temperature. A change in entropy for a reaction can thus be interpreted as the energy required per unit of temperature to redistribute all equivalent representations of all of the reactants into all equivalent representations of the products.

$$G_i(T) = H_i - TS_i \quad 1.7$$

$$\Delta G_{rxn}(T) = \Delta H_{rxn} - T\Delta S_{rxn} \quad 1.8$$

Eq. 1.7 and Eq. 1.8 still hold when the components of a reaction are in their standard states, but a distinction is made through the use of the superscript “naught”, as in Eq. 1.7. This distinction is subtle yet important, since at equilibrium, as seen in Eq. 1.2, the change in Gibbs free energy,  $\Delta G_{rxn}(T)$ , is equal to zero, while  $\Delta G_{rxn}^\circ(T)$  is equal to  $-RT\ln(K_{eq}(T))$ , as seen in Eq. 1.4 and Eq. 1.10.

$$\Delta G_{rxn}^\circ(T) = \Delta H_{rxn}^\circ - T\Delta S_{rxn}^\circ \quad 1.9$$

$$\Delta G_{rxn}^\circ(T) = -RT\ln(K_{eq}(T)) \quad 1.10$$

By combining Eq. 1.9 and Eq.1.10 the van't Hoff isotherm, which describes the behavior of the equilibrium constant as a function of temperature, can be obtained, Eq. 1.11. It should be pointed out that both the change in enthalpy and entropy do exhibit an inherent dependence on temperature. However, if the change in heat capacity between the products and reactants remains constant over the temperature range of interest, then the standard change in enthalpy and entropy can be considered to be constant. If measurements of  $K_{eq}$  are made as a function of temperature, then the value of  $\Delta H_{rxn}^\circ$  and  $\Delta S_{rxn}^\circ$  associated with an equilibrium process can be obtained from a plot of  $\ln(K_{eq}(T))$  versus  $1/T$ .

$$\ln(K_{eq}(T)) = -\frac{\Delta G_{rxn}^\circ(T)}{RT} = -\frac{\Delta H_{rxn}^\circ}{RT} + \frac{\Delta S_{rxn}^\circ}{R} \quad 1.11$$

## **Chapter 2**

### **Experiment and Theory**

A wide variety of tools are available to the gas phase chemist investigating ion/molecule interactions. For the most part, it is possible to make experimental measurements of thermochemical or kinetic variables, such as equilibrium constants, rate constants, standard enthalpy, entropy or Gibbs free energies of a reaction, and then accurately model and predict those same properties using a combination of quantum mechanics, molecular dynamics and statistical mechanics. The degree of accuracy of both experimentally and computationally determined values will undeniably depend on the techniques and methods used, and caution must be employed while interpreting results. It can, however, be said that when rigorous attention to detail is combined with sound chemical intuition, confident conclusions can be drawn, so long as one stays within the inherent error limits of the method.

Many experimental approaches for the measurement of thermochemical properties of ionic clusters have been developed, each with varying degrees of accuracy. To name only a few, pulsed-ionization high pressure mass spectrometry (PHPMS), the kinetic method of Cooks and the “third law” method as has been implemented in ICR and FTICR experiments enable the measurement of thermochemical values with varying success. The third law method, for example, has been praised in its ability to measure thermochemical properties with very low uncertainties, but can often be in error when intramolecular hydrogen bonding takes place or internal rotations are released or hindered.<sup>23</sup> At a small cost to accuracy, the kinetic method is considered to be highly successful because of its simplicity and convenience of use. For that very same reason, however, the kinetic method has often been

criticized, since the approximations and simplifications made impose restrictions on its applicability to certain chemical systems. In contrast, PHPMS is unique in its ability to directly measure the thermochemical properties of cluster ions without the need of a reference compound, and constitutes the most rigorous method of determining these values.<sup>23</sup> This fact, combined with the ability of this technique to produce thermochemical data with a reliably high degree of accuracy and reproducibility, has established PHPMS as one of the most successful methods of studying ion-molecule equilibria.<sup>24</sup>

Over the last 50 years, through the advent and advancement of computational and numerical methods, a revolution in physical chemistry has occurred. By combining modern electronic structure calculations and statistical thermodynamics, the thermochemical properties of an experimentally explored system can be reproduced with moderate to high degrees of accuracy.<sup>25</sup> In fact, this is now common practice for small to medium sized systems (up to 1000 atoms, in some cases)<sup>25</sup>. Much of the theoretical framework necessary to perform such a task, i.e. classical mechanics, statistical thermodynamics and quantum theory, was laid out before the middle of the twentieth century, but exact solutions to these problems were often unavailable. Since many of the equations involved possess no analytic solution, especially in the case of the quantum mechanical description of matter, only the simplest and most idealized of cases were soluble. The famous quote by Paul Dirac in 1929<sup>25</sup> is a testament to the disparity of the situation that existed at that time, and perhaps a significant source of motivation for a great number of theoreticians since then:

“The fundamental laws necessary for the mathematical treatment of a large part of physics and the whole of chemistry are thus completely known, and the difficulty lies only in the fact that application of these laws leads to equations that are too complex to be solved”

Until the advent of computers, theoreticians lacked a practical way to address this issue. While the literal meaning of Dirac’s statement is essentially true, that most quantum mechanical equations describing multi-electron molecules are unsolvable, many numerical methods have since been developed which can provide near exact solutions to these problems. These advancements give the modern chemist the ability to quantitatively confirm experimental observations, as well as make predictions on previously uninvestigated systems.<sup>25</sup> Of the myriad of techniques available, electronic structure methods such as *ab initio* calculations and density functional theory are amongst the most commonly used by experimental physical chemists. A description of both of these, as well as the statistical thermodynamic equations necessary for the determination of thermochemical variables is given below.

The general approach taken in the investigation of the various equilibrium systems reported in this thesis was to measure the associated thermochemical variables *via* PHPMS and then compare those values to the calculated analogues. Once the thermochemical “fingerprint” measured *via* PHPMS is matched to one calculated for a specific set of isomers, a comprehensive, and quite literal, picture of the physical phenomena under investigation is obtained.

## **2.1 Pulsed-Ionization High Pressure Mass Spectrometry**

The use of PHPMS dates back to the 1960's when Kebarle and co-workers pioneered the technique for study of the radiolysis of gases at near atmospheric pressures.<sup>26</sup> Since then, PHPMS has been an invaluable tool in the investigation of many aspects of gas-phase ion chemistry. It has been employed in the study of ion-solvent and ion-ligand equilibria, proton transfer reactions, gas-phase acidities and basicities of a wide variety of compounds, electron transfer processes, electron affinity and ionization energies, as well as hydride and halide transfer reactions, to name only a few.<sup>24</sup> Many review articles have been written on PHPMS and its applications over the years, in which detailed descriptions of all of the above processes have been given.<sup>24,27-31</sup> A more focused discussion of PHPMS as it applies to the study of the thermochemical properties related to ion-solvent equilibria will be given here, along with a description of the apparatus used to carry out the experiments reported in this thesis.

As described in Section 1.2, a gas-phase association process, such as Eq. 1.1, under conditions of thermal and chemical equilibrium will possess a thermodynamic equilibrium constant, Eq. 1.6. The temperature dependence of this equilibrium constant can be measured *via* PHPMS and, as predicted from the van't Hoff isotherm, Eq. 1.11, a measure of the standard change in enthalpy,  $\Delta H_{exp}^\circ$ , and entropy,  $\Delta S_{exp}^\circ$ , for the equilibrium reaction can be obtained from a plot of the natural logarithm of the equilibrium constant as a function of inverse temperature. Before measurements of the equilibrium constant can be made, an ion population in thermal and chemical equilibrium must first be created. At the University of Waterloo, a homebuilt pulsed-ionization high pressure ion source has been mated to a

commercially available VG 8-80 magnetic sector mass spectrometer. This unique coupling not only allows for the creation of a thermalized chemical system at various temperatures, but also allows for the measurement of ion concentrations within the ion source as a function of time after their creation. Details of its operation are given below.

A schematic diagram of the pulsed-ionization high pressure ion source, as well as ion accelerating and focusing optics is shown in Figure 2.1. Inside of the stainless steel ion source a gaseous mixture of analyte, chemical ionization agents, as well as a relatively inert third body collisional stabilization agent, also called the “bath” gas, is introduced at relatively high pressures (typically between 4 and 10 torr). The bath gas typically constitutes > 99% of this gaseous mixture, and may also act as the chemical ionization agent. Only a small amount of the gaseous mixture is allowed to leak out of the ion source through two 200  $\mu$ m apertures. One of these apertures allows for a pulsed beam of high energy electrons to enter the ion source, while the other allows for the sampling and analysis of the mixture. A large pressure differential (10 torr vs.  $10^{-7}$  torr) is maintained between the inside of the ion source and the surrounding vacuum chamber by use of high speed diffusion pumps, collectively capable of evacuating 1100 L of gas per minute. The temperature of the ion source can be varied *via* cartridge heaters which are placed within a stainless steel heating jacket. This heating jacket surrounds the ion source, allowing for experimental temperatures ranging from room temperature up to approximately 400 °C. Temperature measurements are made by a J-type iron-constantin thermocouple, which is placed within a blind hole drilled into, but not through, the side of the ion source. This arrangement allows for the temperature of the gaseous mixture to be measured with an accuracy of  $\pm 1^\circ\text{C}$ .

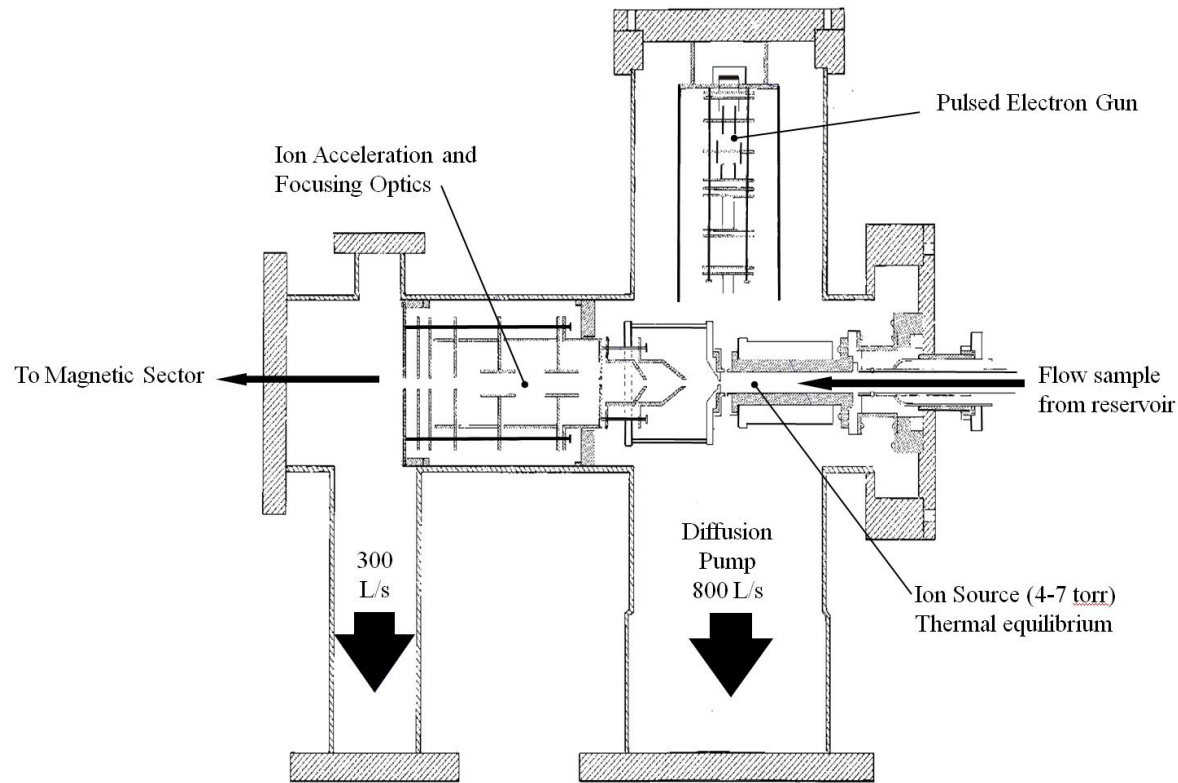


**Figure 2.1:** Schematic diagram of the home-built pulsed-ionization high pressure ion source and ion acceleration and focusing optics found at the University of Waterloo.

In order to initiate ionization, the reactant gas mixture is irradiated by a pulsed beam of electrons as it flows into the ion source. The pulsed beam of electrons can initiate several different ionization mechanisms, depending on the bath gas and chemical ionization agents present, ultimately leading to the creation of the desired ions or ion-molecule clusters. In all cases of ionization the newly formed ionic species are left with an excess internal energy. These “hot” species quickly become cooled to the temperature of the ion source, since at the experimental pressure and temperatures a collision rate of approximately  $10^8$  collisions per second exists.<sup>‡</sup> Through a diffusion controlled process, the ions disperse throughout the ion source, some of which approach the ion exit aperture. All positive or negative ions (depending on the mode of operation) exiting through this aperture become focused and accelerated toward the magnetic sector mass analyzer by a series of ion optics. Upon mass selection, the ions of interest are counted *via* a channeltron electron multiplier. Since no electric field gradient exists within the ion source, the effusing ion/molecule mixture leaving the ion source is considered to be a representative thermal equilibrium sample of the total mixture within.

The mass analyzer employed in the PHPMS at the University of Waterloo consists of an  $80^\circ$  section of a circular electromagnet, 8 cm in radius. If it is assumed that all ions exiting the ion source are accelerated through a constant electrical potential,  $V$ , then the kinetic energy, KE, of each ion is given by Eq. 2, where  $z$  is the charge number,  $e$  is the elementary charge,  $m$  is the mass of the ion and  $v$  is its speed. Even though the ions exiting the ion source will possess a Boltzmann distribution of speeds, the large electrical potential

---

<sup>‡</sup> Estimated using the Langevin Equation for collisional rate constants.

typically used to accelerate the ions ensures that the contribution of the initial non-homogeneous speed of the ions is small in comparison to the speed acquired through acceleration.<sup>32</sup> Thus, the speed of all ions entering the magnetic field can be expressed as Eq. 2.2.

$$KE = zeV = \frac{mv^2}{2} \quad 2.1$$

$$v = \sqrt{\frac{2zeV}{m}} \quad 2.2$$

For a charged particle traveling through a constant magnetic field,  $\vec{B}$ , the force,  $\vec{F}$ , experienced is determined by the Lorentz force equation, Eq. 2.3. Since there is no electric field present within the region in which the ions interact with the magnetic field, the force experienced by the ion is perpendicular to the direction of both the velocity and magnetic field, and thus the ion will exhibit circular motion, Figure 2.2. By equating the Lorentz force to the classical centrifugal force, Eq. 2.4a, and substituting in the expression for the speed of the ion, Eq. 2.2, an expression for  $m/z$  for a particular ion traveling a trajectory of fixed radius,  $r$ , is obtained, Eq. 2.4b. Since the radius of orbit is fixed by entrance and exit slits, a mass spectrum can be achieved by scanning either the magnetic field or the accelerating voltage over the desired mass range. As the magnetic field or accelerating voltage is changed, only those ions with the appropriate mass to charge ratio to achieve a radius of orbit equal to 8 cm (radius of orbit fixed by the presence of two .025 cm slits) will successfully pass through the magnetic sector. Upon impact with a channeltron electron multiplier (CEM)

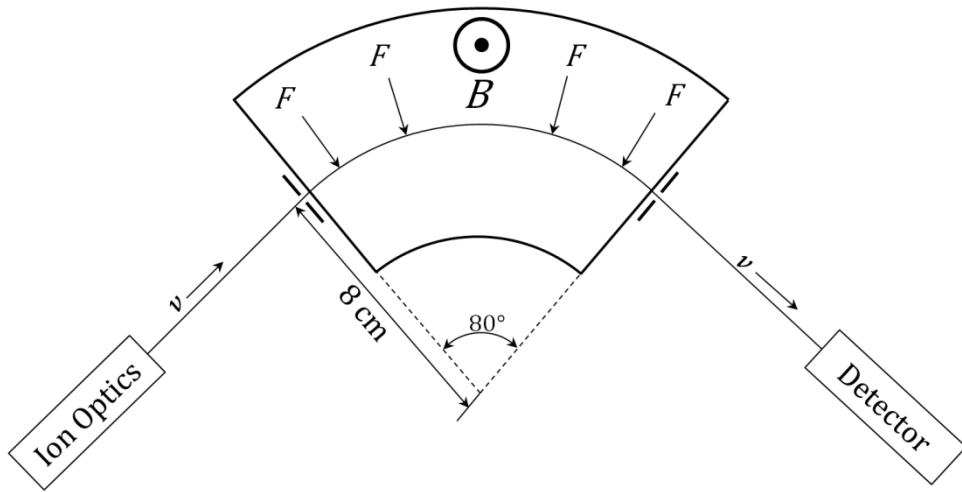


**Figure 2.2:** Schematic diagram of MM8-80 mass analyzer, with an  $80^\circ$  magnetic sector and an 8 cm radius of orbit fixed by the presence of entrance and exit slits. Magnetic field,  $\vec{B}$ , is oriented into the plane of the page. The resulting Lorentz force,  $\vec{F}$ , acts in a perpendicular fashion to both the incident trajectory of a positive ion with a speed,  $v$ , and the magnetic field.

these ions will generate an electrical signal,  $I_{m/z}$ , proportional to their number density inside the ion source. Alternatively, the intensity corresponding to a particular peak can be monitored as a function of time if the magnetic field and accelerating voltage are tuned to a constant value.

$$\vec{F} = ze(\vec{E} + \vec{v} \times \vec{B}) \quad 2.3$$

$$zevB = m \frac{v^2}{r} \quad 2.4a$$

$$\frac{m}{z} = \frac{er^2B^2}{2V} \quad 2.4b$$

In the case of the equilibrium process outlined in Eq. 1.1, a measure of the equilibrium constant can be obtained if the ion intensity of the reactant and product ions,  $I_A-$  and  $I_{AB}-$ , are recorded as a function of time. This is achieved by monitoring the discriminated and amplified output from the CEM by a multichannel scaler (MCS) card installed in a PC. The MCS card is triggered by the pulsed electron beam, and a series of successive intensity profiles are summed to reduce random scatter and improve the signal-to-noise ratio (typically  $10^3$  to  $10^4$  scans may be summed). Typical time intensity profiles for an association process such as the one given in Eq. 1.1 are shown in Figure 2.3.

From Figure 2.3, evidence that a state of chemical equilibrium has been reached can be seen in the decreasing nature of the two intensity-time profiles. The observed decrease in ion intensity is due to ions exiting the ion source through the electron beam entrance aperture

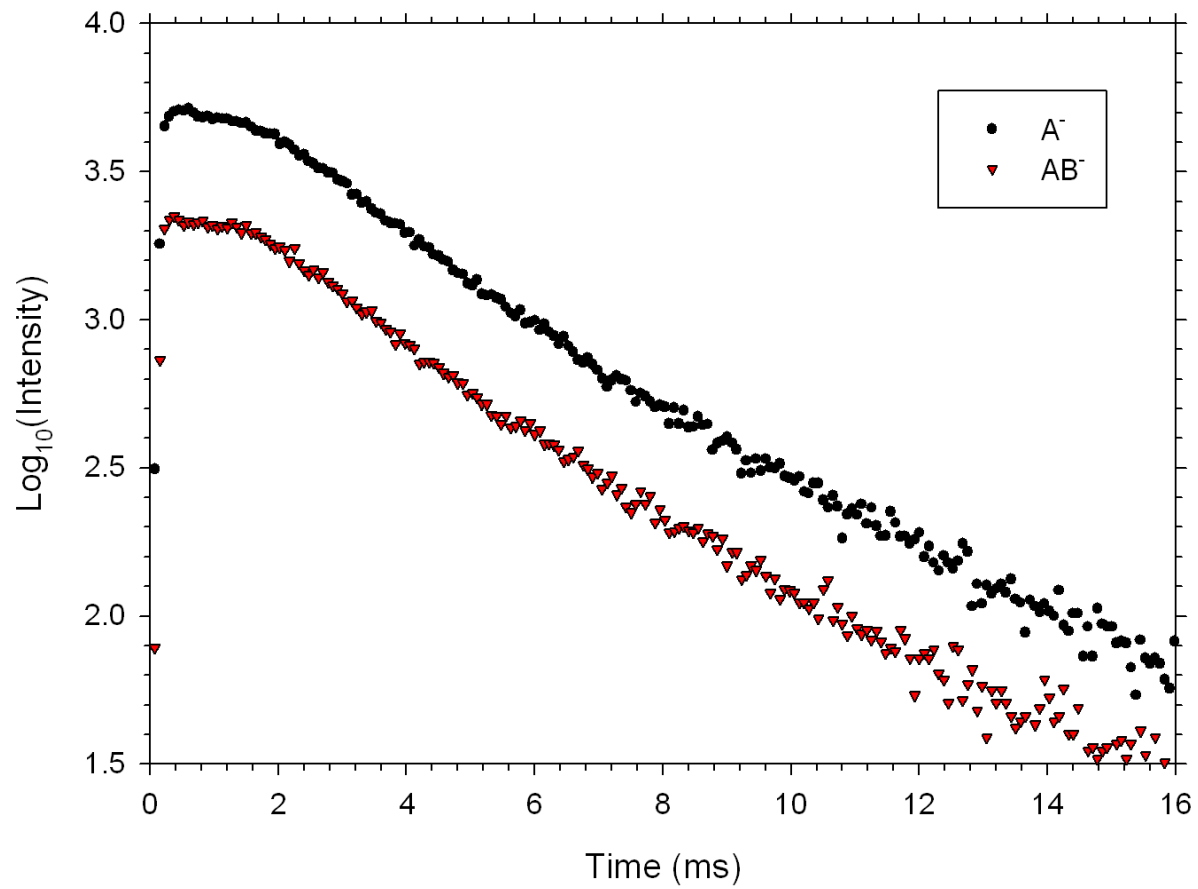


**Figure 2.3:** Typical intensity-time profiles shown on a logarithmic intensity scale. Ions  $A^-$  and  $AB^-$  correspond to species involved in the equilibrium clustering reaction such that ion  $A^-$  and a neutral B cluster together to form ion  $AB^-$ .

and ion exit aperture, chemical reaction to form another species, and through a discharge process occurring upon contact with the walls of the ion source.<sup>29</sup> Since the area of the two aperture holes are negligible in comparison to the area of the ion source walls, this source of ion depletion is considered to be negligible. If  $A^-$  and  $AB^-$  were involved in other reactions which compete with Eq. 1.1 the rate of consumption of the two ionic species would not be equal, except for rare cases. Hence, the discharging process taking place with the walls of the ion source should contribute a significant amount to the depletion of ion intensity.

It has been shown that the rate of signal depletion within the ion source due to diffusion to the walls is expected to follow an exponential decay<sup>24</sup>, just as observed in the experimentally-determined logarithmic intensity-time profiles of Figure 2.3. Since the diffusive processes taking place within the ion source are dependent upon mass, it would be expected that the heavier cluster ion would discharge to the walls more slowly than the lighter ion. Since both profiles are observed to decrease at the same rate, the two ions of significantly different mass must be diffusing toward the wall at the same rate. Since  $A^-$  and  $AB^-$  are constantly interconverting *via* Eq. 1.1, any one particular ion or molecule will be continually changing its chemical identity, so that a sort of average diffusion rate is achieved. This is strong evidence of the fact that  $A^-$  and  $AB^-$  are in chemical equilibrium.<sup>29</sup> If the ion intensity-time profiles are normalized to remove the common effect of the diffusion-controlled discharging of the ions, Eq. 2.5, the approach and attainment of equilibrium is easily visualized, Figure 2.4.

$$I_{norm,A^-} = \frac{I_{A^-}}{I_{A^-} + I_{AB^-}} \quad 2.5a$$

$$I_{norm,AB^-} = \frac{I_{AB^-}}{I_{A^-} + I_{AB^-}} \quad 2.5b$$

Since the partial pressure of an ionic species is directly proportional to the measured ion intensity for that species, the ratio of partial pressures of the ionic species can be equated to the ratio of measured ion intensities, as in Eq. 2.6. A functional form of the equilibrium constant, Eq. 2.7, is obtained by substitution of Eq. 2.6 into Eq. 1.6. Thus, if the ion intensities are measured and the partial pressure of the neutral molecule B is known, then the equilibrium constant can be measured. If such measurements are made at a series of temperatures, a van't Hoff plot can be generated and the standard change in enthalpy and entropy can be obtained.

$$\frac{I_{AB^-}}{I_{A^-}} = \frac{P_{AB^-}}{P_{A^-}} \quad 2.6$$

$$K_{eq} = \frac{I_{C^-}}{I_{A^-} \cdot P_B} \cdot P_o \quad 2.7$$

An interesting consequence of ion generation within a PHPMS ion source is that all thermodynamically accessible isomers will be present and, provided there are no kinetic

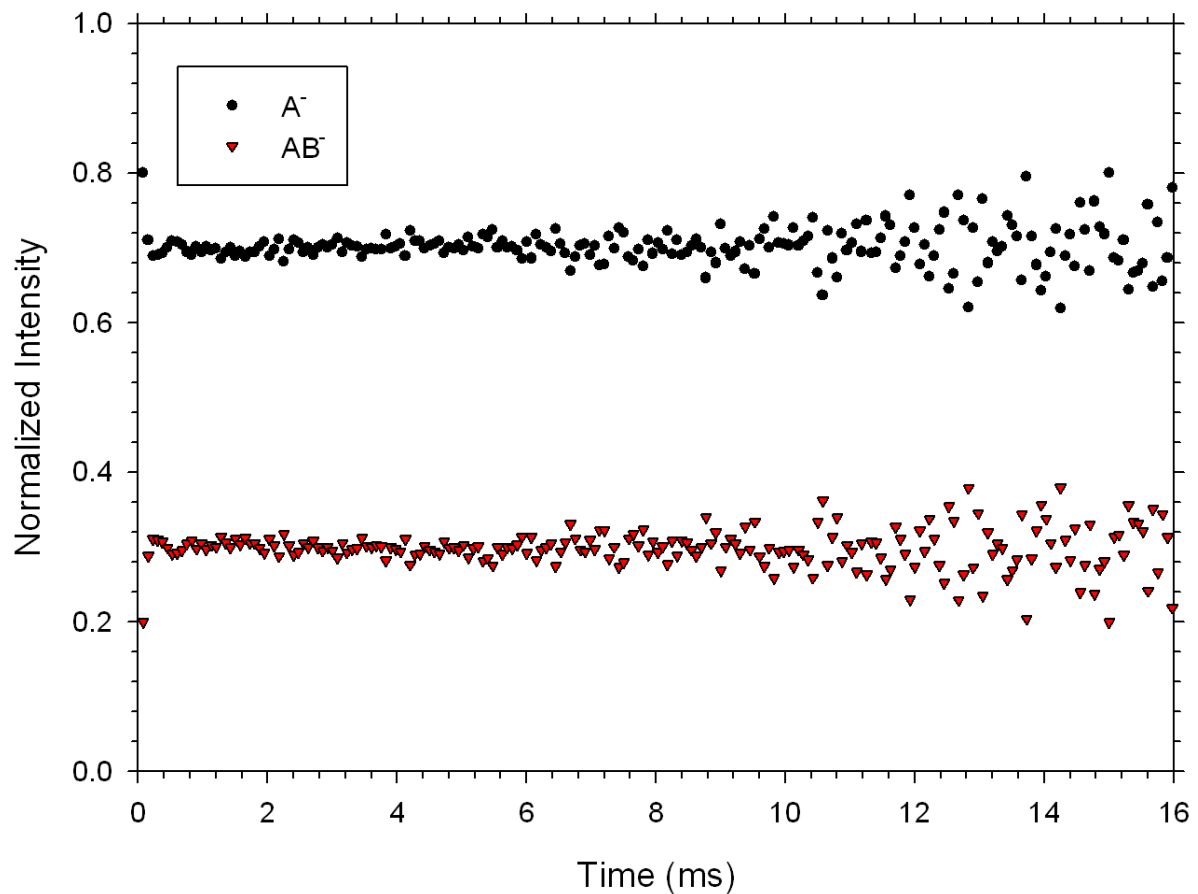


**Figure 2.4:** Typical normalized intensity-time profiles for the clustering of  $A^-$  with B to form  $AB^-$ . The two profiles becoming parallel within 0.5 ms of ion formation indicates a rapid establishment of equilibrium.

barriers to their interconversion, the relative abundance of each will be determined by Boltzmann statistics. Specifically, the relative abundance for a distribution of isomers can be determined *via* Eq. 2.8, where  $A_i$  and  $A_j$  are the relative abundances of the  $i^{\text{th}}$  isomer and the most stable isomer  $j$ , and  $\Delta G_i^\circ - \Delta G_j^\circ$  is the difference in their free energies of formation.

$$A_i = A_j e^{\frac{-(\Delta G_i^\circ - \Delta G_j^\circ)}{RT}} \quad 2.8$$

For instance, at 298 K, any isomer more than 10 kJ·mol<sup>-1</sup> higher in energy than the most stable isomer will possess a number density less than 2% than that of the most stable isomer. In such cases of low abundance, contributions from these other isomers can be considered to be negligible and measured thermodynamic properties can be attributed to that of the lowest energy isomer. In chemical systems where more than one isomer is present in significant amount (i.e. nearly equivalent free energy of formation to that of the lowest energy isomer at a given temperature), then consideration of possible isomeric effects should be taken into account.

Previous PHPMS investigations have demonstrated that isomerization can lead to changes in the measured thermochemical properties of a system in equilibrium. The first such evidence of this was observed by Hiraoka and Kebarle,<sup>33</sup> in which clusters of C<sub>2</sub>H<sub>5</sub><sup>+</sup> and H<sub>2</sub> were able to isomerize into a covalently bonded C<sub>2</sub>H<sub>7</sub><sup>+</sup> species at higher temperatures. Subsequently, while investigating the interaction between t-C<sub>4</sub>H<sub>9</sub><sup>+</sup> and i-C<sub>4</sub>H<sub>10</sub>, Sunner, *et al.*,<sup>34</sup> were able to observe an isomerization of a tightly bound species (at low temperatures)

into a more weakly bound cluster (at higher temperatures). Szulejko and McMahon<sup>35</sup> have also observed isomerization in PHPMS investigations of the equilibrium clustering of methylated acetone with acetone and dimethyl ether. Norrman and McMahon<sup>36</sup> have shown that over a broad temperature range, clusters of t-butyl cation with small organic molecules also exhibited a shift in isomeric distribution. In all of the above cases, the temperature dependent shift in isomeric distribution was a result of one isomer having a significant entropic advantage and, thus, was favored at high temperature, while another possessed a significant enthalpic advantage and was favored at lower temperatures. Such behavior led to the observation of bent van't Hoff plots whose two linear portions were defined by the thermochemical properties of the dominant isomer in a particular temperature range.

Apart from these bent van't Hoff plots, other interesting thermochemical consequences of isomerization may be encountered. If a collection of isomers with similar free energies of formation is present over a large enough temperature range, and no major shift in the isomeric distribution takes place, then linear van't Hoff plots can be observed. From these plots, the changes in enthalpy and entropy for the equilibrium process examined are obtained in the conventional way, but the measured change in entropy would then be considered to include the entropy of mixing for the collection of isomers. Such a treatment has recently been applied by Akrou, *et al.*, in the investigation of neutral and protonated 2,4 pentanedione, 2,5 hexanedione and methyl acetoacetate using the kinetic method.<sup>37</sup> To compensate for entropy of mixing, a correction term,  $\Delta S_{mix}^\circ$ , was included such that the experimentally observed entropy change for a reaction of interest,  $\Delta S_{exp}^\circ$ , was related to that of the most stable isomer (msi),  $\Delta S_{msi}^\circ$ , as shown in Eq. 2.9.

$$\Delta S_{exp}^{\circ} = \Delta S_{msi}^{\circ} + \Delta S_{mix}^{\circ} \quad 2.9$$

An expression for  $\Delta S_{mix}^{\circ}$  has been derived by the statistical thermodynamic modeling of the entropy change associated with  $N$  isomers of equal abundance being isothermally expanded into a common volume, Eq. 2.10. The resulting correction term depends on both the mole fraction of each isomer,  $x_i$ , as well as the number of different isomers present,  $N$ , and  $R$ , the ideal gas constant. In order to compensate for such an effect, an *a priori* knowledge of all isomers present within the system would be required, otherwise, it would be generally noted that any measured  $\Delta S_{exp}^{\circ}$  would contain within it  $\Delta S_{mix}^{\circ}$ . Since  $x_i$  is always a value between 0 and 1,  $\Delta S_{mix}^{\circ}$  is always  $\geq 0$ , therefore any comparison of  $\Delta S_{exp}^{\circ}$  to  $\Delta S_{msi}^{\circ}$ , would show  $\Delta S_{exp}^{\circ}$  to be more positive. Should  $N$  thermochemically equivalent isomers exist, then  $x_i = 1/N$  and Eq. 2.10 reduces to Eq. 2.11

$$\Delta S_{mix}^{\circ} = -R \sum_{i=1}^N x_i \ln(x_i) \quad 2.10$$

$$\Delta S_{mix}^{\circ} = R \ln N \quad 2.11$$

The treatment of the measured entropy of reaction used by Akrour, et. al., bears resemblance to that which has been applied in a computational study of hydrocarbons at equilibrium by Alberty, *et al.*<sup>38</sup>. In this case, the so-called “isomer group” thermodynamic

properties<sup>39-45</sup> were calculated such that a single value of enthalpy, entropy and Gibbs free energy of formation were used to describe the thermodynamics of a mixture of isomers. These isomer group properties were expressed in terms of the thermochemical properties of the individual isomers, and had the advantage of greatly reducing the complexity of the calculations necessary to describe the equilibrium composition of a system.

## 2.2 Quantum Chemical Calculations

As a complement to the measured thermochemical properties obtained from PHPMS, *ab initio* and density functional theory calculations (collectively known as electronic structure calculations) were performed, which provide energetic and structural details for any species of interest. The commercially available quantum chemical software package GAUSSIAN 03<sup>46</sup>, was employed to determine the electronic energy, equilibrium structure, vibrational frequencies and thermochemical variables for all molecules and ions of interest. A brief overview of some key methods used by GAUSSIAN 03, namely *ab initio* methods and density functional theory, is given below. In addition, the GaussView 3.0<sup>47</sup> software package was used to create initial guesses at molecular/ionic structures necessary for input into, as well as to generate visual representations of the optimized equilibrium structures outputted by, the GAUSSIAN 03 program.

### 2.2.1 Electronic Structure Calculations

The premise on which electronic structure calculations are based is the application of quantum mechanics to solve the time-dependent or –independent Schrödinger equation, Eq.

2.12 or Eq. 2.13, for a collection of particles of interest (i.e. a molecule or ion). By providing the program with an initial guess at the structure of a molecule, it will minimize its electronic energy by iteratively altering the input geometry and finding approximate solutions to the associated Schrödinger equation. Once this optimized structure is found, various statistical thermodynamic properties can be determined since the electronic energy, vibrational frequencies, bond lengths and angles for the equilibrium structures are then known. Only the time-independent Schrödinger equation will be discussed since those variables necessary to calculate the thermochemical properties for a reaction can be considered time-independent.<sup>48</sup>

$$\hat{H}\Psi(\vec{r}, t) = i\hbar \frac{\partial\Psi(\vec{r}, t)}{\partial t} \quad 2.12$$

$$\hat{H}\Psi(\vec{r}) = E\Psi(\vec{r}) \quad 2.13$$

The time-independent Schrödinger equation, Eq. 2.13, can be described as a multivariable differential equation in which the energy of the system being described,  $E$ , is obtained as an eigenvalue solution to the eigenfunction,  $\Psi(\vec{r})$  (or wavefunction, as it is commonly known), when operated on by the total energy operator, also known as the Hamiltonian,  $\hat{H}$ . The wavefunction,  $\Psi(\vec{r})$ , and its eigenvalues are dependent on the position,  $\vec{r}$ , of all constituent electrons and nuclei. In order to determine the total energy of the system both the Hamiltonian and the wavefunction must be specified. Unfortunately, the

equations resulting from an exact description of a non-trivial system are too complex and no analytic solutions to them have been found. Thus, several approximations must be made in order to find the wavefunctions and associated energy eigenvalues for an exactly defined Schrödinger equation. Some of the more important details and approximations necessary to solve the Schrödinger equation are discussed below; however, a full description of the implementation of these approximations is beyond the scope of this thesis.

### 2.2.1.1 The Hamiltonian Operator

The total energy operator,  $\hat{H}$ , for electrons interacting with nuclei is obtained by combining the kinetic energy operator,  $\hat{T}$ , and the potential energy operator,  $\hat{V}$ , as seen in Eq. 2.14. The kinetic energy operator is given in Eq 2.15, and is constructed by summing the kinetic energy contributions from all  $k$  electrons and nuclei. The potential energy operator, Eq. 2.16, is obtained by summing all of the various potentials arising from the Coulombic forces of attraction and repulsion between the electrons and nuclei. In Eq. 2.15 and Eq. 2.16,  $\hbar$  is Planck's constant divided by  $2\pi$ ,  $m_k$  is the mass of the  $k^{\text{th}}$  particle,  $\varepsilon_0$  is the permittivity of free space,  $Z_i$  is the charge of the  $i^{\text{th}}$  particle,  $e$  is the elementary charge, and  $\Delta r_{ij}$  is the separation between the  $i^{\text{th}}$  and  $j^{\text{th}}$  particles. The first term in Eq. 2.16 describes the interaction between the electrons and nuclei, while the second and third terms describe the interactions between electrons and between nuclei, respectively.<sup>48</sup>

$$\hat{H} = \hat{T} + \hat{V} \quad 2.14$$

$$\hat{T} = -\frac{\hbar^2}{2} \sum_k \frac{1}{m_k} \left( \frac{\partial^2}{\partial x_k^2} + \frac{\partial^2}{\partial y_k^2} + \frac{\partial^2}{\partial z_k^2} \right) \quad 2.15$$

$$\hat{V} = \frac{1}{4\pi\epsilon_0} \left( \sum_l^{electrons} \sum_M^{nuclei} \frac{Z_l Z_M e^2}{\Delta r_{lM}} + \sum_l^{electrons} \sum_m^{electrons} \frac{Z_l Z_m e^2}{\Delta r_{lm}} + \sum_L^{nuclei} \sum_M^{nuclei} \frac{Z_L Z_M e^2}{\Delta r_{LM}} \right) \quad 2.16$$

In all but the most trivial of cases, direct use of this full Hamiltonian in the Schrödinger equation will lead to differential equations without analytic solutions, thus approximations must be made. The assumption that the much more massive nuclei move significantly slower than the light electrons leads to what is known as the Born-Oppenheimer approximation. This allows for the separation of the nuclear and electronic kinetic energy components of the system, and a significant reduction in the complexity of the problem.<sup>48</sup> Another considerable difficulty encountered is a result of the contributions from electron-electron interactions. The presence of the second term in Eq. 2.16 makes exact solution of the Schrödinger equation extremely difficult, unless simplifying assumptions are made. For instance, in Hartree-Fock theory electron correlation is modeled as an electron interacting with an average electric field.<sup>25</sup> This over-simplification can lead to major errors in the calculated electronic energy and is really only applicable for the smallest and simplest of systems. In Møller-Plesset perturbation theory, electron correlation is treated as a perturbation to the Hartree-Fock Hamiltonian.<sup>49</sup> As in other perturbation methods, the exact solution to the Schrödinger equation is obtained when infinite recursive solutions are made.

This is clearly not possible, but fortunately even when solutions are obtained to the second order the accuracy of the electronic energy is greatly improved. While higher order solutions do further improve the accuracy, the computational costs of doing so rapidly increase.<sup>49</sup> Thus, it is clear that the different ways in which electronic structure methods handle electron-electron interactions is one of the most significant causes for their widely varying accuracy.<sup>25</sup>

### 2.2.1.2 The Wavefunction

Another variable which can greatly influence the accuracy of a calculation is the specification of  $\Psi(\vec{r})$ . Through the use of orbital theory as laid out by Hartree, Fock and Slater, the wavefunction,  $\Psi(\vec{r})$ , for a species containing n electrons can be represented as an  $n \times n$  Slater determinant of molecular orbitals,  $\phi$ , and electronic spin functions,  $\alpha$  and  $\beta$  as in Eq. 2.17, where  $\vec{r}_n$  specifies the position of the electron.<sup>25</sup> The determinantal nature of this formulation ensures that the symmetry rules for the exchange of any two particles are preserved.<sup>48</sup>

$$\Psi(\vec{r}) = \frac{1}{\sqrt{n!}} \begin{vmatrix} \phi_1(\vec{r}_1)\alpha(1) & \phi_1(\vec{r}_1)\beta(1) & \phi_2(\vec{r}_1)\alpha(1) & \phi_2(\vec{r}_1)\beta(1) & \cdots & \phi_{\frac{n}{2}}(\vec{r}_1)\alpha(1) & \phi_{\frac{n}{2}}(\vec{r}_1)\beta(1) \\ \phi_1(\vec{r}_2)\alpha(2) & \phi_1(\vec{r}_2)\beta(2) & \phi_2(\vec{r}_2)\alpha(2) & \phi_2(\vec{r}_2)\beta(2) & \cdots & \phi_{\frac{n}{2}}(\vec{r}_2)\alpha(2) & \phi_{\frac{n}{2}}(\vec{r}_2)\beta(2) \\ \vdots & \vdots & \vdots & \vdots & \ddots & \vdots & \vdots \\ \phi_1(\vec{r}_i)\alpha(i) & \phi_1(\vec{r}_i)\beta(i) & \phi_2(\vec{r}_i)\alpha(i) & \phi_2(\vec{r}_i)\beta(i) & \cdots & \phi_{\frac{n}{2}}(\vec{r}_i)\alpha(i) & \phi_{\frac{n}{2}}(\vec{r}_i)\beta(i) \\ \phi_1(\vec{r}_j)\alpha(j) & \phi_1(\vec{r}_j)\beta(j) & \phi_2(\vec{r}_j)\alpha(j) & \phi_2(\vec{r}_j)\beta(j) & \cdots & \phi_{\frac{n}{2}}(\vec{r}_j)\alpha(j) & \phi_{\frac{n}{2}}(\vec{r}_j)\beta(j) \\ \vdots & \vdots & \vdots & \vdots & \ddots & \vdots & \vdots \\ \phi_1(\vec{r}_n)\alpha(n) & \phi_1(\vec{r}_n)\beta(n) & \phi_2(\vec{r}_n)\alpha(n) & \phi_2(\vec{r}_n)\beta(n) & \cdots & \phi_{\frac{n}{2}}(\vec{r}_n)\alpha(n) & \phi_{\frac{n}{2}}(\vec{r}_n)\beta(n) \end{vmatrix} \quad 2.17$$

Certain calculation methods, such as those of Hartree-Fock theory, utilize a single determinant to approximate the wavefunction, while more advanced theories often use multiple determinants. Generally speaking, using multiple determinants allows for a more exact representation of the true wavefunction in a manageable way. Møller-Plesset perturbation theory, for instance, approximates  $\Psi(\vec{r})$  as a linear combination of Slater determinants derived from Hartree-Fock theory, Eq. 2.18.<sup>49</sup> The variable,  $\lambda$ , is a result of describing the exact Hamiltonian as being the Hartree-Fock Hamiltonian,  $\hat{H}_{HF}$ , plus a small perturbing operator,  $\hat{P}$ . The resulting energies are also expressed as a series in terms of the Hartree-Fock energies and the perturbation factor,  $\lambda$ .

$$\Psi(\vec{r}) = \Psi_{HF}^{(0)} + \lambda \Psi_{HF}^{(1)} + \lambda^2 \Psi_{HF}^{(2)} + \dots \quad 2.18$$

$$\hat{H} = \hat{H}_{HF} + \lambda \hat{P} \quad 2.19$$

$$E_{MP}^{(n)} = E_{HF}^{(0)} + \lambda E_{HF}^{(1)} + \lambda^2 E_{HF}^{(2)} + \dots \quad 2.20$$

Regardless of whether a single or multiple determinant representation of the full wavefunction is used, the knowledge of all molecular orbitals found within the molecule is required. Since these are not known exactly, yet another approximation must be made in order to continue on with the solution of the Schrödinger equation. These molecular orbitals can be approximated by a linear combination of  $N$  functions,  $\chi(\vec{r})$ , as seen in Eq. 2.21.<sup>48</sup>

These functions are known as basis functions, the collection of which is referred to as the basis set, and must be specified when defining the calculation method to be used. One of the most common forms of the basis functions is the contracted gaussian function, which can be seen in Eq. 2.22, where  $g_p(\vec{r})$  are the known primitive gaussian functions, shown in Eq. 2.23.<sup>48</sup> In Eq. 2.21 – Eq. 2.23  $d_{\mu p}$ ,  $c$ ,  $n$ ,  $m$ ,  $l$  and  $\alpha$  are all constants optimized for each particular type of orbital within a given basis set. Although a single gaussian type orbital is not the most accurate representation of an orbital, a linear combination of a sufficient number of these functions will yield an accurate representation. This is an important characteristic since analytic solutions to all integrals occurring within SCF theory can be obtained when gaussian type orbitals are used.<sup>25</sup> Choice of basis set, and hence the number of contracted and primitive gaussians used to represent a molecular orbital, as well as the values of the associated constants, can greatly affect the accuracy of a calculation. The combination of Eq. 2.21 to Eq. 2.23 into one representative molecular orbital can be seen in Eq. 2.24. The use of these molecular orbitals to construct the Slater determinant representation of  $\Psi(\vec{r})$  thus reduces the task of solving the Schrödinger equation for  $\Psi(\vec{r})$  to one of finding the values of the expansion co-efficients<sup>48</sup>,  $c_{\mu i}$ , the details of which are not given.

$$\phi_i(\vec{r}) = \sum_{\mu=1}^N c_{\mu i} \chi_{\mu}(\vec{r}) \quad 2.21$$

$$\chi_{\mu}(\vec{r}) = \sum_{p=1} d_{\mu p} g_p(\vec{r}) \quad 2.22$$

$$g_p(\vec{r}) = cx^n y^m z^l e^{-\alpha r^2} \quad 2.23$$

$$\phi_i(\vec{r}) = \sum_{\mu=1}^N c_{\mu i} \left( \sum_{p=1} d_{\mu p} (cx^n y^m z^l e^{-\alpha r^2}) \right) \quad 2.24$$

### 2.2.1.3 Density Functional Theory

Through the use of density functional theory (DFT) it is possible to account for the effects of electron interactions in a very efficient manner. Since calculation methods employing DFT can obtain results that are equally accurate, or better, than those of *ab initio* methods, in a fraction of the time, they are being used more frequently and on larger and larger systems.<sup>50</sup> The use of the efficient DFT methods has allowed for systems up to 1000 atoms to be examined in unprecedented detail, but the most advanced DFT methods are still limited to the study of small systems. According to DFT, all molecular properties can be calculated if the electronic distribution within that molecule,  $\rho(\vec{r})$ , is known. The electron density for an  $n$ -electron species can be obtained from a sum of the molecular orbitals in the fashion seen in Eq. 2.25. Since the total electronic energy can be broken down into components resulting from various interactions, as done in Eq. 2.26, each can be described in terms of  $\rho(\vec{r})$ .<sup>51</sup> In Eq. 2.26,  $E_T$  represents the electronic contribution to the kinetic energy,  $E_V$  represents the potential energy associated with the nuclear-electron attraction and nuclear-

nuclear repulsion,  $E_J$  is the electron-electron repulsion term,  $E_X$  is the exchange energy associated with same-spin electron interactions, and  $E_C$  is the correlation energy arising from mixed spin interactions.

$$\rho(\vec{r}) = \sum_{i=1}^n \phi_i^*(\vec{r})\phi_i(\vec{r}) \quad 2.25$$

$$E = E_T + E_V + E_J + E_X + E_C \quad 2.26$$

Several different density functional models have been formulated over the years, providing many different expressions for each of the terms found within Eq. 2.26, all functions of  $\rho(\vec{r})$ . One of the most popular DFT models currently in use is B3LYP. This hybrid model, introduced by Becke, combines both  $\rho(\vec{r})$  and the molecular orbitals,  $\phi_i(\vec{r})$ , to solve for the total electronic energy for an  $n$  electron and  $M$  nuclei system, as outlined in Eq. 2.27.<sup>51</sup> The energy functionals of Eq. 2.27 corresponding to the kinetic, potential, and exchange energies are given in Eq. 2.28 to Eq. 2.33,<sup>51</sup> while the explicit form of  $E_C^{VWN}$  and  $E_C^{LYP}$  are very complicated and not shown. Expressions for  $E_C^{VWN}$  and  $E_C^{LYP}$  are reported by Parr, *et al.*,<sup>52</sup> and Lee, *et al.*<sup>53</sup>.

$$E^{B3LYP} = E_T^{H28} + E_V + E_J + (1 - c_1)E_X^{D30} + c_1 E_X^{F30} + c_2 \Delta E_X^{B88} + (1 - c_3)E_C^{VWN} + c_3 E_C^{LYP} \quad 2.27$$

$$E_T^{H28} = -\frac{1}{2} \sum_i^n \int \phi_i(\vec{r}) \nabla^2 \phi_i(\vec{r}) d\vec{r} \quad 2.28$$

$$E_V = - \sum_a^M Z_a \int \frac{\rho(\vec{r})}{|\vec{r} - \vec{R}_a|} d\vec{r} \quad 2.29$$

$$E_J = \frac{1}{2} \int \int \frac{\rho(\vec{r}_1)\rho(\vec{r}_2)}{|\vec{r}_1 - \vec{r}_2|} d\vec{r}_1 d\vec{r}_2 \quad 2.30$$

$$E_X^{D30} = -\frac{3}{2} \left( \frac{3}{4\pi} \right)^{1/3} \int (\rho_\alpha(\vec{r}))^{\frac{4}{3}} d\vec{r} \quad 2.31$$

$$E_X^{F30} = -\frac{1}{2} \sum_i^n \sum_j^n \int \int \frac{\phi_i(\vec{r}_1)\phi_j(\vec{r}_1)\phi_i(\vec{r}_2)\phi_j(\vec{r}_2)}{|\vec{r}_1 - \vec{r}_2|} d\vec{r}_1 d\vec{r}_2 \quad 2.32$$

$$\Delta E_X^{B88} = -b \int (\rho_\alpha(\vec{r}))^{\frac{4}{3}} \frac{x_\alpha^2}{1 + 6b(x_\alpha(\vec{r})) \sinh^{-1}(x_\alpha(\vec{r}))} d\vec{r} \quad 2.33$$

$$x_\alpha = \frac{|\nabla \rho_\alpha(\vec{r})|}{(\rho_\alpha(\vec{r}))^{\frac{4}{3}}} \quad 2.34$$

The three constants of Eq. 2.27,  $c_1$ ,  $c_2$ , and  $c_3$ , were obtained from fitting the model to experimental data. In Eq. 2.28 – Eq. 2.34,  $Z_a$  and  $\vec{R}_a$  are the nuclear charge and position of

the  $a^{\text{th}}$  nuclei,  $\vec{r}_i$  and  $\phi_i$  are the position and molecular orbital of the  $i^{\text{th}}$  electron,  $b$  is a constant, and  $\rho_\alpha$  is the spin polarized electron density.

#### 2.2.1.4 Calculation of Thermochemical Quantities

In order to calculate bulk thermochemical properties ( $\Delta H_{rxn}^\circ(T)$ ,  $\Delta S_{rxn}^\circ(T)$  and  $\Delta G_{rxn}^\circ(T)$ ) for an equilibrium reaction from the single-molecule energetic and structural details provided by electronic structure calculations, the common relations of statistical thermodynamics must be employed. Modern electronic structure calculation programs greatly simplify the task of obtaining these single-molecule properties, and when given the proper command, will also evaluate associated thermochemical quantities. A brief outline of the equations utilized by such programs is given below.

The basis for the calculation of the standard entropy, enthalpy and Gibbs free energy difference relative to absolute zero, Eq. 2.35 to Eq. 2.37, is the ability to express these macroscopic variables in terms of the molecular partition function,  $Q(T)$ .<sup>54</sup> In these equations  $N_A$  is Avogadro's number and  $k_B$  is the Boltzmann constant. The expression for the molecular partition function, Eq. 2.38, is crucial for the probabilistic description of the thermochemical properties in terms of the molecular energy levels,  $\epsilon_i$ .

$$S^\circ(T) - S^\circ(0) = S^\circ(T) = N_A k_B \left\{ \frac{\partial}{\partial T} [T \ln Q(T)] - \ln N_A + 1 \right\} \quad 2.35$$

$$H^\circ(T) - H^\circ(0) = N_A k_B T^2 \frac{\partial \ln[Q(T)]}{\partial T} + N_A k_B T \quad 2.36$$

$$G^\circ(T) - G^\circ(0) = -N_A k_B T \left\{ \ln \left[ \frac{Q(T)}{N_A} \right] \right\} \quad 2.37$$

$$Q(T) = \sum_i e^{-\frac{\epsilon_i}{k_B T}} \quad 2.38$$

The exact molecular energy levels are not generally known, but the translational, electronic, vibrational and rotational contributions to the molecular energy are readily obtained from electronic structure calculations.<sup>54</sup> Expressing the molecular energy as a sum of these contributions, Eq. 2.39, results in a molecular partition function that is expressed as a product of the translational, electronic, vibrational and rotation partition functions, Eq. 2.40.

$$\epsilon_i = \epsilon_i^{trans} + \epsilon_i^{elec} + \epsilon_i^{vib} + \epsilon_i^{rot} \quad 2.39$$

$$Q(T) = Q^{trans} Q^{elec} Q^{vib} Q^{rot} \quad 2.40$$

Each of these component partition functions is easily solved for within the electronic structure program if the equilibrium geometry and infrared (IR) vibrational frequencies are known. Details on how this is performed are not given, but rather a discussion of how to handle the output of the calculations is.

In order to calculate the properties of an equilibrium reaction such as Eq. 1.1, the difference in the stoichiometrically-scaled sums of properties for the products and reactants can be made. This approach is also referred to as the supermolecular approach.<sup>55</sup> Standard changes in enthalpy are computed according to Eq. 2.41, where  $\Delta E^{elec}$ ,  $\Delta E^{vib}$ ,  $\Delta E^{rot}$ , and  $\Delta E^{trans}$  are the differences in electronic, vibrational, rotational and translational energies between products and reactants,  $\Delta ZPE$  is the difference in zero point energies, and  $w$  is the pressure-volume work done in going from reactants to products. Under the isobaric conditions of the PHPMS ion source,  $w = P\Delta V = (-1)RT$  for the reaction outlined in Eq. 1.1.

$$\Delta H_{calc}^\circ(T) = \Delta E^{elec} + \Delta E^{vib} + \Delta E^{rot} + \Delta E^{trans} + \Delta ZPE + w \quad 2.41$$

Standard entropy changes are computed according to Eq. 2.42, where  $\sum_{products} S_i^\circ$  and  $\sum_{reactants} S_j^\circ$  represent the sums of translational, electronic, vibrational and rotational entropies over all product and reactant species, respectively.

$$\Delta S_{calc}^\circ(T) = \sum_{products} S_i^\circ(T) - \sum_{reactants} S_j^\circ(T) \quad 2.42$$

Once  $\Delta H_{calc}^\circ$  and  $\Delta S_{calc}^\circ$  are known, the change in Gibbs free energy can be determined *via* Eq. 2.43.

$$\Delta G_{calc}^\circ(T) = \Delta H_{calc}^\circ(T) - T\Delta S_{calc}^\circ(T) \quad 2.43$$

## **2.2.2 Describing Anionic Systems with Hydrogen Bonding**

In order to ensure that the results of electronic structure calculations accurately describe the system of interest, careful consideration must be given to the choice of both the theoretical model and basis set used. As noted above, several approximations can be employed by a particular model and large errors can be expected if those approximations over-simplify crucial interactions taking place within the system under investigation. Furthermore, even if a very detailed and appropriate theoretical model is used, poor agreement between theory and experiment can be expected unless an appropriate mathematical representation of the molecular orbitals and wavefunction is made. In general, large basis sets and highly correlated methods will give the best results. It is not always practical, or even possible, to use these since computational resource often cannot meet the demands of such a combination. Thus, one of the biggest difficulties in choosing a method and basis set is finding a combination that is both accurate and practical, so that all molecules/ions being investigated can be described.

When attempting to calculate the electronic properties of anions involved in hydrogen bonds several special considerations must be made. Even more so than in neutrals, electron-electron interactions in anions are of great importance since the extra electron(s) further increase the complexity of this problem. Thus it is absolutely essential that a model used to describe such a system should include electron correlation. *Ab initio* methods such as fully correlated second order Møller-Plesset perturbation theory (MP2(full)) or DFT methods such as B3LYP are two methods which pragmatically handle electron correlation in ions of moderate size, and as a result have been utilized in innumerable computational studies of

hydrogen bonding and anionic systems.<sup>19</sup> The MP2(full) and B3LYP methods, when combined with an appropriate basis set, have both been praised in their ability to recreate the energetic and geometric features of hydrogen bonded systems.<sup>19</sup> A comparison of these two methods shows that while MP2(full) often provides more accurate energy values, it is also the more computationally demanding method. On the other hand, B3LYP can efficiently recreate geometric features, but give a slightly poorer description of electron correlation.<sup>19</sup> A combination of these two methods can be employed in which the geometry of an ion/molecule of interest is iteratively optimized using the less demanding B3LYP and the electronic energy of this optimized structure is then evaluated using a single MP2(full) calculation. This pragmatic compound method should provide accurate descriptions of both the geometry and energy of anions involving hydrogen bonding.

Equally important to the choice of an appropriate level of theory is the choice of an appropriate basis set. Due to the extra electron repulsion found within the electron cloud of an anion, the molecular orbitals in which they are found are often larger than those of its neutral analog.<sup>48</sup> In addition, the presence of highly electronegative atoms within the anion can also result in poor agreement between theory and experiment since the molecular orbitals of these atoms are often more difficult to describe. It is common for basis sets describing anions involving electronegative atoms to include both diffuse and polarization functions to correctly account for electron repulsion and the resizing of molecular orbitals due to electronegative arguments.<sup>48</sup> The so-called Pople-style split basis sets can be employed, and are fully capable of compensating for these two effects. One often utilized basis set is 6-311++G(d,p), which has been acknowledged as being a good compromise between accuracy

and practicality in its ability to describe the molecular orbitals of anionic hydrogen bonding systems.<sup>19</sup> It is able to do so by adding diffuse and polarization functions to all heavy and light atoms within the molecule/ion.

With the above arguments in mind, all geometry and frequency calculations reported in this thesis were performed using the B3LYP level of theory with the 6-311++G(d,p) basis set. The electronic energies of these optimized structures were obtained by applying the fully correlated MP2(full) method, also using the 6-311++G(d,p) basis set. The conventional nomenclature of first stating the method and basis set used to calculate the electronic energy followed by the method and basis set used to calculate the geometry optimization will be used. Thus, the short hand notation for the compound method and basis set used in this thesis is MP2(full)/6-311++G(d,p)//B3LYP/6-311++G(d,p). As a test of the appropriateness of this method and basis set, the enthalpy and free energy of deprotonation of HF, CH<sub>3</sub>OH, and C<sub>2</sub>H<sub>5</sub>OH, as well as the fluoride attachment of HF, H<sub>2</sub>O, and CH<sub>3</sub>OH were calculated using various basis sets. The results of this comparison can be found in Table 2-1. It was confirmed that the combination of B3LYP/6-311++G(d,p) optimizations with MP2(full)/6-311++G(d,p) single point electronic energy calculations provided results in good agreement with literature. The suitability of this method can also be confirmed *a posteriori*, as will be seen from the excellent agreement between calculated and experimental thermochemical data reported in this thesis. In some cases an improvement in the agreement could be seen from an increase in the size of the basis set, but it is interesting to note that this was not always the case. Also, these larger basis sets proved to be too resource demanding for some of the larger clusters examined, thus justifying the use of the 6-311++G(d,p) basis set.

**Table 2-1: Validating the Choice of Method and Basis Set From a Comparison to Literature for Select Anionic Hydrogen Bonding Systems**

Reaction	Method	$\Delta_{rxn}H^\circ$ (kJ·mol <sup>-1</sup> )	$\Delta_{rxn}G_{298}^\circ$ (kJ·mol <sup>-1</sup> )	Ref
$HF \rightleftharpoons H^+ + F^-$	literature	1554	1529	a
	MP2/6-311++G(d,p)// B3LYP/6-311++G(d,p)	1552.8	1528.8	b
	MP2/6-311++G(3df,2pd)// B3LYP/6-311++G(3df,3pd)	1556.3	1532.3	b
$CH_3OH \rightleftharpoons H^+ + CH_3O^-$	literature	1597	1569	c
	MP2/6-311++G(d,p)// B3LYP/6-311++G(d,p)	1600.4	1573.2	b
	MP2/6-311++G(2df,2pd)// B3LYP/6-311++G(d,p)	1596.3	1566.1	b
$C_2H_5OH \rightleftharpoons H^+ + C_2H_5O^-$	literature	1583	1555	c
	MP2/6-311++G(d,p)// B3LYP/6-311++G(d,p)	1584.2	1554	b
$HF + F^- \rightleftharpoons FHF^-$	literature	-192	n/a	d
	MP2/6-311++G(d,p)// B3LYP/6-311++G(d,p)	-189.2	-157.4	b
	MP2/6-311++G(2df,2pd)// B3LYP/6-311++G(2df,2pd)	-197.6	-166	b
$H_2O + F^- \rightleftharpoons H_2O \cdots F^-$	literature	-114.6	-91.6	e
	MP2/6-311++G(d,p)// B3LYP/6-311++G(d,p)	-117	-89.5	b
	MP2/6-311++G(3df,3pd)// B3LYP/6-311++G(3df,3pd)	-124.8	-97.2	b
$CH_3OH + F^- \rightleftharpoons CH_3OH \cdots F^-$	literature	-124	-95	f
	MP2/6-311++G(d,p)// B3LYP/6-311++G(d,p)	-129.6	-101.1	b
	MP2/6-311++G(3df,2pd)// B3LYP/6-311++G(3df,3pd)	-140.3	-111.9	b

a – Blondel, et al.<sup>56</sup>

b – this work

c – Ramond, et al.<sup>57</sup>

d – Wenthold, et al.<sup>20</sup>

e – Weis, et al.<sup>58</sup>

f – Larson, et al.<sup>59</sup>

## Chapter 3

# Investigations of Strong Hydrogen Bonding in $(ROH)_n \cdots FHF^-$ ( $n = 1, 2$ and $R = H, CH_3, C_2H_5$ ) Clusters *via* High Pressure Mass Spectrometry and Quantum Calculations

### 3.1 Introduction

One hydrogen bonded system which has received much attention is that of the hydrogen bihalides,  $XHY^-$  ( $X, Y = F, Cl, Br$  or  $I$ ), whose simplicity allows for (sometimes excruciatingly) in depth examinations of these prototypical short strong hydrogen bonds (SSHBs). The well-documented thermochemical<sup>20,22,60-67</sup>, spectroscopic<sup>68-77</sup> and geometric<sup>65,67,68,71,74,76</sup> properties of these linear triatomic anions, as well as the acquisition of a fundamental understanding of the factors influencing their bonding, enable the establishment of a basis for the examination of more complex hydrogen bonding systems.

Of the  $XHY^-$  species, the bifluoride anion,  $FHF^-$ , has the strongest hydrogen bond in the group, and as such, has been extensively examined. The vibrational levels of this anion have been reported by Kawaguchi and Hirota<sup>68</sup> and its equilibrium F-F bond distance was determined to be 2.278 Å. High level computational studies have shown  $FHF^-$  to be linear with a symmetrically shared proton, giving it  $D_{\infty h}$  symmetry. Wenthold and Squires determined the strength of this bond to be 191.6 kJ · mol<sup>-1</sup> *via* kinetic method measurements of flowing afterglow collision induced dissociation (CID) experiments<sup>20</sup> which, in terms of strength, places this bond in the covalent regime. Despite the attention this simple triatomic anion has received, it is quite surprising to note that investigations of clusters involving this

ideal ionic hydrogen bond are limited to a short list of computational studies. Investigations into the stepwise clustering of  $\text{FHF}^-$  with  $(\text{ROH})_n$  ( $n=1,2$  R = H,  $\text{C}_2\text{H}_5$ ) have been performed by Li and Hamilton, *et al.*,<sup>78-80</sup> and showed that upon solvation the F-F distance becomes elongated and the proton in  $\text{FHF}^-$  is no longer symmetrically shared. Moreover, these two characteristics were indicative of a weakening of the  $\text{FHF}$  hydrogen bond, which, in the case of two water attachments, was by as much as  $79.1 \text{ kJ}\cdot\text{mol}^{-1}$ .

A closer look at the changes in hydrogen bond geometric properties seen in the reported structures of Li and Hamilton, *et al.*, were consistent with predictions of the traditional model of hydrogen bonding. Considering an ionic hydrogen bond to be comprised of a proton-donating AH moiety and a proton accepting B<sup>-</sup> moiety,  $\text{AH}\cdots\text{B}^-$ , if the acid strength of AH and the basicity of B<sup>-</sup> are raised, the hydrogen bond strength and linearity will increase while bond length will decrease. For instance, the addition of one water molecule to  $\text{FHF}^-$  was reported to lengthen the F-F distance by  $0.027 \text{ \AA}$  and cause a slight bending,  $\angle\text{FHF} = 179.2^\circ$ , at the B3LYP/6-311++G(d,p) level of theory<sup>80</sup>. This lengthening can be attributed to the formation of an OH $\cdots$ F hydrogen bond to  $\text{FHF}^-$ , causing a weakening of the basicity of the F<sup>-</sup> moiety.

Another observation from the calculations of Li and Hamilton, *et al.*, was the presence of several isomers (and/or low-lying transition states) of similar binding energy for each cluster examined. Any  $\text{FHF}^-\cdots(\text{ROH})_n$  clusters that are created under thermodynamic conditions are expected to consist of a distribution of accessible isomers and each isomer's number density will be determined by Boltzmann statistics. In such cases, entropic effects caused from the presence of a mixture of isomers can be expected whose contribution would be dependent on

both the mole fraction of each isomer, as well as the number of different isomers present. As outlined in Section 2.1, the correction for this effect involves the addition of the entropy of mixing, otherwise uncorrected values of  $\Delta S_{rxn}^\circ$  would be more positive than that calculated for the formation of the most stable isomer.

In order to contribute to the vast amount of literature available, a high pressure mass spectrometric (HPMS) study of the stepwise clustering of FHF<sup>-</sup> with (ROH)<sub>n</sub> solvents has been performed, where n = 1, 2 and R = H, CH<sub>3</sub>, C<sub>2</sub>H<sub>5</sub>. Experimental gas-phase thermochemical data pertaining to these systems have been measured and compared to *ab initio* and density functional theory calculations for various structures of interest. These studies provide further insight into the nature of the SSHB, the importance of which warrants thorough investigation of this hydrogen bond-rich system.

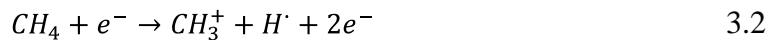
### 3.2 Experimental Methods

All thermodynamic measurements were made using a high pressure mass spectrometer (HPMS) configured around a VG 8-80 single magnetic sector mass analyzer and a homebuilt pulsed-ionization high pressure ion source, which has been described in detail in Section 2.1.

A mixture of 1% NF<sub>3</sub> in CH<sub>4</sub> and varying amounts of the desired protic solvents (solvent partial pressure between .01% and 1% of total pressure) was flowed into the ion source at pressures between 6 and 7 torr and temperatures between 40 °C and 140 °C, depending on the equilibrium reaction being examined. NF<sub>3</sub>, CH<sub>4</sub> (99.97% purity), CH<sub>3</sub>OH (99.8% purity) and C<sub>2</sub>H<sub>5</sub>OH were purchased from Ozark-Mahoning, Praxair, Sigma Aldrich and Commercial Alcohols Inc. , respectively, and used as supplied without any further

purification, while any H<sub>2</sub>O used was purified using a Milli-Q filtration system. Upon bombardment of this reactant gas mixture with a pulsed electron beam of 2 kV, defined by 60 µs long bursts with a period of 60 ms, the desired anionic species were produced within the ion source through the series of ion molecule reactions proposed below, Eq. 3.2 – Eq. 3.6.

Initial electron bombardment of CH<sub>4</sub> liberates hydrogen atoms and two low-energy secondary electrons, Eq. 3.2. These secondary electrons can combine with NF<sub>3</sub> and, through the process of dissociative electron capture, form an abundance of F<sup>-</sup>, Eq. 3.3, while the hydrogen atoms formed in Eq. 3.2 can abstract fluorine from another molecule of NF<sub>3</sub> to form HF, Eq. 3.4. The presence of both F<sup>-</sup> and HF within the ion source leads to the formation of FHF<sup>-</sup>, Eq. 3.5. Once FHF<sup>-</sup> has been formed it is free to undergo a sequential solvation process with ROH, Eq. 3.6, where R = H, CH<sub>3</sub> or C<sub>2</sub>H<sub>5</sub> and n = 1 and 2.



At the experimental temperatures and pressures used, all newly formed hot ions undergo approximately  $10^8$  collisions before diffusing out of the ion source and being accelerated onto the detector, thus ensuring that all species had been thermalized to the known temperature of the ion source.

A typical  $\log_{10}(\text{intensity})$ -time profile is depicted in Figure 3.1 and was collected for the pair of ions involved in Eq. 3.6, while the inset shows typical normalized intensity-time profiles. Each plot was the result of an accumulation of ion intensity as a function of time after 2000 successive electron beam pulses. The time required for the ion formation process outlined in Eq. 3.2 – Eq. 3.6 is reflected in the collected profiles as a 0.5 ms delay between the end of the electron beam pulse ( $t = 0$  ms) and the onset of the first observed ion signals. From these intensity-time profiles it can be seen that equilibrium is reached approximately 1.5 ms after the electron beam was turned off, or approximately 1 ms after the ions of interest first appear in the source.

By taking the ratio of product to reactant ion intensities during the period in which the two ions were in equilibrium (after 1.5 ms), and dividing by the partial pressure of the neutral solvent gas, a measure of the equilibrium constant at a given temperature was obtained. Provided that no significant changes in heat capacity or any major shift in isomeric distribution occurs over a particular temperature range, a plot of  $\ln(K_{\text{eq}})$  versus  $T^{-1}$  can be expected to be linear with enthalpy change found from the slope and entropy change found from the intercept.

Six to ten measurements of  $K_{\text{eq}}$  were obtained at each temperature and the standard deviation displayed as error bars for each point as shown in the resulting van't Hoff plots.

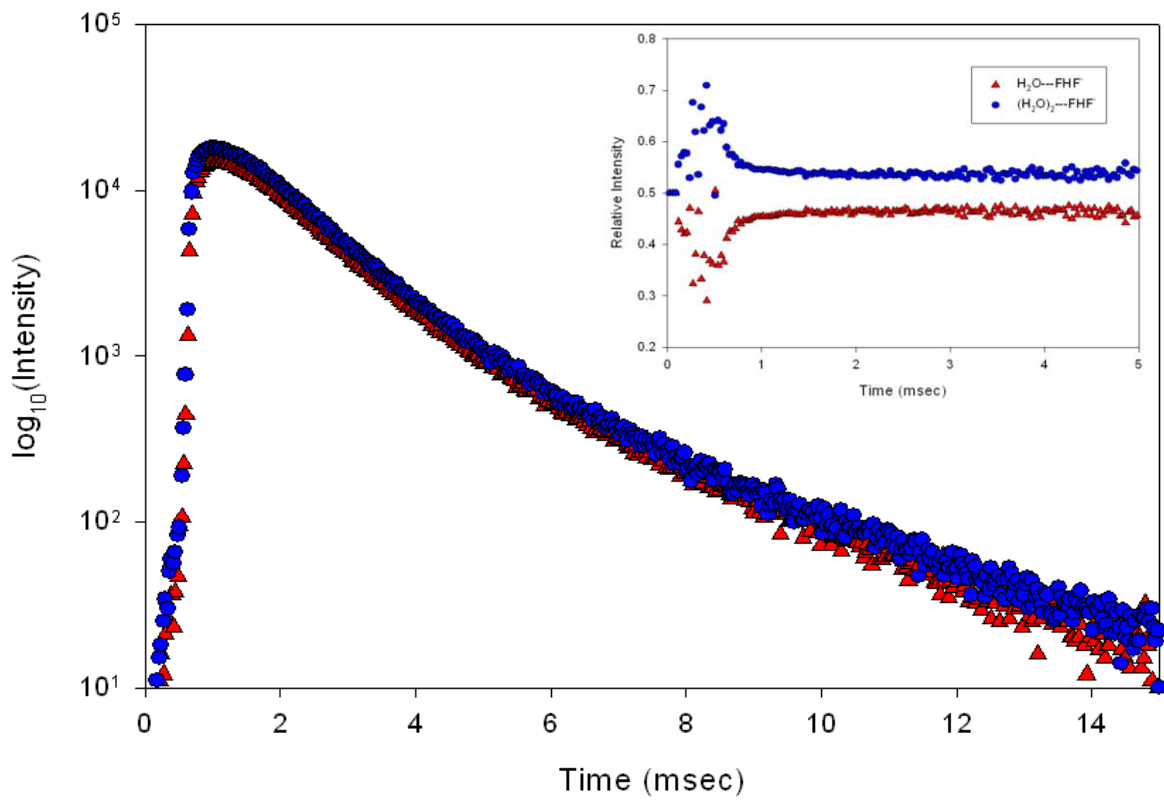


**Figure 3.1:** Typical  $\log_{10}(\text{intensity})$ -time profiles for the ion clusters of  $\text{FHF}^-$  with one and two water molecules. *Inset:* Normalized intensity-time profiles.

Temperature measurements were performed using a J-type thermocouple with an accuracy of  $\pm 1$  K. Estimated errors of  $\pm 2.0$  kJ·mol<sup>-1</sup>,  $\pm 10$  J·K<sup>-1</sup>·mol<sup>-1</sup> and  $\pm 4.1$  kJ·mol<sup>-1</sup> in  $\Delta H_{exp}^\circ$ ,  $\Delta S_{exp}^\circ$  and  $\Delta G_{exp,298}^\circ$ , respectively, are based on the propagation of uncertainties in temperature and pressure measurements for the experiment.

Calculations were performed to complement the HPMS measurements and gain further insight into the energetic and structural properties of the anion-protic solvent clustering process. Values for  $\Delta H_{calc}^\circ$ ,  $\Delta S_{calc}^\circ$  and  $\Delta G_{calc,298}^\circ$  associated with Eq. 3.6 were calculated as detailed in Section 2.2.1.4. In all systems examined, several thermodynamically accessible isomers and rotamers exist on the potential energy surface for each cluster. Only the thermochemical properties of those structures found to be of importance (i.e. enthalpically, entropically, or ergonomically favorable species) are reported below.

### 3.3 Results and Discussion

#### 3.3.1 Step-wise Solvation of FHF<sup>-</sup> by H<sub>2</sub>O

The van't Hoff plots obtained for the stepwise clustering of one and two water molecules to FHF<sup>-</sup> are shown in Figure 3.1, and associated thermochemical properties, both measured and calculated, are reported in Table 3-1.  $\Delta H_{exp}^\circ$  and  $\Delta S_{exp}^\circ$  for the addition of the first water molecule to FHF<sup>-</sup> were determined to be  $-78.6 \pm 2.0$  kJ·mol<sup>-1</sup> and  $-107.9 \pm 10.0$  J·K<sup>-1</sup>·mol<sup>-1</sup>, respectively, *via* HPMS, while calculations determine  $\Delta H_{calc}^\circ$  to be -68.7 kJ·mol<sup>-1</sup> and  $\Delta S_{calc}^\circ$  to be -86.6 J·K<sup>-1</sup>·mol<sup>-1</sup>. Using both the HPMS data and calculated values, changes

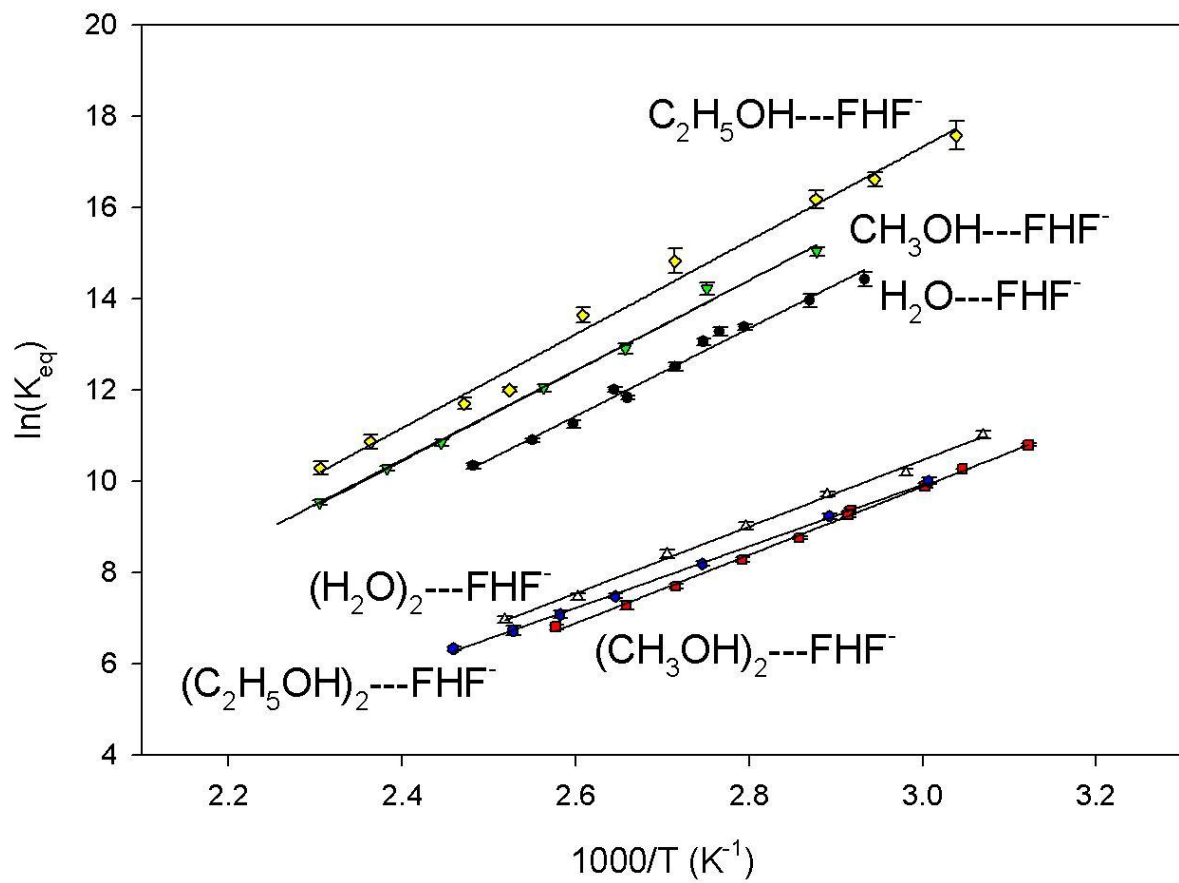


**Figure 3.2: van't Hoff plots for the sequential clustering of one and two water, methanol and ethanol molecules to  $\text{FHF}^-$ .**

**Table 3-1:Measured and Calculated Thermochemical Properties for Examined Clustering Processes.**

Reaction	$\Delta H_{rxn}^\circ$ (kJ·mol <sup>-1</sup> )	$\Delta S_{rxn}^\circ$ (J·K <sup>-1</sup> ·mol <sup>-1</sup> )	$\Delta G_{298}^\circ$ <sup>†</sup> (kJ·mol <sup>-1</sup> )	method
$FHF^- + H_2O \rightleftharpoons H_2O \cdots FHF^-$	$-78.6 \pm 2.0$	$-107.9 \pm 10.0$	$-46.4 \pm 4.1$	a
	-68.7	-86.6	-42.8	b
$H_2O \cdots FHF^- + H_2O \rightleftharpoons (H_2O)_2 \cdots FHF^-$	$-60.7 \pm 2.0$	$-95.0 \pm 10.0$	$-32.4 \pm 4.1$	a
	-58.9	-96.2	-30.2	b
$FHF^- + CH_3OH \rightleftharpoons CH_3OH \cdots FHF^-$	$-81.3 \pm 2.0$	$-108.1 \pm 10.0$	$-49.1 \pm 4.1$	a
	-73.2	-84.5	-48.0	b
$CH_3OH \cdots FHF^- + H_2O \rightleftharpoons (CH_3OH)_2 \cdots FHF^-$	$-64.0 \pm 2.0$	$-104.9 \pm 10.0$	$-32.7 \pm 4.1$	a
	-61.2	-106.3	-29.6	b
$FHF^- + C_2H_5OH \rightleftharpoons C_2H_5OH \cdots FHF^-$	$-86.4 \pm 2.0$	$-111.1 \pm 10.0$	$-53.3 \pm 4.1$	a
	-76.4	-92.1	-48.9	b
$C_2H_5OH \cdots FHF^- + H_2O \rightleftharpoons (C_2H_5OH)_2 \cdots FHF^-$	$-56.5 \pm 2.0$	$-86.8 \pm 10.0$	$-30.6 \pm 4.1$	a
	-62.6	-111.3	-29.4	b

<sup>†</sup> –  $\Delta G_T^\circ = \Delta H_{rxn}^\circ - T\Delta S_{rxn}^\circ$

a – HPMS

b – MP2(full)/6-311++G(d,p)//B3LYP/6-311++G(d,p)

in Gibbs free energies at 298K were determined (*via* Eq. 1.9) to be  $-46.4 \pm 4.1 \text{ kJ}\cdot\text{mol}^{-1}$  and  $-42.8 \text{ kJ}\cdot\text{mol}^{-1}$ , respectively. Good agreement exists between theory and experiment for the thermochemical data obtained. The reported  $\Delta H_{rxn}^\circ$  values determined in this study are consistent with the binding energy of  $62.3 \text{ kJ}\cdot\text{mol}^{-1}$  reported by Li, *et al.*<sup>80</sup> with any discrepancy between values being explained by differences in calculation methods employed.

The optimized geometry, along with related structural properties for the most favorable species of  $\text{H}_2\text{O}\cdots\text{FHF}^-$ , is shown as structure **3.3I** and is consistent with the structure reported by Li, *et al.*<sup>80</sup> Pertinent bond lengths and angles associated with the various calculated mono-solvated structures, among others, are reported in Table 3-2. While the total F-F bond distance of  $2.321 \text{ \AA}$  remains relatively unchanged compared to the unclustered anion (F-F bond distance is  $2.278 \text{ \AA}^{68}$  in  $\text{FHF}^-$ ), the addition of  $\text{H}_2\text{O}$  to  $\text{FHF}^-$  causes the proton in  $\text{FHF}^-$  to shift to a final position  $1.274 \text{ \AA}$  away from the site of solvent molecule attachment and causes a change in the FHF bond angle to  $179.2^\circ$ , ( $\angle\text{FHF} = 180.0^\circ$  in  $\text{FHF}^-$ ). The newly formed OHF bond between water and  $\text{FHF}^-$  possesses a bond angle of  $172.2^\circ$  and a total O-F bond distance of  $2.605 \text{ \AA}$ . Upon close inspection, these geometric details provide information regarding the relative strengths of these hydrogen bonds and are rationalized when simple acidity and basicity arguments are considered.

If  $\text{FHF}^-$  is envisioned to be constructed of a proton-accepting  $\text{F}^-$  and a proton-donating HF group, the strongest, shortest and most linear hydrogen bond will be formed when the gas-phase basicity of  $\text{F}^-$  and gas-phase acidity of HF are strongest. Unsolvated  $\text{FHF}^-$  has been shown to be perfectly symmetric, and due to the indistinguishability of the fluorines, it is not possible to immediately assign the title of proton-accepting or proton-donating to either

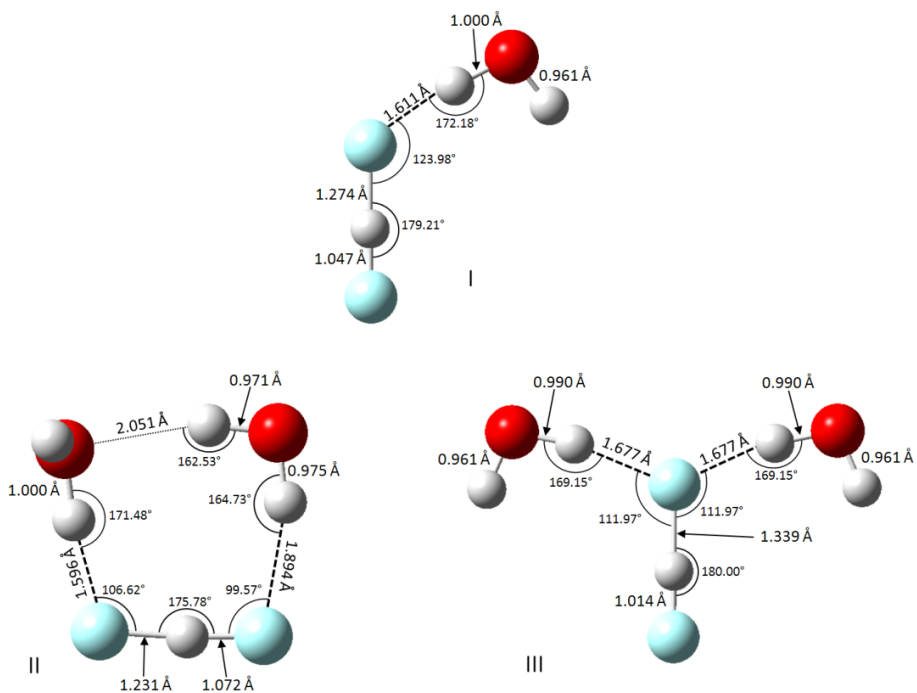


**Figure 3.3:** Structures and geometric properties of FHF $\cdots$ (H<sub>2</sub>O)<sub>n</sub> clusters, n = 1 and 2.

**Table 3-2: Summary of Important Geometric Properties of FHF<sup>-</sup> and Several Solvated FHF<sup>-</sup> Clusters.**

Cluster(Figure)	F-F (Å)	H-F (Å)	∠FHF (°)	F-O (Å)	F-H (Å)	∠FHO	source
FHF <sup>-</sup>	2.278	-	-	-	-	-	a
	2.294	1.147	180.0	-	-	-	b
H <sub>2</sub> O···FHF <sup>-</sup> (3.3I)	2.321	1.274	179.21	2.605	1.611	172.18	c
	2.321	1.274	179.2	2.605	1.611	172.2	b
(H <sub>2</sub> O) <sub>2</sub> ···FHF <sup>-</sup> (3.3II)	2.301	1.231	175.78	2.846, 2.589	1.894, 1.596	164.73, 171.48	c
	2.301	1.226	177	2.824, 2.579	1.868, 1.579	166, 176	b
(H <sub>2</sub> O) <sub>2</sub> ···FHF <sup>-</sup> (3.3III)	2.353	1.339	180.00	2.656	1.677	169.15	c
CH <sub>3</sub> OH···FHF <sup>-</sup> (3.4I)	2.330	1.293	179.65	2.570	1.573	173.54	c
(CH <sub>3</sub> OH) <sub>2</sub> ···FHF <sup>-</sup> (3.4II)	2.368	1.364	180.00	2.633	1.651	171.62	c
(CH <sub>3</sub> OH) <sub>2</sub> ···FHF <sup>-</sup> (3.4III)	2.283	1.142*	179.73	2.647*	1.666*	173.09*	c
C <sub>2</sub> H <sub>5</sub> OH···FHF <sup>-</sup> (3.5I)	2.322	1.278	178.42	2.587	1.593	172.86	c
	2.305	1.268	-	2.345	1.542	173.6	d
C <sub>2</sub> H <sub>5</sub> OH···FHF <sup>-</sup> (3.5II)	2.332	1.299	179.36	2.575	1.584	170.44	c
(C <sub>2</sub> H <sub>5</sub> OH) <sub>2</sub> ···FHF <sup>-</sup> (3.5III)	2.370	1.367	180.00	2.642	1.661	170.90	c
(C <sub>2</sub> H <sub>5</sub> OH) <sub>2</sub> ···FHF <sup>-</sup> (3.5IV)	2.280	1.140	180.00	2.673	1.693*	172.23*	c

a – ref<sup>68</sup>      b – ref<sup>80</sup>      c - MP2(full)/6-311++G(d,p)//B3LYP/6-311++G(d,p)

d – ref<sup>78</sup>

\* – average value

moiety in  $\text{FHF}^-$ . However, upon addition of the first solvent molecule (in this case water) the two fluorines in  $\text{FHF}^-$  become distinguishable. The fluorine involved in the newly formed OHF hydrogen bond can be identified as the proton-accepting site in  $\text{FHF}^-$ , since this new bond will attract electron density towards the site of attachment on  $\text{FHF}^-$ , giving it properties more similar to  $\text{F}^-$  than HF. The formation of the OHF hydrogen bond weakens the basicity of the  $\text{F}^-$  moiety, causing the observed lengthening of the F-F distance when unclustered  $\text{FHF}^-$  is compared to structure **3.3I**. Should the basicity of this proton-accepting fluorine weaken even further, a further increase in the FHF bond length would be observed. This is exactly what is observed upon the addition of a second water molecule, as discussed below. Since the gas phase acidity of HF ( $\Delta_{acid}G^\circ = 1529.3 \text{ kJ}\cdot\text{mol}^{-1}$ )<sup>81</sup> is stronger than that of water ( $\Delta_{acid}G^\circ = 1605.4 \text{ kJ}\cdot\text{mol}^{-1}$ )<sup>82</sup>, the FHF hydrogen bond is expected to be stronger than the OHF hydrogen bond. This is supported by the fact that the total O-F distance observed in **3.3I** is larger than the F-F distance, and the OHF bond angle of  $172.18^\circ$  is less linear than the FHF bond angle of  $179.21^\circ$ .

For the addition of a second water molecule onto mono-solvated  $\text{FHF}^-$ ,  $\Delta H_{exp}^\circ$  and  $\Delta S_{exp}^\circ$  were measured to be  $-60.7 \pm 2.0 \text{ kJ}\cdot\text{mol}^{-1}$  and  $-95.0 \pm 10.0 \text{ J}\cdot\text{K}^{-1}\cdot\text{mol}^{-1}$ , respectively, and  $\Delta G_{exp,298}^\circ$  was determined to be  $-32.4 \pm 4.1 \text{ kJ}\cdot\text{mol}^{-1}$ . These values are as expected, noting the decrease in both exothermicity and exergonicity for the addition of the subsequent water molecule. From a computational standpoint, several isomers of doubly solvated  $\text{FHF}^-$ , each possessing similar enthalpies of formation, can be obtained. This has been demonstrated by Li, *et al.*, in their presentation of three such structures.<sup>79</sup> Structure 3.3II reports the most enthalpically favorable structure for the di-hydrated  $\text{FHF}^-$  cluster and is

consistent with the most energetically stable structure reported by Li, *et al.*, while **3.3III** reports a slightly less enthalpically favorable isomer of this cluster. Rotamers of these two structures can be obtained *via* rotations of any combination of water molecules about the axis defined by the H-F bond between H<sub>2</sub>O and FHF<sup>-</sup>. A detailed discussion of such isomers will not be given here, as some of their energetic properties have been investigated previously<sup>79</sup> and were determined to be very similar (within 0.5 kJ·mol<sup>-1</sup>) to the most stable rotamers reported in Figure 3.3. When left unaccounted for, the presence of these rotamers leads to an increase in the measured value of  $\Delta S_{exp}^\circ$ , as discussed in Section 2.1. This is demonstrated upon comparison of entropy changes reported in Table 3-1 for the addition of the first and second water molecules, noting the more positive value of  $\Delta S_{exp}^\circ$  for the more isomerically rich di-hydrated cluster. Measured and calculated thermodynamic properties for the formation of important clusters of dihydrated FHF<sup>-</sup> are compared in Table 3-3. It is interesting to note that when entropic arguments are considered and  $\Delta G_{calc,298}^\circ$  values are compared, structure **3.3III** clearly emerges as the most thermodynamically favorable isomer. A comparison of the calculated thermodynamic properties of **3.3III** to the measured thermochemical fingerprint obtained from HPMS further exemplifies this point. Such a comparison provides evidence that the thermodynamically favored isomer is the predominant one found within the high pressure ion source, and that the second water molecule will exhibit a tendency to attach to the mono-solvated FHF<sup>-</sup> in the manner shown in **3.3III**. The excellent linearity of the associated van't Hoff plot (Figure 3.2) only provides further support of this fact, demonstrating the ability of high pressure mass spectrometry to distinguish between isomers, based on their thermochemical properties.

**Table 3-3: Calculated and Measured Thermochemical Properties of Various Isomers of  $(ROH)_n \cdots FHF^-$ .**

Structure: <sup>a</sup>	3.3II <sup>b</sup>	3.3III <sup>b</sup>	HPMS <sup>c</sup>	3.4II <sup>b</sup>	3.4III <sup>b</sup>	HPMS <sup>c</sup>	3.5I <sup>b</sup>	3.5II <sup>b</sup>	HPMS <sup>c</sup>	3.5III <sup>b</sup>	3.5IV <sup>b</sup>	HPMS <sup>c</sup>
$\Delta H_{rxn}^\circ$ (kJ·mol <sup>-1</sup> )	-59.9	-58.9	-60.7 ± 2.0	-61.2	-56.6	-64.0 ± 2.0	-77.6	-76.4	-86.4 ± 2.0	-62.6	-60.5	-56.5 ± 2.0
$\Delta S_{rxn}^\circ$ (J·K <sup>-1</sup> ·mol <sup>-1</sup> )	-142.2	-96.2	-95.0 ± 10.0	-106.3	-97.2	-104.9 ± 10.0	-101.4	-92.1	-111.1 ± 10.0	-111.3	-129.5	-86.8 ± 10.0
$\Delta G_{298}^\circ$ <sup>d</sup> (kJ·mol <sup>-1</sup> )	-17.5	-30.2	-32.4 ± 4.1	-29.6	-27.6	-32.7 ± 4.1	-47.4	-48.9	-53.3 ± 4.1	-29.4	-21.9	-30.6 ± 4.1

a – number refers to Figure number

b – MP2(full)/6-311++G(d,p)//B3LYP/6-311++G(d,p)

c – exp. data for system reported in columns to left

d –  $\Delta G_T^\circ = \Delta H_{rxn}^\circ - T\Delta S_{rxn}^\circ$

A detailed examination of the geometry of structure **3.3III** provides more insight into the effect of solvation on  $\text{FHF}^-$ . Observations made of the geometric changes of the monohydrated cluster become even more evident in the case of the di-hydrated anion. As seen in **3III**, the proton in  $\text{FHF}^-$  shifts to a final position 1.339 Å away from the point of solvation, 0.067 Å further than for the singly solvated case, making the total F-F distance 2.353 Å. Again this is expected since the basicity of the  $\text{F}^-$  moiety is weakened even further than in the mono-hydrated case, and thus a weaker FHF bond is observed. It is interesting to note that attachment of a second solvent molecule to the unclustered end of mono-solvated  $\text{FHF}^-$ , as in the case of the ergonomically less favorable **3.3II**, the acid strength of the proton donating fluorine in  $\text{FHF}^-$  increases and when compared to the mono-hydrated case, a strengthening of the FHF bond, indicated by a shorter F-F distance of 2.303 Å, is observed. In structure **3.3III** both OHF bond angles are found to be 169.15° and the total O-F distances are 2.656 Å, indicating a weaker interaction than observed in the n=1 cluster. An interesting result of the addition of a second solvent molecule was the restoration of symmetry to the atomic orbitals on the proton in  $\text{FHF}^-$ , indicated by the return of the FHF bond angle to 180° (as is the case found for unclustered  $\text{FHF}^-$ ). This is in contrast to the nonlinear FHF bonds of structures **3I** and **3II**, for which the bond angles are 179.21° and 175.78°, respectively.

### 3.3.2 Step-wise Solvation of $\text{FHF}^-$ by $\text{CH}_3\text{OH}$

The van't Hoff plots for the n = 1 and 2 cases of methanol clustering onto  $\text{FHF}^-$  are shown in Figure 3.2. From these plots,  $\Delta H_{exp}^\circ$  for first and second addition of methanol were measured to be  $-82.4 \pm 2.0 \text{ kJ}\cdot\text{mol}^{-1}$  and  $-64.0 \pm 2.0 \text{ kJ}\cdot\text{mol}^{-1}$ , while  $\Delta S_{exp}^\circ$  for these reactions

were determined to be  $-110.8 \pm 10.0 \text{ J}\cdot\text{K}^{-1}\cdot\text{mol}^{-1}$  and  $-104.9 \pm 10.0 \text{ J}\cdot\text{K}^{-1}\cdot\text{mol}^{-1}$ , respectively. Eq. 1.9 was employed to determine  $\Delta G_{exp,298}^\circ$  to be  $-49.3 \pm 4.1 \text{ kJ}\cdot\text{mol}^{-1}$  and  $-32.7 \pm 4.1 \text{ kJ}\cdot\text{mol}^{-1}$ . Calculations performed on this system determined  $\Delta H_{calc}^\circ$ ,  $\Delta S_{calc}^\circ$  and  $\Delta G_{calc,298}^\circ$  for the mono-solvated case to be  $-73.2 \text{ kJ}\cdot\text{mol}^{-1}$ ,  $-84.5 \text{ J}\cdot\text{K}^{-1}\cdot\text{mol}^{-1}$  and  $-48.0 \text{ kJ}\cdot\text{mol}^{-1}$ . These values can be found in Table 3-1, noting a similar level of agreement between measurements and calculations as that observed in the water clusters. In the case of the di-solvated cluster,  $\Delta H_{calc}^\circ$ ,  $\Delta S_{calc}^\circ$  and  $\Delta G_{calc,298}^\circ$  were determined to be  $-61.3 \text{ kJ}\cdot\text{mol}^{-1}$ ,  $-106.3 \text{ J}\cdot\text{K}^{-1}\cdot\text{mol}^{-1}$  and  $-29.6 \text{ kJ}\cdot\text{mol}^{-1}$  and are in good agreement with experimental values. This increase in agreement between experimental and calculated data over the mono-solvated case is, again, similar to that observed in the water clusters.

Reported in Figure 3.4 are the lowest energy (and thermodynamically favored) structures calculated for methanol solvated  $\text{FHF}^-$  clusters. Many of the observations made on these clusters are analogous to those made for the water clusters reported in Figure 3.3. Rotamers of **3.4II** can be obtained, all within  $1 \text{ kJ}\cdot\text{mol}^{-1}$  of the reported lowest energy structures, and can be envisioned as rotations of the methanol about the HF axis of the various OHF hydrogen bonds. Other isomers of the di-solvated cluster have been investigated, where attachment of the second methanol takes place on the opposite end of the  $\text{FHF}^-$ , as seen in structure **3.4III**. A comparison of the calculated thermochemical properties for structures **3.4II** and **III** is given in Table 3-3. According to calculations, **3.4III** is  $4.70 \text{ kJ}\cdot\text{mol}^{-1}$  less enthalpically favourable and  $1.98 \text{ kJ}\cdot\text{mol}^{-1}$  less ergonomically favourable than structure **3.4II**. This small difference leads to the prediction that both of these isomers, as

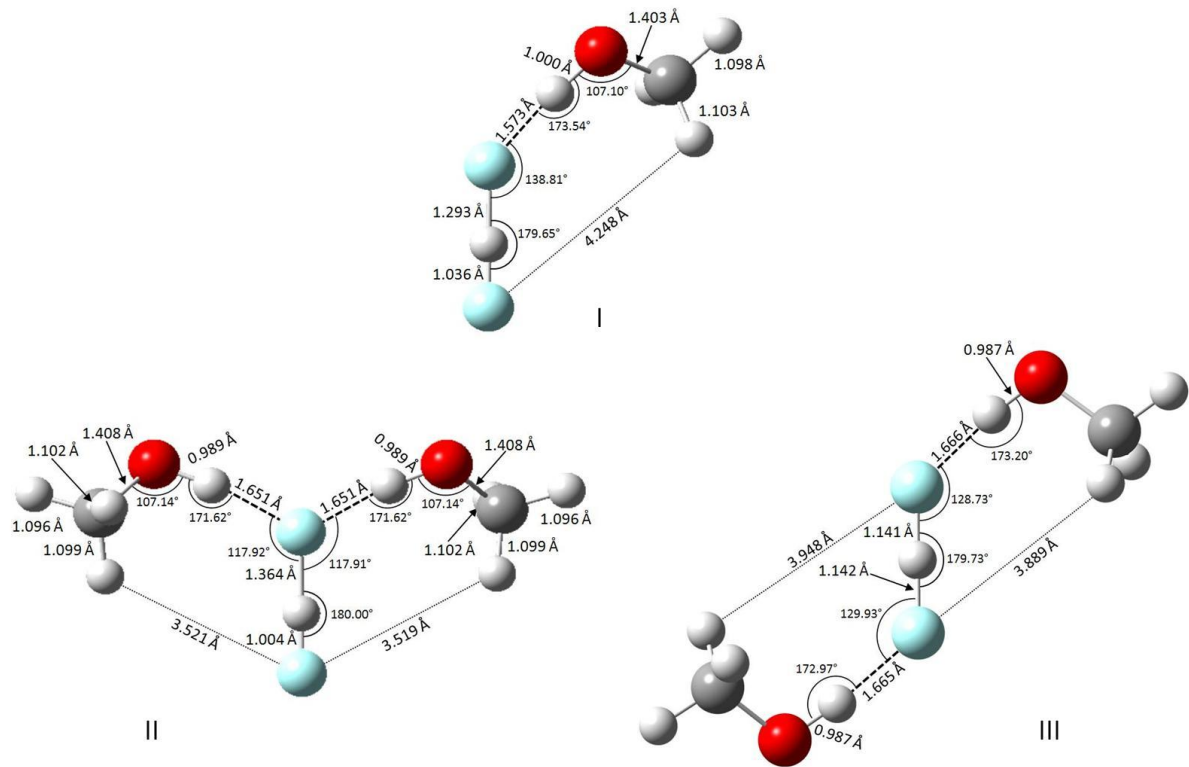


**Figure 3.4: Structures and geometric properties of FHF<sup>-</sup>···(CH<sub>3</sub>OH)<sub>n</sub> clusters, n = 1 and 2.**

well as any others of comparable energetics, will contribute significantly to the overall thermochemistry observed within the ion source.

Pertinent bond lengths and angles for structures **3.4I-III** are tabulated in Table 3-2. The relationship between bond length and bond strength is demonstrated in both **3.4I** and **II**, as the proton in FHF<sup>-</sup> is observed to shift to a final position 1.293 Å and 1.364 Å away from the site of solvation. Total F-F bond distances for the mono- and di-solvated clusters are calculated to be 2.329 Å and 2.368 Å, respectively. The FHF bond angle goes through an evolution similar to that observed for the water clusters. Specifically, addition of the first solvent molecule causes the once linear FHF<sup>-</sup> to bend slightly to 179.65°, while addition of the second restores the angle to 180.00°. The newly formed OHF hydrogen bond of the mono-solvated cluster is characterized by an H-F distance of 1.573 Å, a total O-F distance of 2.573 Å and  $\angle OHF = 173.54^\circ$ . According to calculation, the addition of a second methanol, as shown in structure **3.4II** alters the geometry of the first OHF bond, resulting in two identical OHF bonds with an H-F distance of 1.651 Å, a total O-F distance of 2.640 Å and  $\angle OHF = 171.62^\circ$ . In contrast to structures **3.3I-III**, **3.4I** and **3.4II**, the observed F-F bond distance found in **3.4III** (2.283 Å) is only 0.005 Å longer than the F-F distance in unsolvated FHF<sup>-</sup>.

### 3.3.3 Step-wise Solvation of FHF<sup>-</sup> by C<sub>2</sub>H<sub>5</sub>OH

The van't Hoff plots for the clustering of one and two ethanol molecules to FHF<sup>-</sup> are shown in Figure 3.2, with measured and calculated values for the associated processes reported in Table 3-1. HPMS determined values of  $\Delta H_{exp}^\circ$  and  $\Delta S_{exp}^\circ$  for the addition of the

first ethanol molecule to  $\text{FHF}^-$  are  $-86.4 \pm 2.0 \text{ kJ}\cdot\text{mol}^{-1}$  and  $-111.1 \pm 10.0 \text{ J}\cdot\text{K}^{-1}\cdot\text{mol}^{-1}$ , respectively, while calculations determine  $\Delta H_{calc}^\circ$  to be  $-76.4 \text{ kJ}\cdot\text{mol}^{-1}$  and  $\Delta S_{calc}^\circ$  to be  $-92.1 \text{ J}\cdot\text{K}^{-1}\cdot\text{mol}^{-1}$ . Again, Eq. 1.9 was employed and  $\Delta G_{rxn,298}^\circ$  values from HPMS and calculation were determined to be  $-53.3 \pm 4.1 \text{ kJ}\cdot\text{mol}^{-1}$  and  $-48.9 \text{ kJ}\cdot\text{mol}^{-1}$ , respectively. For the addition of the second molecule of ethanol, HPMS experiments determined  $\Delta H_{exp}^\circ$  and  $\Delta S_{exp}^\circ$  to be  $-56.5 \pm 2.0 \text{ kJ}\cdot\text{mol}^{-1}$  and  $-86.8 \pm 10.0 \text{ J}\cdot\text{K}^{-1}\cdot\text{mol}^{-1}$ , respectively, while calculations determined them to be  $-62.6 \text{ kJ}\cdot\text{mol}^{-1}$  and  $-111.3 \text{ J}\cdot\text{K}^{-1}\cdot\text{mol}^{-1}$ .  $\Delta G_{298}^\circ$  values obtained from HPMS and calculations were found to be  $-30.6 \pm 4.1 \text{ kJ}\cdot\text{mol}^{-1}$  and  $-29.4 \text{ kJ}\cdot\text{mol}^{-1}$ , respectively. The level of agreement between theory and experiment was found to be of the same high degree of accuracy as noted in the cases of water and methanol.

As in the cases of water and methanol solvation, many thermodynamically accessible isomers exist for the cluster ions involved in the solvation of  $\text{FHF}^-$  with  $\text{C}_2\text{H}_5\text{OH}$ . Two such isomers have been previously discussed in detail by Hamilton, et al,<sup>78</sup> while structure **3.5I** shows the most enthalpically favorable structure found. A third, previously unreported isomer, **3.5II**, is also reported and was found to be the most ergonomically favorable structure of  $\text{C}_2\text{H}_5\text{OH}\cdots\text{FHF}^-$ . While structure **3.5II** is slightly less enthalpically favorable, an increase in the entropic favorability gives this ion a small ergonomic advantage of  $1.5 \text{ kJ}\cdot\text{mol}^{-1}$  over **3.5I**. The thermochemical details of **3.5I** and **3.5II** are reported in Table 3-3. This difference is, however, small and thus a statistical distribution of these two isomers, as well all other accessible isomers, are expected to be found within the high pressure ion source. Evidence of this can be seen in Table 3-1 as the measured value of  $\Delta S_{rxn}^\circ$  is observed to be more positive than the calculated value by nearly  $20 \text{ J}\cdot\text{K}^{-1}\cdot\text{mol}^{-1}$ , as predicted by Eq. 2.9.

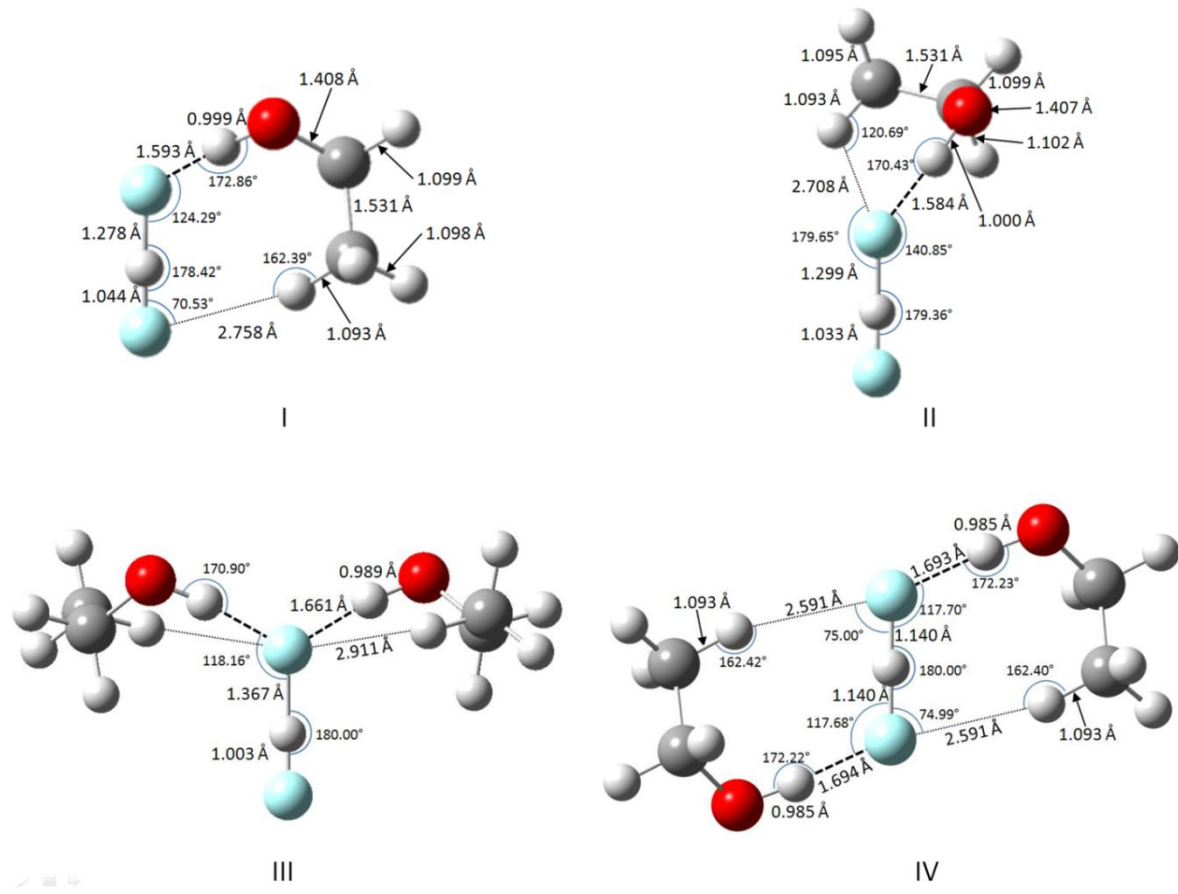


**Figure 3.5: Structures and geometric properties of FHF<sup>-</sup>···(C<sub>2</sub>H<sub>5</sub>OH)<sub>n</sub> clusters, n = 1 and 2.**

Inspection of the geometries of these clusters (Table 3-2) continues to demonstrate the effects of solvation on the strong FHF hydrogen bond. Structure **3.5I** reveals a smaller proton shift in  $\text{FHF}^-$ , compared to the methanol solvated counterpart, with the proton sitting a final distance of 1.278 Å away from the fluorine involved in the new OHF bond and  $\angle\text{FHF} = 178.42^\circ$ . This decrease in proton shift from the centre can be rationalized by the presence of an additional CHF hydrogen bond between the solvent molecule and  $\text{FHF}^-$ , taking place on the fluorine not involved with the strong OHF bond. As stated before, if  $\text{FHF}^-$  is envisioned to be comprised of an HF proton-donating group and an  $\text{F}^-$  proton-accepting group, this second interaction acts to increase the acid strength of the HF donating group, resulting in a stronger FHF hydrogen bond than that found in the methanol solvated case. Inspection of **3.5II** demonstrates the effect of forming the second interaction to the  $\text{F}^-$  proton-accepting group. This causes the basicity of this moiety to weaken, and hence, a longer HF distance of 1.299 Å is observed. It is interesting to see that the FHF bond in **3.5II** ( $\angle\text{FHF}=179.36^\circ$ ) retains more of its linearity than does **3.5I** upon solvation. The OHF bonds of both **3.5I** and **3.5II** can be characterized as having O-F distances of 2.592 Å and 2.584 Å, respectively, H-F distances of 1.593 and 1.584 and a bond angles of 172.86° and 170.43°.

The addition of a second molecule of ethanol to mono-solvated  $\text{FHF}^-$  can be envisioned to take place in two main ways: 1) through the formation of a second strong OHF hydrogen bond to the same fluorine as the first strong OHF bond, or 2) through the formation of the second strong OHF bond at the opposite fluorine in FHF compared to the site of attachment of the first ethanol. Structures **3.5III** and **3.5IV** depict the two lowest energy isomers of the aforementioned types for  $\text{FHF}^-$  di-solvated with ethanol, and associated

thermochemical data are found in Table 3-3. Many rotamers of both **3.5III** and **3.5IV** exist but they will not be discussed here. The observation of an even larger discrepancy between measured and calculated values of  $\Delta S_{rxn}^\circ$ , reported in Table 3-1 indicates the presence of an even larger number of isomers within the ion source compared to the di-solvated water or methanol clusters. As in the cases of two water and methanol molecules onto  $\text{FHF}^-$ , the site of attachment of a second ethanol is most ergonomically favorable on the same fluorine possessing the first strong OHF bond, in this case by  $7.5 \text{ kJ}\cdot\text{mol}^{-1}$ .

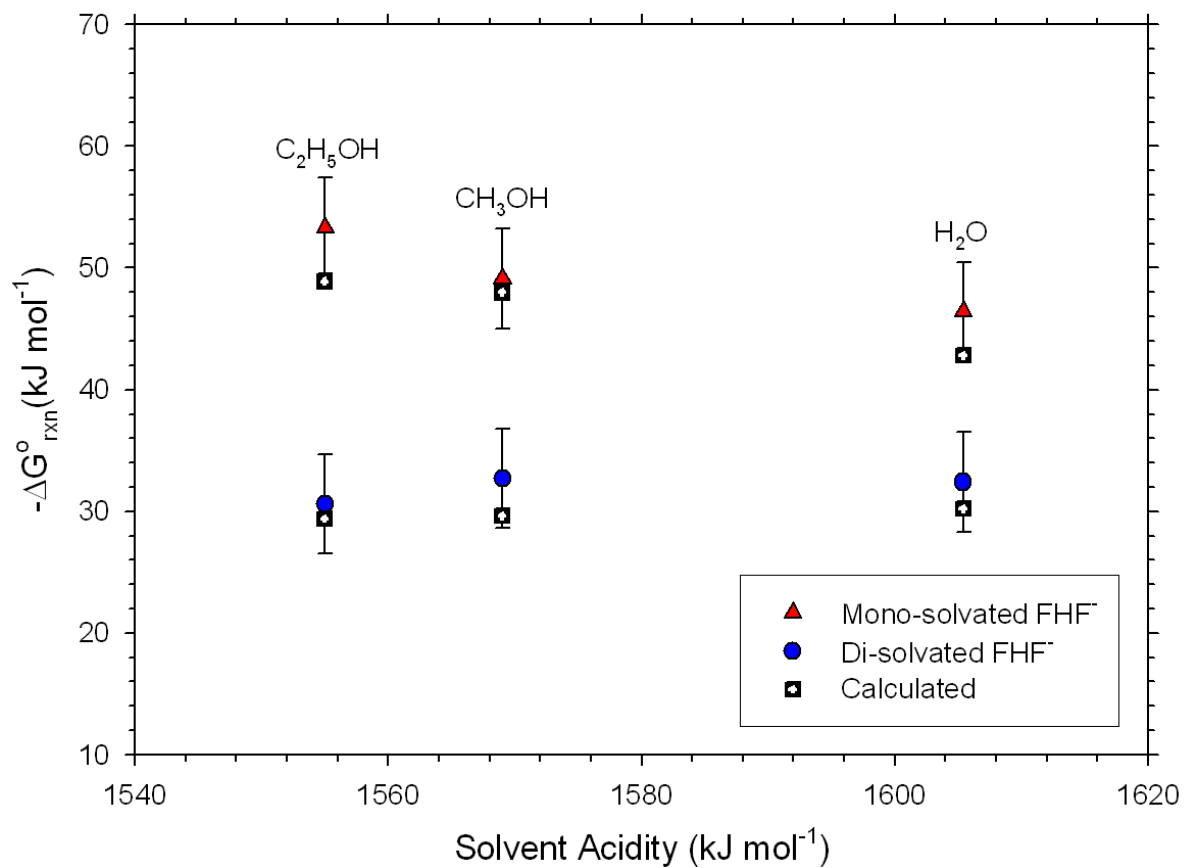
Examination of **3.5III** once again shows the di-fluorinated proton shift away from the site of solvation to a final equilibrium distance of  $1.367 \text{ \AA}$ . The calculated FHF bond angle of  $180.00^\circ$  and symmetric placement of the two solvent molecules for this ergonomically favourable structure give rise to the familiar  $C_2$  point group arrangement that was observed in the di-solvated water and methanol systems. Both OHF bonds were determined to have the proton resting at an equilibrium distance of  $1.661 \text{ \AA}$  away from the fluorine with  $\angle\text{OHF} = 170.90^\circ$ . Structure **3.5IV**, while  $7.5 \text{ kJ}\cdot\text{mol}^{-1}$  less favorable ergonomically and not considered to be a major constituent within the high pressure ion source, possesses some interesting properties that are worth mentioning. The effect of the highly symmetric double solvation on the FHF bond can be seen in both its linearity and its bond length. The total F-F distance,  $2.280 \text{ \AA}$ , in this isomer is again found to be quite short,  $0.002 \text{ \AA}$  greater than that in bare  $\text{FHF}^-$  and  $0.003 \text{ \AA}$  shorter than **3.4III**.

### 3.3.4 Summary of Thermochemical and Geometric Trends

To better demonstrate the relationship between hydrogen bond strength and the acidity and basicity of all bonding groups involved, several comparative graphs are presented. Figure 3.6 is a plot of  $\Delta G_{calc,298}^\circ$  for the addition of a solvent molecule (i.e. the formation of an OHF hydrogen bond) as a function of the gas-phase acidity of the solvent molecule. Both experimentally determined and calculated values for the stepwise solvation of  $\text{FHF}^-$  with water, methanol and ethanol are shown, demonstrating the excellent agreement between theory and experiment.

When considering the mono-solvation of  $\text{FHF}^-$ , an expected increase in the hydrogen bond strength is observed as the acid strength of the solvent molecule increases. It can also be noted that this initial solvation of  $\text{FHF}^-$  weakens the basicity of the proton-accepting fluorine, resulting in all subsequent hydrogen bonds formed (the di-solvated cases) to that fluorine being less exergonic.

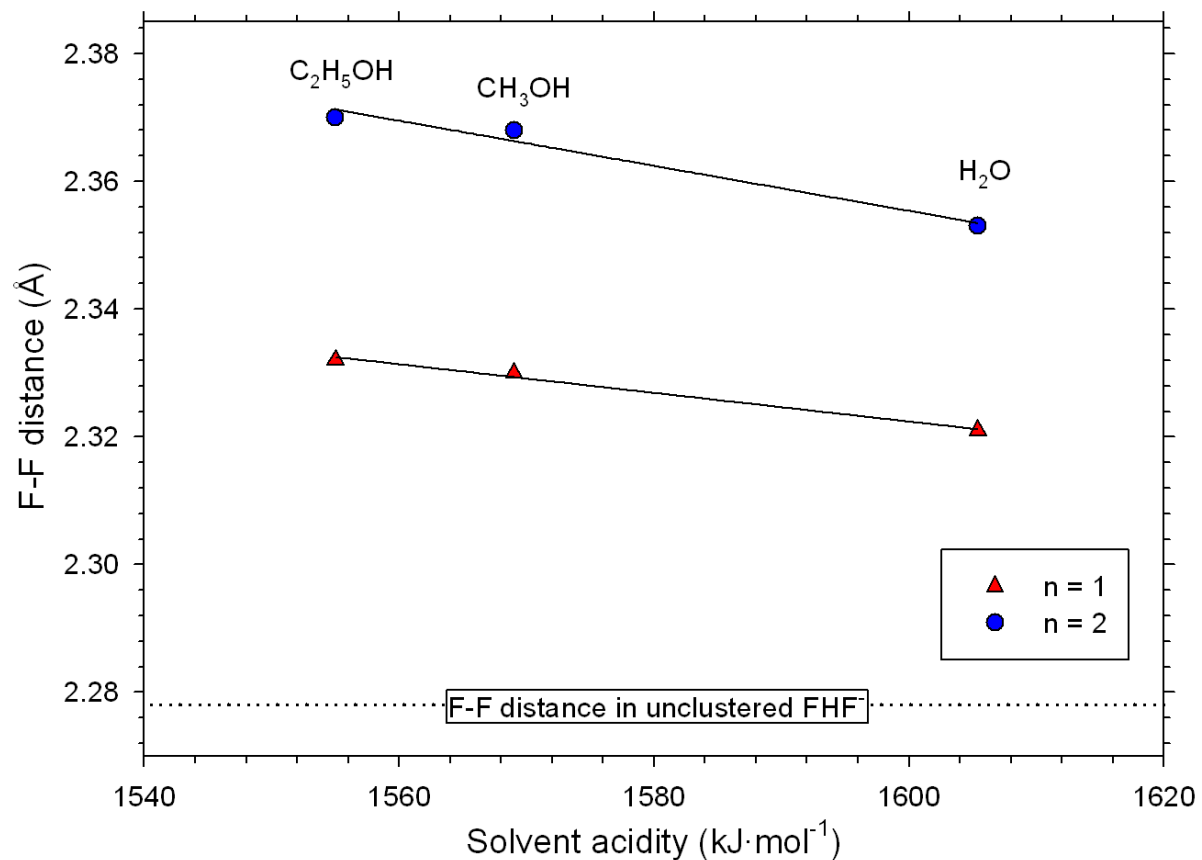
When considering the di-solvated clusters, it is interesting to note that an increase in the experimentally determined exergonicity is observed from water to methanol, while a decrease in exergonicity is observed when the acidity is further increased to the case of ethanol. This break in the direct relationship between bond strength and solvent acid strength is a manifestation of secondary interactions between the terminal methyl group of ethanol and the fluorine of  $\text{FHF}^-$ . The presence of this secondary interaction in the mono-solvated cluster weakens the basicity of the proton accepting fluorine, demonstrating that even though the acid strength of the solvent molecule may increase, the overall strength of a second OHF hydrogen bond may be lower than expected.



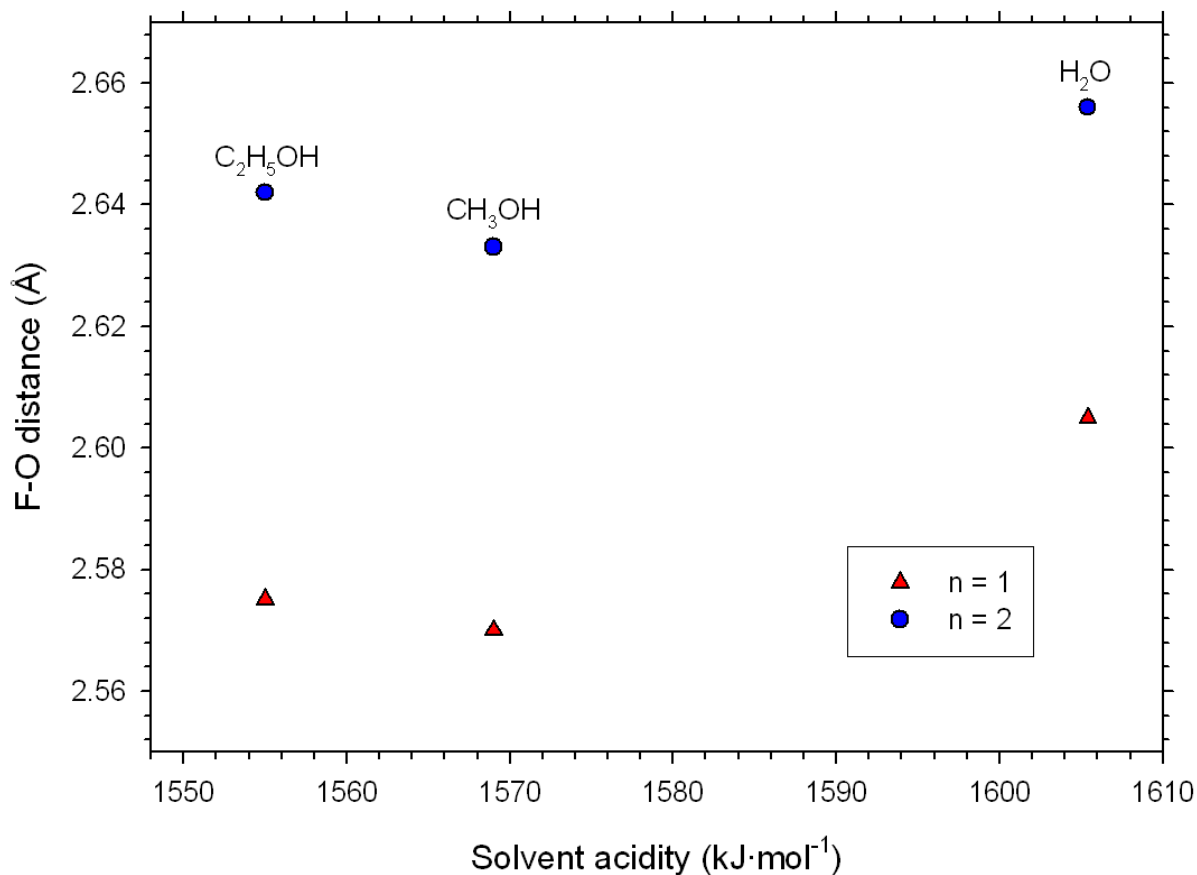
**Figure 3.6: Measured and calculated ergonicity of stepwise formation reactions for  $(ROH)_n \cdots FHF^-$  as a function of the gas phase acidity of ROH ( $n = 1$  and  $2$ ;  $R = H, CH_3, C_2H_5$ ). Gas-phase acidities for  $H_2O$ ,  $CH_3OH$  and  $C_2H_5OH$  were obtained from ref<sup>82</sup>, ref<sup>57</sup> and ref<sup>57</sup>, respectively.**

Figure 3.7 is a plot of the total F-F bond distance in  $\text{FHF}^-$  as a function of the gas phase acidity of the solvent molecule. Compared to unclustered  $\text{FHF}^-$ , an increase in F-F bond length is observed upon mono-solvation. In both the mono- and di-solvated systems, a linear increase in the F-F distance as a function of the acid strength of the solvent exists and can be rationalized as follows. Since the basicity of the fluorine decreases as a result of the newly formed OHF hydrogen bond, a lengthening of all other bonds with which it is involved (the strong hydrogen bond in  $\text{FHF}^-$ ) is expected. Likewise, as acid strength of the solvent increases, the F-F bond distance continues to increase. If a second hydrogen bond is formed to the fluorine (moving vertically within Figure 3.7, from the mono-solvated case to the di-solvated case), a further weakening in fluorine basicity occurs, and hence, a large increase in the F-F bond distance is observed. As acid strength of the solvent in the di-solvated system increases, so will the F-F distance.

The F-O bond distance found in the most ergonomically favored species is plotted against the gas phase acidity of the solvent in Figure 3.8. As the acid strength of the solvent increases, a stronger hydrogen bond (shorter F-O distance) is expected since the proton donating ability of the hydroxyl will increase. In both the mono- and di-solvated cases, this shortening of the F-O distance can be observed when water clusters are compared to those of methanol, however a slight lengthening of the F-O distance is observed when methanol is compared to ethanol. In order to discern the trends observed here, the effect of secondary interactions must once again be considered. Upon inspection of the equilibrium structure of the ethanol clusters, it can be seen that a secondary interaction between the terminal methyl of ethanol and the same fluorine involved in the strong OHF hydrogen bond exists. This



**Figure 3.7:** Calculated F-F bond distances in  $(ROH)_n \cdots FHF^-$  clusters ( $n = 1$  and  $2$ ;  $R = H, CH_3, C_2H_5$ ) plotted against the gas phase acidity of ROH. Note, only F-F distances for the most ergonomically favorable species are plotted. Gas-phase acidities for  $H_2O$ ,  $CH_3OH$  and  $C_2H_5OH$  were obtained from ref <sup>82</sup>, ref <sup>57</sup> and ref <sup>57</sup>, respectively.



**Figure 3.8:** Calculated F-O bond distances in  $(ROH)_n \cdots FHF^-$  clusters ( $n = 1$  and  $2$ ;  $R = H, CH_3, C_2H_5$ ) plotted against the gas phase acidity of ROH. Note, only F-O distances for the most ergonomically favorable species are plotted. In the case of the doubly solvated clusters, the  $C_2$  symmetry of these clusters reduces the discussion of two separate OHF hydrogen bonds to that of one identical pair (*via* an  $180^\circ$  rotation) of OHF bonds. Gas-phase acidities for  $H_2O$ ,  $CH_3OH$  and  $C_2H_5OH$  were obtained from ref <sup>82</sup>, ref <sup>57</sup> and ref <sup>57</sup>, respectively.

secondary interaction, also responsible for raising the exergonicity of the n=2 cluster of ethanol onto FHF<sup>-</sup> (Figure 3.7), decreases the basicity of the fluorine and hence results in a slightly longer than expected F-O distance.

### 3.4 Conclusions

An examination of the strong and very strong hydrogen bonds found in (ROH)<sub>n</sub>...FHF clusters (n = 1 and 2; R = H, CH<sub>3</sub>, C<sub>2</sub>H<sub>5</sub>) has been presented. Very good agreement has been observed between thermochemical values obtained from HPMS measurements and those predicted from MP2(full)/6-311++G(d,p)//B3LYP/6-311++G(d,p) calculations, with all calculated values of the ergonicity falling within the experimental error of  $\pm 4.1 \text{ kJ}\cdot\text{mol}^{-1}$ . Calculated structures were then examined and insight into the geometric bonding nature of these systems was obtained. In the case of water binding to FHF<sup>-</sup>, it was found that the large entropic advantage of structure **3.3III** over **3.3II** was significant enough as to make **3.3III** the predominant species found within the ion source. In the case of methanol solvation, no evidence of secondary interaction of the methyl group with any other moiety could be found. The structural details revealed from the ethanol-solvated clusters indicate that if secondary interactions between the terminal methyl group and FHF<sup>-</sup> are present, then the consequences of such interactions can be seen in both the strength and the length of the FHF and OHF bonds.

## Chapter 4

# Strong and Very Strong Hydrogen Bonding in Fluoro-amine – Fluoride Systems

### 4.1 Introduction

In the solid and liquid phases,  $\text{NF}_2\text{H}$  (difluoramine) has attracted considerable attention based on its highly unstable and explosive nature.<sup>83-85</sup> The extremely volatile nature of this compound makes it very dangerous to work with and significant safety precautions must be taken when dealing with it. In the gas-phase, difluoramine is much safer to handle and, as such, it has been possible for it to be characterized by IR, microwave and UV spectroscopy<sup>86-88</sup>, Figure 4.1. Despite considerable interest in the condensed phase of difluoramine as a potential explosive and fuel<sup>89</sup>, relatively few gas-phase investigations of clusters of difluoramine have been performed<sup>90,91</sup> as a source of insight into the true nature of the intermolecular interactions intrinsic to this molecule.

The presence of both the NH moiety and lone pairs of electrons on nitrogen and fluorine in difluoramine make it an appealing candidate for hydrogen bond formation. Yamdagni and Kebarle first demonstrated that hydrogen bond strength,  $D(\text{BH}\cdots\text{X}^-)$ , will increase both with the acidity of an acid, BH, and the basicity of an ionic base,  $\text{X}^-$ .<sup>22</sup> It has also previously been demonstrated that fluorination of an acid, BH, can lead to both an increase in the gas-phase acidity of BH and a stronger  $\text{BH}\cdots\text{X}^-$  hydrogen bond. This is demonstrated, for example, by the hydrogen bonding properties of ethanol and 1,1,1 trifluoroethanol. The substitution of fluorine in ethanol to form  $\text{CF}_3\text{CH}_2\text{OH}$  results in a

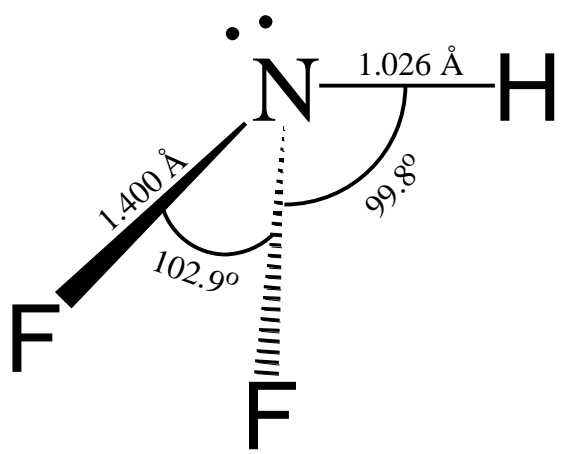


**Figure 4.1:** Structure of  $\text{NF}_2\text{H}$  as determined from microwave spectroscopy by Lide.<sup>87</sup>

decrease in the enthalpy of deprotonation from 1586.2 kJ·mol<sup>-1</sup><sup>92</sup> to 1513 kJ·mol<sup>-1</sup><sup>93</sup>, indicating a substantial increase in the gas-phase acid strength. When CH<sub>3</sub>CH<sub>2</sub>OH and CF<sub>3</sub>CH<sub>2</sub>OH are clustered with the anionic base F<sup>-</sup>, the measured OHF hydrogen bond strengths are -135.6 kJ·mol<sup>-1</sup><sup>94</sup> and -164 kJ·mol<sup>-1</sup><sup>59</sup>, respectively. The difference in values of ΔH<sub>rxn</sub><sup>o</sup> for the deprotonation of NF<sub>2</sub>H and NH<sub>3</sub> are even greater and reported in the literature as -1552 kJ·mol<sup>-1</sup><sup>95</sup> and -1563 kJ·mol<sup>-1</sup><sup>96</sup> for NF<sub>2</sub>H and -1687.8 kJ·mol<sup>-1</sup><sup>97</sup> for NH<sub>3</sub>. Based on these arguments, difluoramine would be expected to participate in stronger hydrogen bonds with F<sup>-</sup> than would NH<sub>3</sub> and is a very likely candidate to form very strong hydrogen bonds.

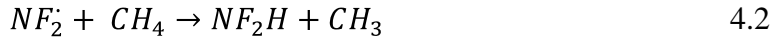
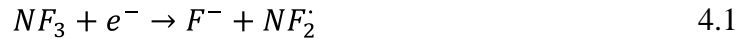
An investigation of difluoramine in hydrogen bonding environments from both experimental and computational perspectives was performed. Using high pressure mass spectrometry, thermochemical properties associated with difluoramine were measured. This technique allows for the creation of ions derived from potentially dangerous compounds *in situ*, greatly increasing the safety of the experiment. Also, computational investigations of difluoramine, as well as other clusters of interest, have been performed to help further develop the understanding of very strong hydrogen bonds which can form in amine-fluorine systems.

## 4.2 Experimental

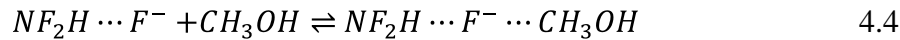
In a heated 5L reservoir, a known amount (between 2 and 40 μL) of CH<sub>3</sub>OH was injected into a mixture containing 9 torr NF<sub>3</sub> in 900 torr CH<sub>4</sub>. CH<sub>3</sub>OH (99.8% purity), NF<sub>3</sub>, and CH<sub>4</sub> (99.97% purity) were purchased from Sigma Aldrich, Ozark Mahoning, and Praxair,

respectively. Chemicals were used as supplied with no further purification performed. This mixture was introduced into the ion source at a constant total pressure and, using 2 keV electron pulses of 60  $\mu$ s duration with a repetition period of 60 ms, small, but reproducible ionic signals corresponding to  $\text{NF}_2\text{H}\cdots\text{F}^-$  and  $\text{NF}_2\text{H}\cdots\text{F}^-\cdots\text{CH}_3\text{OH}$  were observed.

There are several different possible explanations for the presence of the difluoramine containing species within the ion source. One possibility is that a small amount of  $\text{NF}_2\text{H}$  is present as a contaminant in the commercial sample of  $\text{NF}_3$ . Gaseous  $\text{NF}_2\text{H}$  is known to react with metal surfaces to decompose into HF and tetrafluorohydrazine<sup>84,85,98</sup> and it is possible that tetrafluorohydrazine itself may react subsequently with protic species to regenerate  $\text{NF}_2\text{H}$ . A second possibility is the direct synthesis of  $\text{NF}_2\text{H}$  within the ion source, initiated by ionization of the gas mixture. Slow secondary electrons or low energy electrons resulting from the thermalization of the 2 kV electrons entering the source, can undergo dissociative electron capture to  $\text{NF}_3$ , Eq. 4.1<sup>96</sup> and the resulting  $\text{NF}_2^\cdot$  species can then react with  $\text{CH}_4$  to generate  $\text{NF}_2\text{H}$ , Eq. 4.2.



Whatever the mechanism of formation, once  $\text{NF}_2\text{H}$  and  $\text{NF}_2\text{H}\cdots\text{F}^-$  are present in the ion source they may readily associate with fluoride and methanol respectively, leading to the formation of the fluoride bound dimer of difluoramine and methanol, Eq. 4.3 and Eq. 4.4.



All ions are generated in the electric field free ion source in the presence of a bath gas, in this case CH<sub>4</sub>, and, at the experimental pressures used, newly formed ions will have undergone approximately 10<sup>8</sup> collisions before diffusing out of the ion source. This ensures that all ions attain thermal equilibrium within the residence time in the ion source.

Using an EG&G Ortec multichannel scalar data acquisition system, 7000 accumulations of ion intensity as a function of time after ionization were summed for all ionic species in reaction (1). This large number of accumulations was necessary to improve the signal to noise ratio of the low intensity ion signals involved. Typical time-intensity and normalized time intensity plots can be found in Figure 4.2 and Figure 4.3, respectively. Normalization of the two resulting time-intensity profiles with respect to each other allowed for the identification of the presence of thermal equilibrium 0.5 ms after the end of the electron gun pulse as indicated by the parallel horizontal region in Figure 4.2.

By taking the ratio of product to reactant ion intensities during the period in which the two ions were in equilibrium (after 1.5 ms), and dividing by the partial pressure of the neutral

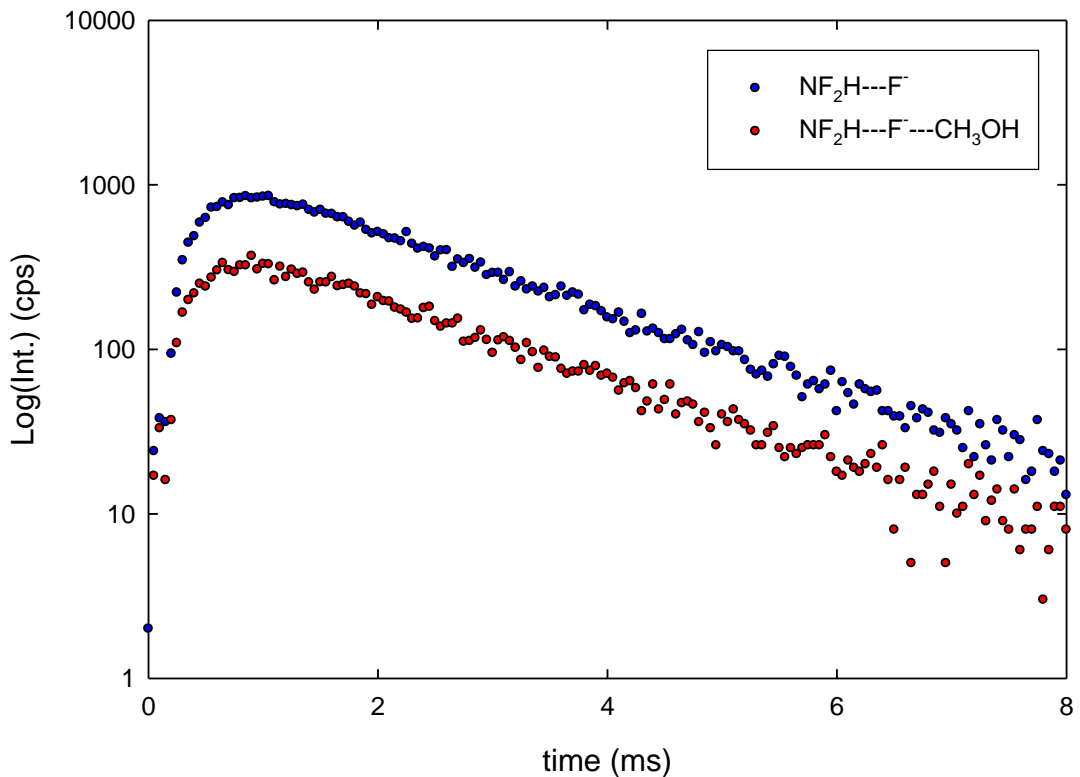


**Figure 4.2:** Time-intensity profiles for  $\text{NF}_2\text{H}\cdots\text{F}^-$  and  $\text{NF}_2\text{H}\cdots\text{F}^-\cdots\text{CH}_3\text{OH}$  at  $117^\circ\text{C}$  and  $P_{\text{CH}_3\text{OH}} = 7.45$  millitorr. Each profile is the result of the summation of ion intensity after 7000 electron gun pulses.

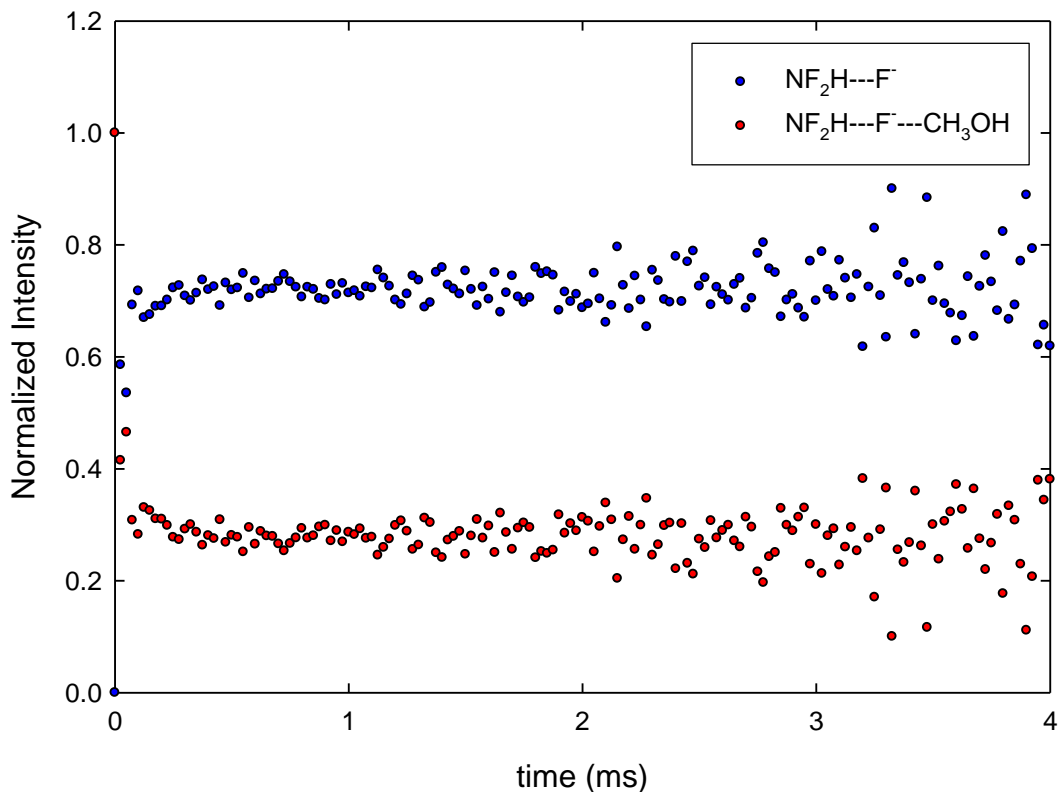


**Figure 4.3:** Normalized time-intensity profiles for  $\text{NF}_2\text{H}\cdots\text{F}^-$  and  $\text{NF}_2\text{H}\cdots\text{F}^-\cdots\text{CH}_3\text{OH}$ . Equilibrium is established 0.5 ms after ionization and lasts until 3 ms after ionization. The apparent divergence observed after 4 ms is an artifact of low signal intensity and is not an indication that the system is not at equilibrium.

solvent gas, a measure of the equilibrium constant at a given temperature was obtained. Provided that no significant changes in heat capacity or any major shift in isomeric distribution occurs over a particular temperature range, a plot of  $\ln(K_{eq})$  versus  $T^{-1}$  can be expected to be linear with enthalpy change found from the slope and entropy change found from the intercept.

As a complement to experiments, the measured thermochemical properties were also calculated, as prescribed in Section 2.2.2.

## 4.3 Results and Discussion

### 4.3.1 Thermochemical Data

The van't Hoff plot shown in Figure 4.4 for reaction (1) was obtained over a 92 degree temperature range from 55 °C to 147 °C. From this plot,  $\Delta H_{exp}^\circ$  and  $\Delta S_{exp}^\circ$  for Eq. 4.4 were found to be  $-68.3 \pm 2 \text{ kJ}\cdot\text{mol}^{-1}$  and  $-90.5 \pm 10 \text{ J}\cdot\text{mol}^{-1}\cdot\text{K}^{-1}$ , respectively. An expected increase in the scatter of data points in Figure 4.4 was present due to the extremely low signal intensities that were observed for this system, yet excellent linearity remained over the entire temperature range.

The minimum energy structures for  $\text{NF}_2\text{H}\cdots\text{F}^-$ ,  $\text{CH}_3\text{OH}$  and  $\text{NF}_2\text{H}\cdots\text{F}\cdots\text{CH}_3\text{OH}$  obtained from B3LYP/6-311++G(d,p) optimizations are shown in Figure 4.5 as **II**, **III**, and **V**, respectively. The calculated values of  $\Delta H_{calc}^\circ$  and  $\Delta S_{calc}^\circ$  for reaction (1) based on these optimized structures were  $-70.9 \text{ kJ}\cdot\text{mol}^{-1}$  and  $-88.5 \text{ J}\cdot\text{mol}^{-1}\cdot\text{K}^{-1}$ , respectively, and are in

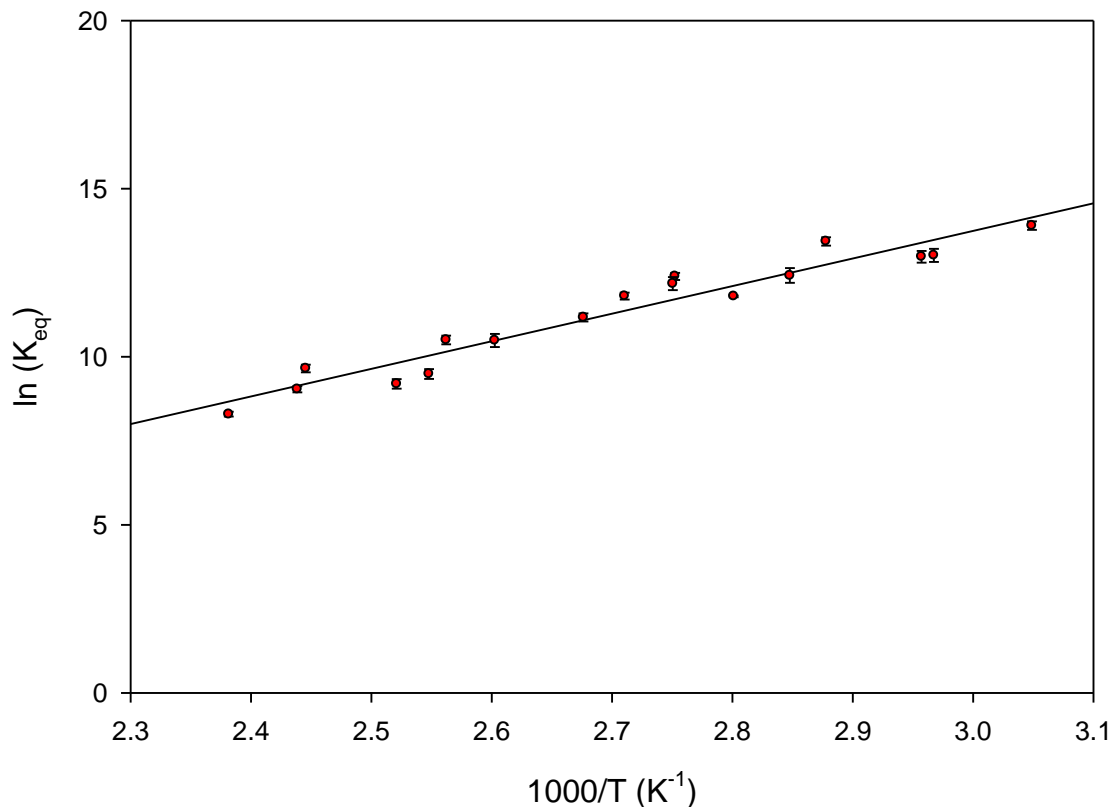


**Figure 4.4:** van't Hoff plot collected over a 92 degree temperature range from 55 °C to 147 °C for clustering of  $\text{NF}_2\text{H}\cdots\text{F}^-$  with  $\text{CH}_3\text{OH}$ . Error bars on each data point indicate standard deviation of 6-10 repetitive measurements of  $K_{\text{eq}}$  at each temperature.

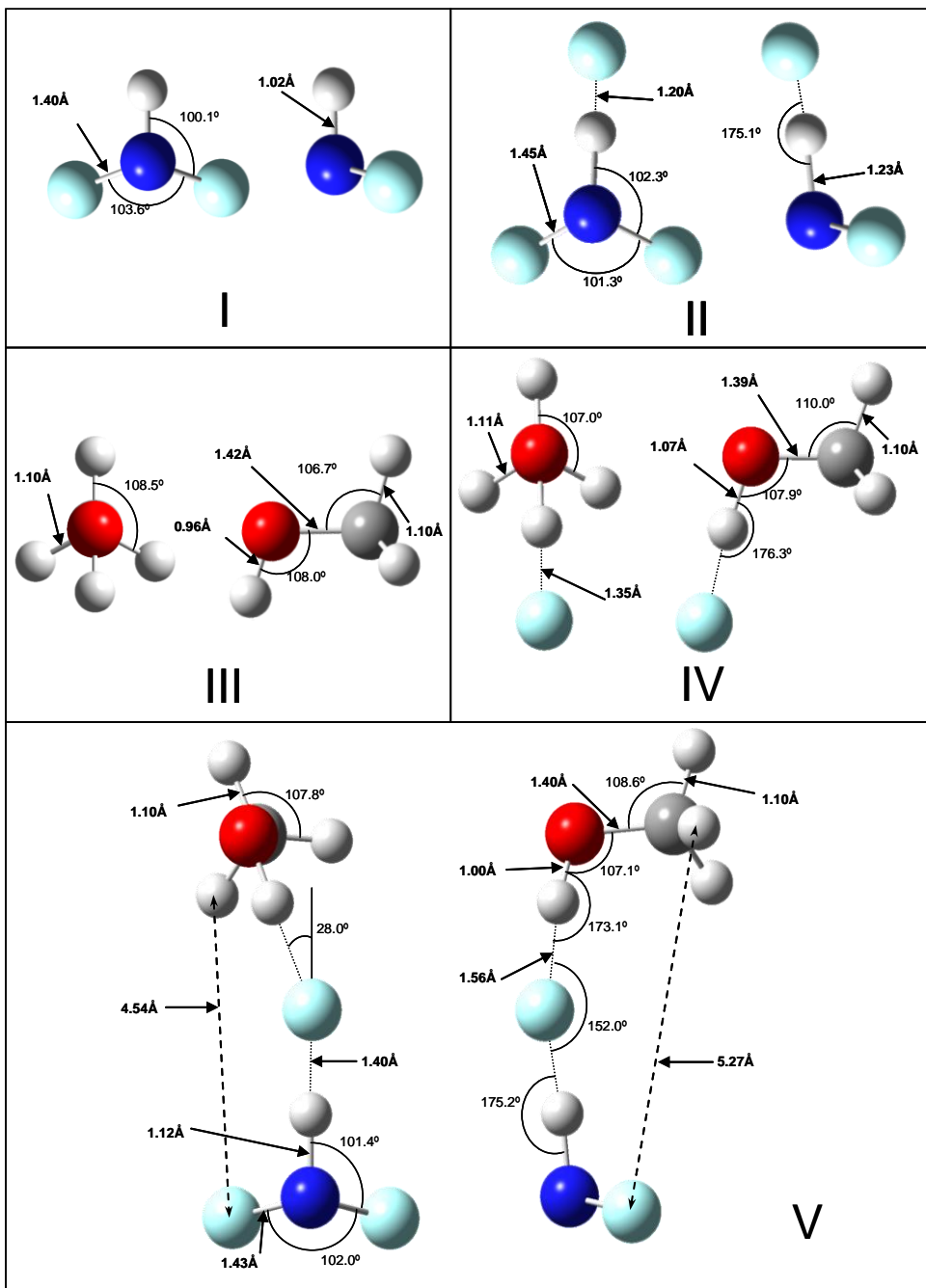


**Figure 4.5: Optimized geometries obtained from B3LYP/6-311++G(d,p) calculations:**  
**(I)  $\text{NF}_2\text{H}$  (II)  $\text{NF}_2\text{H}\cdots\text{F}^-$  (III)  $\text{CH}_3\text{OH}$  (IV)  $\text{CH}_3\text{OH}\cdots\text{F}^-$  (V) Fluoride bound dimer of  $\text{CH}_3\text{OH}$  and  $\text{NF}_2\text{H}$ . All distances are in Å and bond angles are in degrees.**

excellent agreement with the experimentally obtained values reported above. A more detailed discussion of all structures found in Figure 4.5 is given below.

Two different routes for the formation of  $\text{NF}_2\text{H}\cdots\text{F}\cdots\text{CH}_3\text{OH}$  clusters from  $\text{NF}_2\text{H}$ ,  $\text{CH}_3\text{OH}$ , and  $\text{F}^-$ , as shown in Figure 4.6, can be envisioned. The enthalpy change for Eq. 4.4 measured in the present study corresponds to the second step involved in Path 2. In order for this route to be followed, as a first step, a very strong hydrogen bond must be formed between  $\text{NF}_2\text{H}$  and  $\text{F}^-$ . The enthalpy change for this bond formation reaction was calculated to be  $-181.2 \text{ kJ}\cdot\text{mol}^{-1}$ , which, in terms of bond strength, comes close to equaling the very strong hydrogen bond strength present in  $\text{FHF}^-$  ( $\Delta H_{rxn}^\circ = -192 \text{ kJ}\cdot\text{mol}^{-1}$ ).<sup>99</sup> Path 1 in Figure 4.6 outlines an alternative route for the formation of the fluoride bound clusters of methanol and difluoramine. The initial step in Path 1 involves the addition of methanol to fluoride, which has been previously examined by DeTuri and Ervin using thermal collision induced dissociation<sup>92</sup> and by Larson and McMahon employing ion molecule reaction equilibria in an FT-ICR.<sup>59</sup> DeTuri and Ervin found  $\Delta H_{rxn}^\circ$  to be  $-123 \pm 9.2 \text{ kJ}\cdot\text{mol}^{-1}$ , while Larson and McMahon obtained  $\Delta H_{rxn}^\circ$  to be  $-124 \pm 8.4 \text{ kJ}\cdot\text{mol}^{-1}$ . Both of these measurements are consistent with the value of  $-129 \text{ kJ}\cdot\text{mol}^{-1}$  computed in this study. McMahon and co-workers<sup>59</sup> also report a  $\Delta S_{rxn}^\circ$  for this step of  $-94.6 \text{ J}\cdot\text{mol}^{-1}\cdot\text{K}^{-1}$ , which is in excellent agreement with the calculated value of  $-95.7 \text{ J}\cdot\text{mol}^{-1}\cdot\text{K}^{-1}$ .

Calculations were also performed in order to gain further insight into the effect of fluorine substitution in ammonia-fluoride hydrogen bonded systems by examining the formation equilibria of  $\text{NF}_n\text{H}_{3-n}\cdots\text{F}^-$  ( $n = 0..2$ ) clusters. The optimized geometries of these clusters are shown in Figure 4.7 and the thermochemical data for the cluster formation is

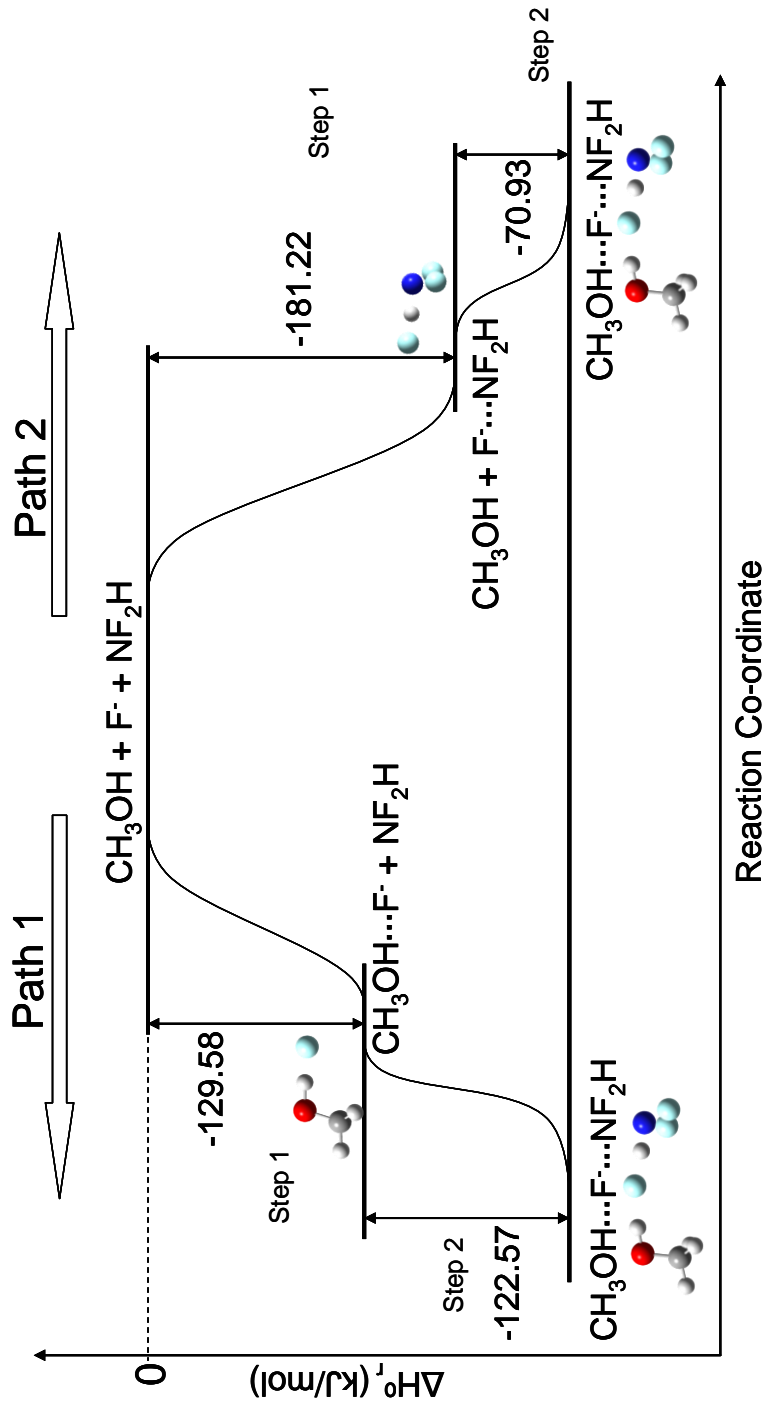


**Figure 4.6: Calculated reaction profile for the formation of  $\text{CH}_3\text{OH}\cdots\text{F}^-\cdots\text{NF}_2\text{H}$  clusters using B3LYP/6-311++G(d,p). Two pathways, each consisting of two steps, are shown.**

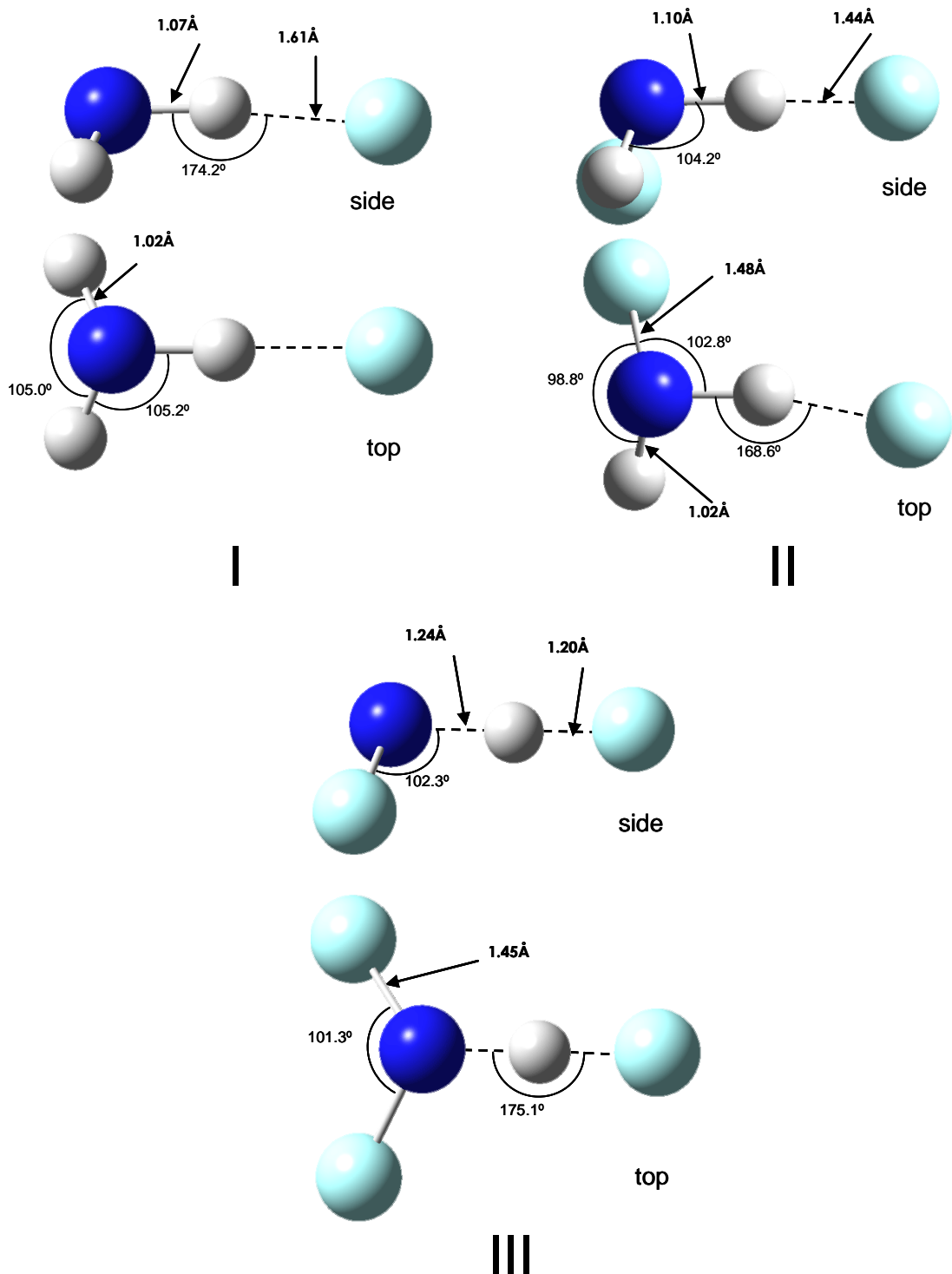


**Figure 4.7: Optimized geometries obtained from B3LYP/6-311++G(d,p) calculations:**  
**(I)  $\text{NH}_3 \cdots \text{F}^-$  (II)  $\text{NFH}_2 \cdots \text{F}^-$  (III)  $\text{NF}_2\text{H} \cdots \text{F}^-$ .**

given in Table 3-1. A detailed discussion of the structural aspects of the clusters shown in Figure 4.7 is given below. A plot of the standard fluoride binding enthalpy,  $\Delta H_{FBE}^\circ$ , versus standard enthalpy of deprotonation,  $\Delta H_{acid}^\circ$ , for the  $\text{NF}_n\text{H}_{3-n}\cdots \text{F}^-$  system is shown in Figure 4.8. The expected linear relationship between gas phase acidity and fluoride binding enthalpy was observed. Each sequential fluorine substitution for hydrogen in  $\text{NH}_3$  increases the strength of the  $\text{NH}\cdots\text{F}^-$  hydrogen bond by approximately  $60 \text{ kJ}\cdot\text{mol}^{-1}$ . Calculated and, where available, experimental literature values for the enthalpy of deprotonation of  $\text{NH}_3$ ,  $\text{NFH}_2$  and  $\text{NF}_2\text{H}$  are reported in Table 3-2. The expected increase in gas-phase acidity as a function of fluorination was observed, and in the case of  $\text{NH}_3$  good agreement between literature and calculated values can be seen. There is currently no reference value available for  $\text{NFH}_2$ , while a large uncertainty in the value for  $\text{NF}_2\text{H}$  exists. Three different values for the acidity of  $\text{NF}_2\text{H}$  are reported in the literature, spanning more than a  $50 \text{ kJ/mol}$  range. It is believed that the stronger, calculated gas-phase acidity reported in this work better represents the actual acidity of  $\text{NF}_2\text{H}$ . This conclusion is based on the excellent agreement of the measured thermochemical data for the  $\text{NF}_2\text{H}$  clusters reported above and a comparison to other simple hydrogen bond forming systems.

For  $\text{AXH}$  acids of the same gas-phase acidity, where  $\text{X} = \text{N}, \text{O}$ , or  $\text{F}$ , it has been shown that upon the formation of hydrogen bonds to an anionic base,  $\text{B}^-$ ,  $\text{AXH}\cdots\text{B}^-$  hydrogen bond strength increases when  $\text{X}$  is changed from  $\text{N}$  to  $\text{O}$  to  $\text{F}$ . A comparison of the deprotonation and fluoride binding energies of HF,  $\text{CFH}_2\text{CH}_2\text{OH}$  and  $\text{NF}_2\text{H}$  provides insight into what the relative magnitudes of each of these should be. In the case of HF, the enthalpy of deprotonation is  $1554 \text{ kJ}\cdot\text{mol}^{-1}$ <sup>156</sup>, while its binding energy to  $\text{F}^-$  is  $192 \text{ kJ}\cdot\text{mol}^{-1}$ <sup>199</sup>. In the

**Table 4-1: Summary of thermodynamic data pertaining to equilibrium reactions studied**

Reaction	$\Delta H_{rxn}^\circ$ (kJ·mol <sup>-1</sup> )	$\Delta S_{rxn}^\circ$ (J·K <sup>-1</sup> ·mol <sup>-1</sup> )	method/ reference
$NF_2H \cdots F^- + CH_3OH \rightleftharpoons NF_2H \cdots F^- \cdots CH_3OH$	-68.3 -70.9	-90.5 -88.5	a/d b/d
$CH_3OH \cdots F^- + NF_2H \rightleftharpoons NF_2H \cdots F^- \cdots CH_3OH$	-122.6	-95.8	b/d
$CH_3OH + F^- \rightleftharpoons CH_3OH \cdots F^-$	-129.6 -124	-95.7 -94.6	b/d c/e
$NF_2H + F^- \rightleftharpoons NF_2H \cdots F^-$	-181.2	-102.9	b/d
$NFH_2 + F^- \rightleftharpoons NFH_2 \cdots F^-$	-120.2	-98.9	b/d
$NH_3 + F^- \rightleftharpoons NH_3 \cdots F^-$	-67.9	-85.1	b/d

a - HPMS

b - MP2(full)/6-311++G(d,p)//B3LYP/6-311++G(d,p)

c – Ion Molecule Reaction Equilibrium

d - This study

e - J.W. Larson and T.B. McMahon<sup>59</sup>

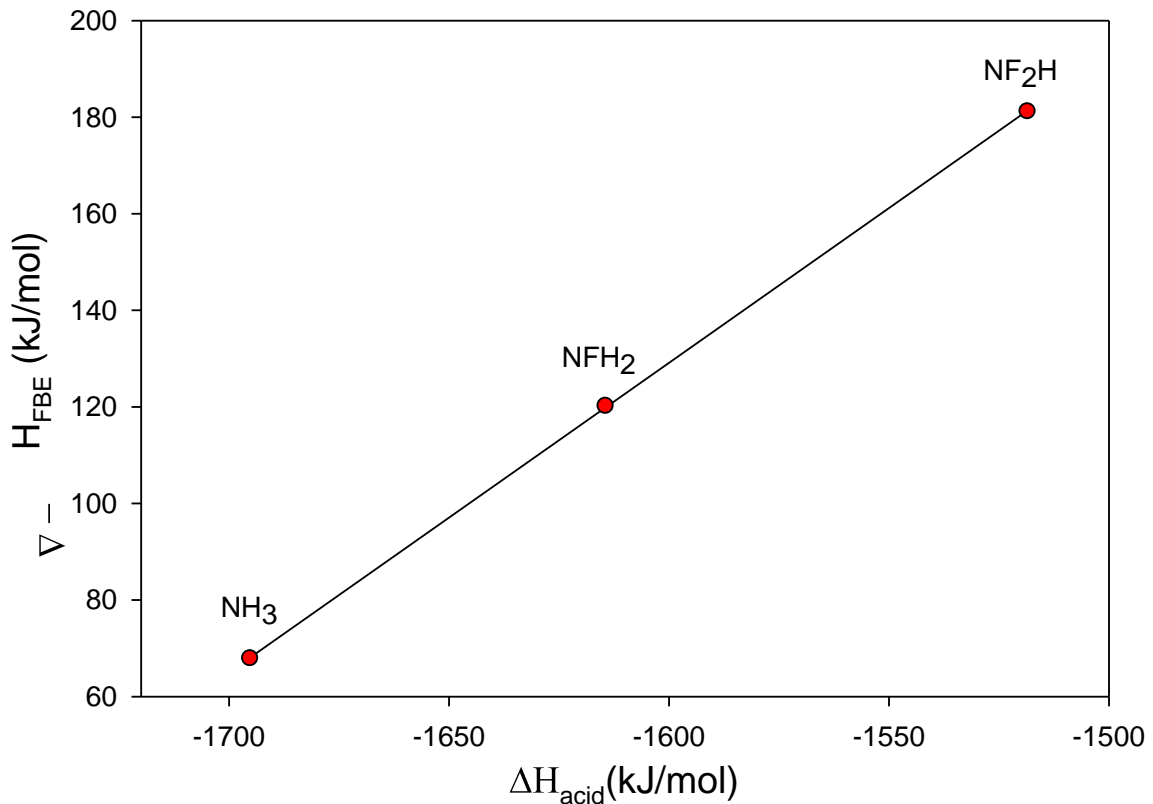


**Figure 4.8:** Plot of fluoride binding enthalpy ( $\Delta H_{\text{FBE}}$ ) versus enthalpy of deprotonation ( $\Delta H_{\text{acid}}$ ) demonstrates the effect of fluorine substitution on hydrogen bond strength in the  $\text{NF}_n\text{H}_{3-n}\cdots \text{F}^-$  system. Electronic energies//optimized geometries obtained from MP2(full)/6-311++G(d,p) // B3LYP/6-311++G(d,p) calculations.

**Table 4-2: Calculated and literature values of  $\Delta H_{rxn}^\circ$  (kJ·mol<sup>-1</sup>) for  $NF_nH_{3-n} \rightleftharpoons NF_nH_{2-n}^- + H^+$  using B3LYP/6-311++G(d,p) geometry optimizations and MP2(full)/6-311++G(d,p) electronic energy**

Reaction	Calculated (kJ·mol <sup>-1</sup> )	Literature (kJ·mol <sup>-1</sup> )
$NH_3 \rightleftharpoons NH_2^- + H^+$	-1695.2	-1687.8 a
$NFH_2 \rightleftharpoons NFH^- + H^+$	-1614.4	-
$NF_2H \rightleftharpoons NF_2^- + H^+$	-1518.5	-1552 b
		-1563 c
		-1506 d

a – C.T. Wickham-Jones, K.M. Ervin, *et. al.*<sup>97</sup>

b – I.A. Koppel, R.W. Taft, *et. al.*<sup>95</sup>

c – Ruckhaberle, N., et al.,<sup>96</sup>

d – I. Koppel, R. Pikver, et. al.<sup>100</sup> Estimated using  $\Delta G_{rxn}^\circ + T\Delta S_{rxn}^\circ$ , where  $T\Delta S_{rxn}^\circ = 29$  kJ·mol<sup>-1</sup>.

case of the 2-Fluoroethanol the enthalpy of deprotonation is  $1553 \text{ kJ}\cdot\text{mol}^{-1}$ <sup>101</sup>, while its binding energy to  $\text{F}^-$  is  $146 \text{ kJ}\cdot\text{mol}^{-1}$ <sup>159</sup>, an observable decrease in fluoride binding energy of nearly  $50 \text{ kJ}\cdot\text{mol}^{-1}$ . If the gas-phase acidity of  $\text{NF}_2\text{H}$  was closer to the literature value of  $1552 \text{ kJ}\cdot\text{mol}^{-1}$  the expected fluoride binding energy of  $\text{NF}_2\text{H}$  would be well below that of 2-Fluoroethanol, yet calculations predict a significantly larger value of  $181 \text{ kJ}\cdot\text{mol}^{-1}$ . In order to explain the unexpectedly large fluoride binding energy of  $\text{NF}_2\text{H}$  an increase in its gas-phase acidity would thus be anticipated, as predicted by calculations.

The ability of difluoramine to form very strong hydrogen bonds was essential in permitting this system to be studied. In order to measure equilibrium constants in an HPMS experiment a ratio of ion intensities less than 100 is desirable. Since only very small amounts of  $\text{NF}_2\text{H}$  were present in the ion source, it was necessary to introduce only very small amounts of methanol. In the absence of the very strong hydrogen bond found in  $\text{NF}_2\text{H}\cdots\text{F}^-$ , it would not have been possible to generate this species and thus to perform these experiments.

### 4.3.2 Structural Aspects of Cluster Formation

#### 4.3.2.1 $\text{NF}_n\text{H}_{3-n}\cdots\text{F}^-$ ( $n = 0..2$ ) Clusters

In the case of the sequentially fluorinated ammonia-fluoride clusters, interesting observations regarding the connection between NHF bond geometry and bond strength can be made. The  $\text{NH}_3\cdots\text{F}^-$  cluster depicted in 4.7I reveals that the formation of a N-H-F hydrogen bond of  $-67.9 \text{ kJ}\cdot\text{mol}^{-1}$  is accompanied by an increase in the NH bond length from  $1.01 \text{ \AA}$  in  $\text{NH}_3$  (calculated in this study) to  $1.07 \text{ \AA}$  in the cluster.

The mono-substitution of fluorine for hydrogen in ammonia to form  $\text{NFH}_2$  (Figure 4.7II) initiates changes in the geometry and physical properties of the species. The root of most of these changes is the electron withdrawing effect of fluorine which causes an increase in the gas-phase acidity of the species, an increase in the NH bond polarity and a stronger hydrogen bond ( $-120.2 \text{ kJ}\cdot\text{mol}^{-1}$ ) in the cluster with fluoride ion. A slightly larger shift in NH bond length from  $1.02 \text{ \AA}$  in  $\text{NFH}_2$  to  $1.10 \text{ \AA}$  in  $\text{NFH}_2\cdots\text{F}^-$  can be seen when the hydrogen bond is formed, also indicating a stronger hydrogen bond relative to that in  $\text{NH}_3\cdots\text{F}^-$ . The difluoro-substitution of ammonia to form  $\text{NF}_2\text{H}$  further amplifies the changes noted in the mono-fluorinated case. An additional increase in gas-phase acidity, bond polarity and hydrogen bond strength ( $-181.2 \text{ kJ}\cdot\text{mol}^{-1}$ ) can all be noted, as well as the increase in NH bond distance upon clustering with fluoride from  $1.03 \text{ \AA}$  in  $\text{NF}_2\text{H}$  to  $1.20 \text{ \AA}$  in  $\text{NF}_2\text{H}\cdots\text{F}^-$ .

The NH bond distance and total NHF bond distance across the  $\text{NF}_n\text{H}_{3-n}\cdots\text{F}^-$  system in order of increasing fluorination (i.e.  $\text{NH}_3$  to  $\text{NFH}_2$  to  $\text{NF}_2\text{H}$ ) are  $1.07 \text{ \AA}$ ,  $1.10 \text{ \AA}$ , and  $1.20 \text{ \AA}$  and  $2.67 \text{ \AA}$ ,  $2.54 \text{ \AA}$ , and  $2.44 \text{ \AA}$ , respectively. This decrease in total bond distance and hydrogen shift away from the nitrogen are strongly indicative of the increasing hydrogen bond strength and increased gas-phase acidity of the fluoro-amine species. It is interesting to note that in the case of the  $\text{NF}_2\text{H}$  fluoride adduct the proton is very close to being equally shared between N and F. This further supports the idea that the acidity of  $\text{NF}_2\text{H}$  is greater than that of HF since nitrogen acids are expected to bond more weakly than HF if they have comparable gas phase acidities.

#### **4.3.2.2 NF<sub>2</sub>H···F<sup>-</sup>···CH<sub>3</sub>OH Clusters**

The geometry of neutral difluoramine calculated in this study and shown in Figure 4.5I is in excellent agreement with the structure obtained from microwave spectroscopy reported in Figure 4.1. This structure is also consistent with the structure of difluoramine determined computationally by Demaison and co-workers using the same level of theory and basis set as that used in this study.<sup>102</sup> An examination of changes in geometry in proceeding from structures **4.5I** to **II** to **V** and **4.5III** to **IV** to **V**, as well as using the changes in enthalpy reported in the two pathways of Figure 4.6, permits a better understanding of this hydrogen bond system.

Path 1 in Figure 4.6 represents the initial clustering of methanol to fluoride, followed by the clustering of CH<sub>3</sub>OH···F<sup>-</sup> with difluoramine. The structures involved in this process are shown in Figure 4.5 as **III**, **IV** and **V**. The initial clustering of methanol to fluoride results in a strong hydrogen bond between the hydroxyl hydrogen of methanol and F<sup>-</sup> ( $\Delta H_{calc}^\circ = -129.6 \text{ kJ}\cdot\text{mol}^{-1}$ ) and results in an increase in O-H bond length from 0.96 Å to 1.07 Å, and a total O-F bond distance of 2.42 Å. The subsequent clustering with difluoramine reduces the strength of interaction between the fluoride and the hydroxyl group, resulting in a decrease in O-H bond length to 1.00 Å. This decreased OH···F hydrogen bond strength in the di-solvated fluoride cluster is also manifested in the increased total O-F bond distance of 2.56 Å.

Path 2 in Figure 4.6 represents the initial clustering of difluoramine with fluoride to form a very strong NH···F hydrogen bond ( $\Delta H_{calc}^\circ = -181.2 \text{ kJ}\cdot\text{mol}^{-1}$ ), followed by the clustering with methanol to form the mixed fluoride bound dimer. The very much stronger interaction of fluoride with NF<sub>2</sub>H relative to that with methanol is an indicator of the

surprising and substantial acidity of  $\text{NF}_2\text{H}$ . The initial formation of the  $\text{NH}\cdots\text{F}$  bond results in an increase in NH bond length from 1.02 Å to 1.23 Å and a total N-F bond length of 2.43 Å. Although the N-F bond length in **4.5II** is almost identical to the O-F bond length in **4.5IV**, one notable difference is that the  $\text{NH}\cdots\text{F}$  hydrogen bond possesses a near symmetric sharing of the proton. This once again indicates that the gas-phase acidity of  $\text{NF}_2\text{H}$  is comparable in magnitude to the acidity of HF, but also implies that it is substantially greater than that of  $\text{CH}_3\text{OH}$ . This greater acidity is also evident from the very significant decrease in the strength of interaction of  $\text{CH}_3\text{OH}$  with  $\text{NF}_2\text{H}\cdots\text{F}^-$ . In contrast, the strengths of interaction in the two steps in Path 1 were comparable. A decrease in N-H bond distance to 1.12 Å, an increase in F-H bond distance to 1.40 Å and an increase in N-F bond distance to 2.52 Å are also seen.

#### 4.4 Conclusion

The mixed fluoride bound cluster of difluoramine and methanol provides a wealth of information concerning strong and very strong hydrogen bonds. The effect of fluorine substitution on  $\text{NF}_n\text{H}_{3-n}\cdots\text{F}^-$  systems is quite evident as demonstrated by the monotonic increase in hydrogen bond strength in the order  $\text{NH}_3\cdots\text{F}^- < \text{NFH}_2\cdots\text{F}^- < \text{NF}_2\text{H}\cdots\text{F}^-$ . The enthalpy of deprotonation of  $\text{NF}_2\text{H}$  was found to be 1518.5  $\text{kJ}\cdot\text{mol}^{-1}$ . The predicted changes in enthalpy observed in the two pathways for the formation of the fluoride bound clusters of methanol and difluoramine are consistent with the geometric changes obtained from calculated structures. Further experiment to measure  $\Delta H_{rxn}^\circ$  and  $\Delta S_{rxn}^\circ$  of formation for

clusters of the type  $\text{NF}_n\text{H}_{3-n}\cdots\text{F}^-$  ( $n = 0..2$ ) or the addition of  $\text{NF}_2\text{H}$  to  $\text{CH}_3\text{OH}\cdots\text{F}^-$  would definitely be useful to confirm the predictions of the calculations performed in this study.

## Chapter 5

# Effects of Isomerization on the Measured Thermochemical Properties of Deprotonated Amino Acid/Protic-Solvent Clusters

### 5.1 Introduction

A complete description of amino acid behavior is undeniably dependent on the chemical environment in which the amino acid is found. It is abundantly demonstrated that amino acids adopt the zwitterionic form,  $^+H_3NCHRCOO^-$ , in solution and the solid state<sup>103-105</sup>, while in the gas phase, in the absence of solvent effects, they retain the canonical form,  $NH_3^+CHRCOOH$ <sup>104-106</sup>. How amino acids interact with other molecules can vary greatly, depending on both the form of the amino acid and the nature of the molecule to which it is binding. These interactions can range from tens of  $kJ \cdot mol^{-1}$ , as has been calculated for a single water molecule hydrogen bonded to canonical glycine<sup>107</sup>, to hundreds of  $kJ \cdot mol^{-1}$ , as in the case of a sodium cations bonded to the  $\alpha$ -amino acids<sup>108</sup>. Regardless of their nature or composition, a thorough understanding of these biologically important interactions is of the utmost importance.

Developments in sample introduction methods and soft ionization techniques have enabled researchers to use traditional mass spectrometry practices to investigate biologically-important systems in a variety of ways. To date, the experimental work investigating amino acids clustering to other ions/molecules primarily deals with protonated amino acids or alkali cation- amino acid complexes. While this provides a basis for understanding interactions with the positive amine terminus of a zwitterionic amino acid or peptide, no analogous

knowledge base exists which would shed insight into the chemical properties of the negatively charged carboxylate terminus. The only experimental investigation of a deprotonated amino acid interacting with another molecule is that of Wyttenbach, *et al.*,<sup>109</sup> in which deprotonated aspartic acid was clustered to 1-3 water molecules. The binding energy of the first water molecule was found to be  $38.5 \text{ kJ}\cdot\text{mol}^{-1}$ , while the binding energy of the subsequent molecules were 32.6 and  $29.3 \text{ kJ}\cdot\text{mol}^{-1}$ , respectively. In the absence of any other quantitative data on deprotonated amino acids with prototypical solvent molecules, it is clear that additional investigations of such species would offer considerable insight. In the present work, the thermochemical properties for the association of deprotonated glycine, alanine, valine and serine with various biologically important protic solvents ( $\text{H}_2\text{O}$ ,  $\text{CH}_3\text{OH}$ ,  $\text{C}_2\text{H}_5\text{OH}$ ) have been determined in an attempt to provide such insight.

Recently, the acidity scale of the 20 protein amino acids has been re-examined by Jones, *et al.*, using electrospray-quadrupole ion trap mass spectrometry and the extended kinetic method.<sup>110</sup> Glycine was found to have the lowest acid strength (enthalpy of deprotonation,  $\Delta H_{\text{acid}} = 1434 \text{ kJ}\cdot\text{mol}^{-1}$ ), while aspartic acid was found to have the strongest acid strength ( $\Delta H_{\text{acid}} = 1345 \text{ kJ}\cdot\text{mol}^{-1}$ ). As a consequence, the conjugate bases of glycine and aspartic acid, the deprotonated anionic forms of these amino acids, would be the most and least basic species, respectively. The enthalpies of deprotonation for alanine, valine and serine were determined to be 1430, 1431 and  $1391 \text{ kJ}\cdot\text{mol}^{-1}$ . If the addition of a first water molecule to deprotonated aspartic acid is presumed to involve an  $\text{OH}\cdots\text{O}^-$  ionic hydrogen bond between a negatively charged carboxylate oxygen of deprotonated aspartic acid and an OH bond of water, then the binding energy for this complex would be expected to be the

weakest of all hydrated anionic amino acid cluster system. If an ionic hydrogen bond,  $\text{AH}\cdots\text{B}^-$ , is considered to be comprised of a proton-donating  $\text{AH}$  moiety and a proton accepting  $\text{B}^-$  moiety, as the acid strength of  $\text{AH}$  and/or the basicity of  $\text{B}^-$  are raised, then the binding energy associated with this bond will increase, bond length will decrease and the bond will become more linear. Therefore, if the acid strength of the solvent,  $\text{AH}$ , were to increase while the basicity of  $\text{B}^-$  remains constant, then the measured bond strength for the resulting hydrogen bond would also be expected to increase. Likewise, if the acid strength of the solvent remains constant while the basicity of  $\text{B}^-$  increased, the hydrogen bond would once again be observed to strengthen. In the case of deprotonated aspartic acid ( $\text{B}^-$ ) forming a hydrogen bond to water ( $\text{AH}$ ), the basicity of  $\text{B}^-$  is expected to be the lowest of all the amino acids and, thus, should form the weakest interaction with water. Since the basicity of the conjugate base of glycine is expected to be the greatest of all amino acids, then it would be expected that the measured binding energy of deprotonated glycine to a particular solvent would represent the strongest such interaction of any deprotonated amino acid for that particular solvent.

As a first approximation, the chemistry of deprotonated anionic amino acids may be expected to behave in a similar manner to that of the acetate ion,  $\text{CH}_3\text{COO}^-$ . The clustering of acetate to many protic solvents has been investigated and it has been found that the  $\Delta H_{rxn}^\circ$  for the formation of water, methanol and ethanol clusters are  $-68.6^{111}$ ,  $-73.6^{112}$  and  $-86.6^{113}$   $\text{kJ}\cdot\text{mol}^{-1}$ , respectively. The corresponding binding energies thus increase in the expected fashion. Since the acid strength of acetic acid ( $\Delta H_{acid}^\circ = 1456 \text{ kJ}\cdot\text{mol}^{-1}$ )<sup>114</sup> is less than that of glycine, the basicity of its conjugate base, acetate, is greater than that of deprotonated

glycine. Using electronic structure calculations, Topel, *et al.*, have calculated the structure of deprotonated glycine and have shown a carboxylate oxygen interacts with the NH<sub>2</sub> moiety *via* an bifurcated hydrogen bond.<sup>115</sup> This intramolecular hydrogen bond environment would thus weaken the basicity of this carboxylate oxygen, potentially weakening any subsequent hydrogen bond that may form. These two observations regarding the basicity of conjugate bases and the presence of a bifurcated hydrogen bond lead to the prediction that interactions between deprotonated glycine and solvents will be weaker than that of the analogous acetate-solvent clusters.

One mass spectrometric technique which has proven to be an invaluable tool in the study of the gas-phase equilibria of amino acids and solvents is high pressure mass spectrometry. Raspovov and McMahon have shown that HPMS experiments involving gas-phase glycine can be carried out by placement of a solid sample of the analyte in direct thermal contact with the heated walls of a high pressure ion source.<sup>116</sup> This modification in HPMS sample introduction has allowed for the direct measurement of the thermochemical properties of various protonated amino acid and nucleic acid clusters<sup>117-119</sup> and paved the way for further HPMS studies of previously inaccessible systems.

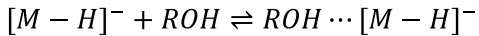
## 5.2 Experimental

All thermodynamic measurements were made using the PHPMS described in detail in Section 2. When solid amino acid was placed in direct thermal contact with the walls of the high pressure ion source, it was determined that above 120°C, sufficient number density of gaseous amino acid was present to produce useable ion signal. To deprotonate the amino

acids, chemical ionization from a mixture of 1% N<sub>2</sub>O in CH<sub>4</sub> was used as described below. Varying amounts of the desired protic solvents (solvent partial pressure between .01% and 1% of the total pressure) were flowed into the ion source at total pressures between 6 and 7 torr and temperatures between 120 °C and 180 °C, depending on the equilibrium reaction being examined. Glycine, L-alanine, L-valine, L-serine (Sigma Aldrich), N<sub>2</sub>O (Matheson, 99.99% purity), CH<sub>4</sub> (Praxair, 99.97% purity), CH<sub>3</sub>OH (Sigma Aldrich, 99.8% purity) and C<sub>2</sub>H<sub>5</sub>OH (Commercial Alcohols Inc.) were used as supplied from the manufacturer without any further purification performed, while any H<sub>2</sub>O used was purified using a Milli-Q filtration system. Upon bombardment of this reactant gas mixture by a 2 kV pulsed (60 µs) electron beam, the desired anionic species were produced within the ion source through the series of ion molecule reactions outlined in Eq. 5.1 - Eq. 5.4.

Initial electron bombardment of N<sub>2</sub>O generates the highly reactive O<sup>-·</sup>, Eq. 5.1, which subsequently abstracts a proton from CH<sub>4</sub>, forming OH<sup>-</sup>, Eq. 5.2. Gaseous hydroxide ions deprotonate the amino acids, M, according to Eq. 5.3 and once [M - H]<sup>-</sup> has been formed, it is free to undergo clustering with ROH, Eq. 5.4, where R = H, CH<sub>3</sub> or C<sub>2</sub>H<sub>5</sub>.





5.4

It can be noted that at the operating pressures and temperatures of the ion source approximately  $10^8$  collisions per second take place, thus ensuring that all species present have been thermalized to the known source temperature.

Figure 5.1 depicts typical logarithmic intensity-time profiles collected for the pair of ions involved in Eq. 5.4, while the inset shows typical normalized intensity-time profiles. Each plot is the result of an accumulation of ion intensity as a function of time for 2000 successive electron beam pulses. The rapid ion formation processes outlined in Eq. 5.1 – Eq. 5.4 result in the immediate onset of ion signal after the end of the electron beam pulse. From these intensity-time profiles it can be seen that equilibrium is reached in approximately 4 ms.

By taking the ratio of product/reactant ion intensities during the period of time in which the two ions were in equilibrium (after 4 ms), and dividing by the partial pressure of the neutral solvent gas, measurements of the equilibrium constant at several temperatures were made. Six to ten measurements of  $K_{eq}$  were obtained at each temperature and the standard deviation displayed as error bars for each point are shown in the resulting van't Hoff plots. According to the van't Hoff equation, Eq. 1.11, measurements of  $K_{eq}$  at various temperatures yields the change in enthalpy and entropy for a given equilibrium process. Provided that no significant changes in heat capacity or any major shift in isomeric distribution occurs over a particular temperature range, a plot of  $\ln(K_{eq})$  versus  $T^{-1}$  is

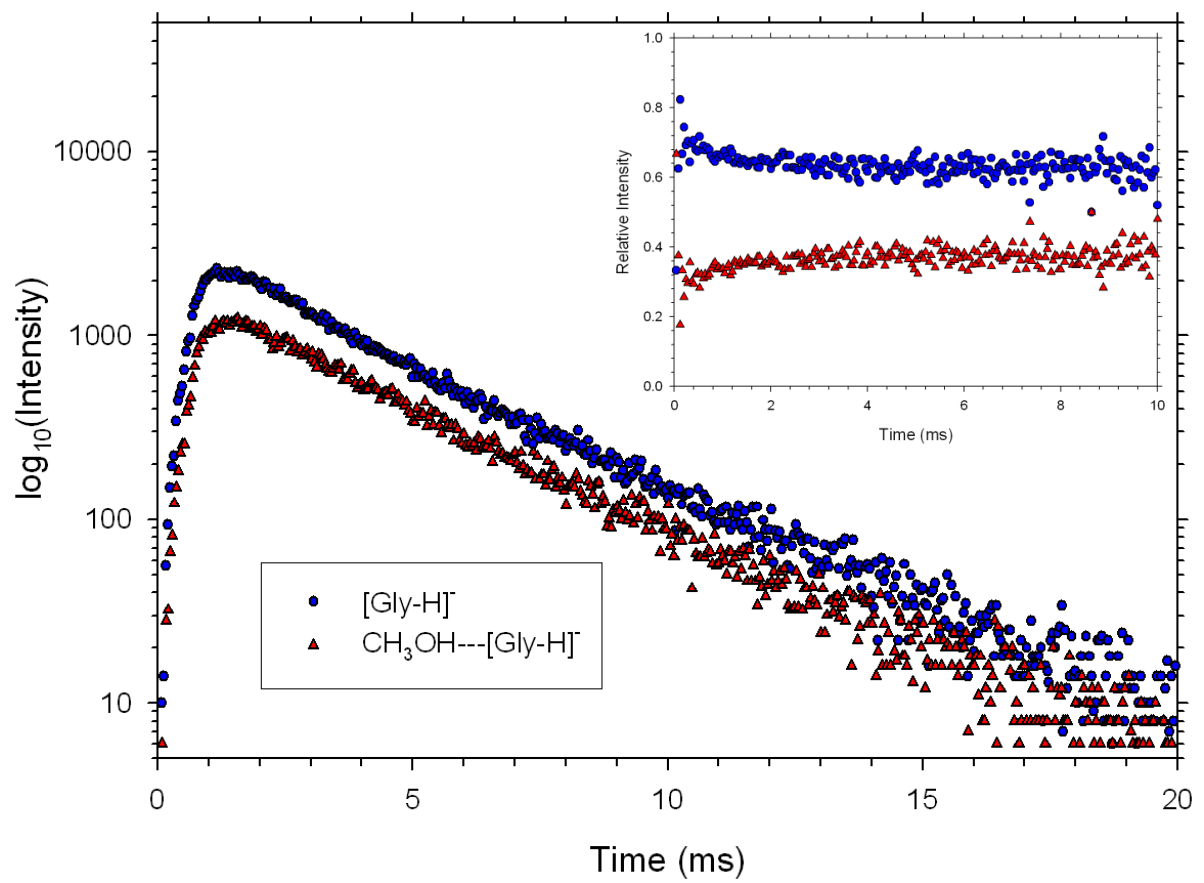
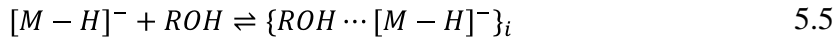


**Figure 5.1:** Typical  $\log_{10}(\text{Intensity})$  – Time profiles for the clustering of deprotonated glycine with an ROH solvent. Inset: normalized Intensity-Time profiles.

expected to be linear. From this straight line, enthalpy change is obtained from the slope and entropy change from the intercept. The experimentally derived change in free energy at any temperature,  $\Delta G_{T,exp}^\circ$ , can then be determined using Eq. 1.9,

For  $N$  thermodynamically accessible isomers of the cluster ion formed in Eq. 5.4, the system of equations represented by Eq. 5.5, provides a more complete description of the equilibrium processes taking place within the ion source. Each of the  $N$  equilibrium processes expressed in Eq. 5.5 has an associated thermodynamic equilibrium constant,  $K_i$ , shown in its functional form in Eq. 5.6.



$$K_i = \frac{I_{ROH \cdots [M-H]^-_i}}{I_{[M-H]^-} \cdot P_{ROH}} \cdot P_o \quad 5.6$$

Since mass analysers of mass spectrometers are incapable of discriminating among particular isomers of an ionic cluster, the intensity of the ion signal collected at a particular m/z,  $I_{m/z}$ , will be the sum of the contributions of all  $N$  isomers present at that m/z, Eq. 5.7. The observable quantity actually measured *via* HPMS in this case, denoted as  $\mathcal{K}_{exp}$ , can be expressed as Eq. 5.8 and related to the equilibrium constants of Eq. 5.6 *via* Eq. 5.9. In order to extract thermochemical information from a system of such isomers, the exponential form of Eq. 1.11 can be substituted into Eq. 5.9 to obtain Eq. 5.10, which can then be used, in principle, to fit a plot of  $\mathcal{K}_{exp}$  as a function of temperature. Doing so would yield values for

$\Delta H_{exp,i}^\circ$  and  $\Delta S_{exp,i}^\circ$ , which correspond to the enthalpy and entropy changes for each of the  $N$  equilibrium processes related to the formation of each isomer.

$$Im_{/z} = \sum_{i=1}^N Im_{z,i} \quad 5.7$$

$$\mathcal{K}_{exp} = \frac{\sum_{i=1}^N I_{ROH \cdots [M-H]^-_i} \cdot P_o}{I_{[M-H]^-} \cdot P_{ROH}} \quad 5.8$$

$$\mathcal{K}_{exp} = \sum_{i=1}^N K_i \quad 5.9$$

$$\mathcal{K}_{exp} = \sum_{i=1}^N e^{\left( -\frac{\Delta H_{exp,i}^\circ}{RT} + \frac{\Delta S_{exp,i}^\circ}{R} \right)} \quad 5.10$$

It can also be pointed out that Eq. 5.10 is the starting point from which all equations in isomer group thermodynamics are derived.<sup>39</sup> Application of Eq. 5.10 to certain limiting cases allows for the ability to directly measure various properties of an equilibrium system. Using Eq. 2.8, it can be shown that at 400 K, if one isomer is less favourable than another by 10 kJ·mol<sup>-1</sup> and no significant barriers to interconversion exist, the number density of the higher energy isomer will be less than 5% of that of the more stable isomer. At the same temperature, if an isomer is > 20 kJ·mol<sup>-1</sup> higher in energy than another, it will constitute < 0.2% of the mixture. The contributions of these higher energy isomers to the total measured

ion intensity diminishes rapidly and, hence, the higher order terms in the summation of Eq. 5.10 ( $i > 1$ ) can be ignored. If the number density of the most stable isomer is much greater than any others, Eq. 5.10 reduces to Eq. 1.11 and a conventional van't Hoff plot can be obtained, whose slope and intercept will be determined by the enthalpy and entropy changes of the lowest energy isomer.

Another limiting case of interest involves the presence of  $N$  isomers possessing identical thermochemical properties,  $\Delta H_{exp}^\circ$  and  $\Delta S_{exp}^\circ$ . It can be shown that Eq. 5.10 can be reduced to Eq. 5.11,

$$\ln(\mathcal{K}_{exp}) = -\frac{\Delta H_{exp}^\circ}{RT} + \frac{\Delta S_{exp}^\circ}{R} + \ln N, \quad 5.11$$

which closely resembles Eq. 1.11 plus a factor of  $\ln N$ . If a plot of  $\mathcal{K}_{exp}$  versus  $T^{-1}$  is made, a straight line is expected with a slope and y-intercept equal to  $-\Delta H_{exp}^\circ/R$  and  $\Delta S_{exp}^\circ/R + \ln N$ , respectively. While the value of  $\Delta H_{exp}^\circ$  can be obtained in a manner similar to that of the one-isomer case presented above, the same cannot be said about for  $\Delta S_{exp}^\circ$ . If it were assumed that no isomers were present and the y-intercept was multiplied by  $R$  to yield  $\Delta S_{exp}^\circ$ , as in the dominant isomer case presented above, an error of  $R \ln N$  would be introduced. It is interesting to note that this error of  $R \ln N$  is equivalent to the value of  $\Delta S_{mix}^\circ$  predicted by Eq. 2.11, which was obtained from the statistical thermodynamic modeling of a system of  $N$  ideal gases of equal abundance, which were isothermally mixed in a common volume. Such an error of  $R \ln N$  can be expected to arise in any mass spectrometric

experiment in which several indistinguishable, interconverting isomers are present. The derivation of the error of  $RlnN$  presented here has the advantage of being based on a very real model of how ions are discriminated and detected within the mass spectrometer, as opposed to the hypothetical idealized model introduced in Section 1. In fact, the effects of this mass-spectrometrically derived error introduced by ignoring the presence of isomers is not unique to HPMS, but would be present in any mass spectrometry technique which attempts to measure thermochemical values through a ratio of ion intensities.

Calculations were performed to compliment the HPMS measurements and gain further insight into the energetic and structural properties of this anion-protic solvent clustering process. For each species involved in Eq. 5.4, the electronic energy, vibrational frequencies and thermochemical properties were calculated as detailed in Section 2.2.2. The vibrational frequencies were extracted from the GAUSSIAN output files with the aid of the C++ program given in Appendix C. A MathCad worksheet (Appendix D) was then used to both scale and combine the vibrational line spectra for any isomers of a particular cluster, then apply a Lorentzian line-shape function for future comparison to an IR spectra.

### 5.3 Results and Discussion

In order to validate the use of the chosen computational method and basis set, the thermochemical properties for the deprotonation of glycine were calculated and compared to those available in the literature. Using the method described in Section 2, the enthalpy and free energy of deprotonation were calculated to be 1433.1 and 1402.7  $\text{kJ}\cdot\text{mol}^{-1}$ , respectively. The calculated enthalpy of deprotonation was observed to be in excellent agreement with the

recently obtained experimental value of  $1434 \text{ kJ}\cdot\text{mol}^{-1}$ , from Jones, *et al.*<sup>110</sup> Moreover, excellent agreement was also observed upon comparison to experimental values measured from Locke and McIver<sup>120</sup> ( $1433, 1404 \text{ kJ}\cdot\text{mol}^{-1}$ ) and those of Caldwell, *et al.*<sup>121</sup> ( $1429, 1400 \text{ kJ}\cdot\text{mol}^{-1}$ ).

The van't Hoff plots associated with the equilibrium reactions of Eq. 5.4 are shown in Figure 5.2 - Figure 5.5. Excellent linearity was observed for each of these plots, and, as given in Eq. 1.11, measurements of  $\Delta H_{exp}^\circ$  and  $\Delta S_{exp}^\circ$  were obtained from the slope and intercept, respectively, and reported in Table 5-1. The free energy change at  $298 \text{ K}$ ,  $\Delta G_{298,exp}^\circ$ , was then obtained using Eq. 1.9 and can also be found in Table 5-1. It can be noted that the binding enthalpy of one water molecule to deprotonated glycine is much greater than ( $> 30 \text{ kJ}\cdot\text{mol}^{-1}$ ) that observed for deprotonated aspartic acid by Wyttenbach. In fact, the binding enthalpies for all of the examined amino acids were more exothermic than that of deprotonated aspartic acid. As noted in Section 5.1, this is expected as the basicities of the conjugate bases of these amino acids are greater than that of aspartic acid.

### 5.3.1 Clustering of Deprotonated Glycine with ROH

For each system, optimized geometries for two basic types of clusters were found, Figure 5.6**I-III** and Figure 5.6**IV-VI**, which can be described as attachments of ROH to either the carboxylate or amine moiety of deprotonated glycine. The corresponding thermochemical properties associated with the formation of **5.6I-VI**,  $\Delta H_{calc}^\circ$ ,  $\Delta S_{calc}^\circ$  and  $\Delta G_{298,calc}^\circ$  are reported in Table 5-2. It is clear that attachment of ROH to the carboxylate

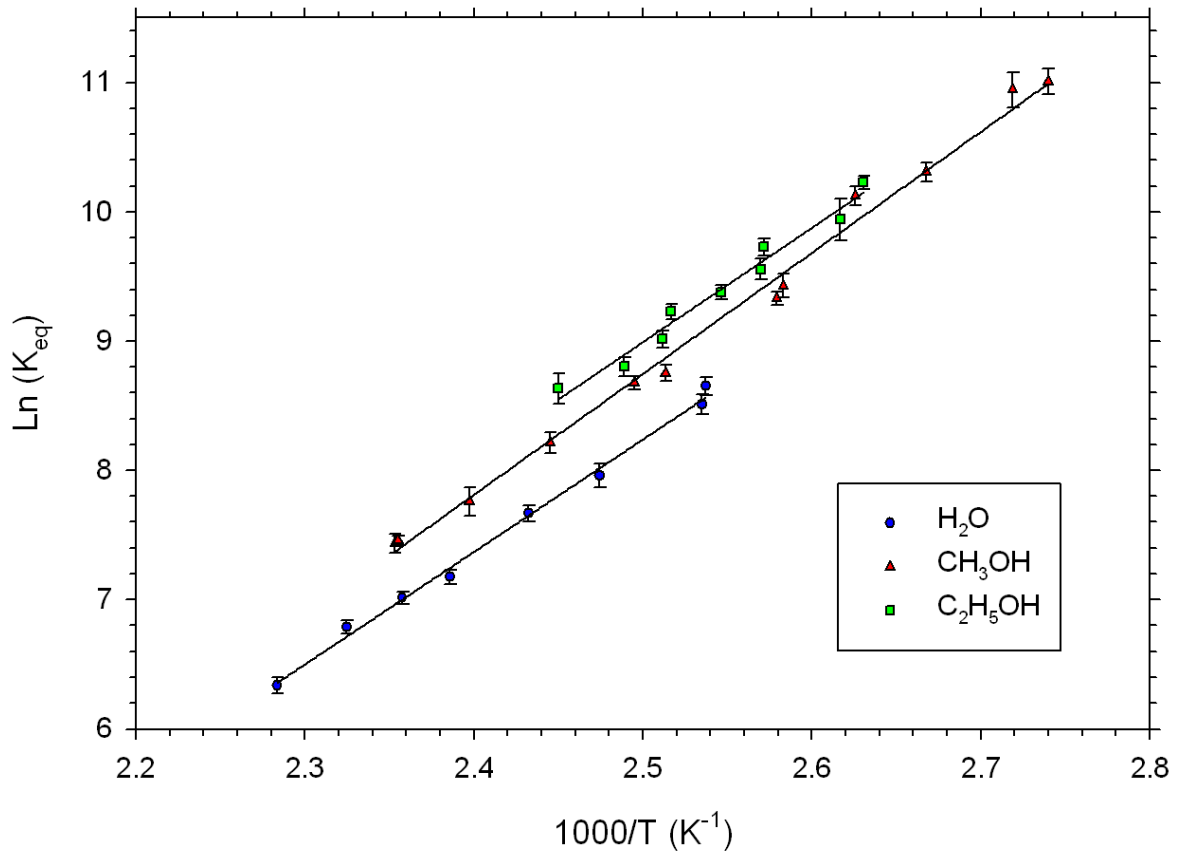


**Figure 5.2:** van't Hoff Plots for the clustering of  $NH_2CH_2COO^-$  with  $H_2O$ ,  $CH_3OH$  and  $C_2H_5OH$ .

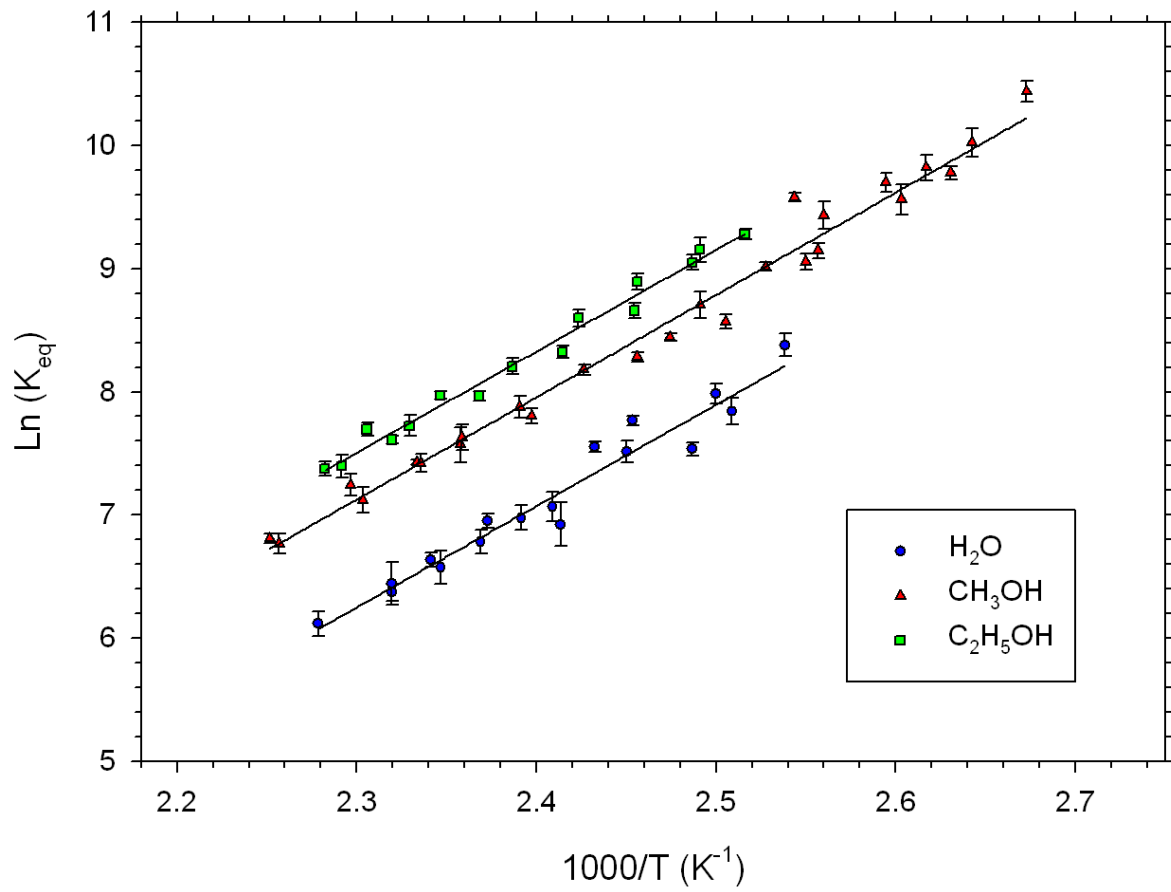


**Figure 5.3:** van't Hoff Plots for the clustering of  $NH_2CH(CH_3)COO^-$  with  $H_2O$ ,  $CH_3OH$  and  $C_2H_5OH$ .

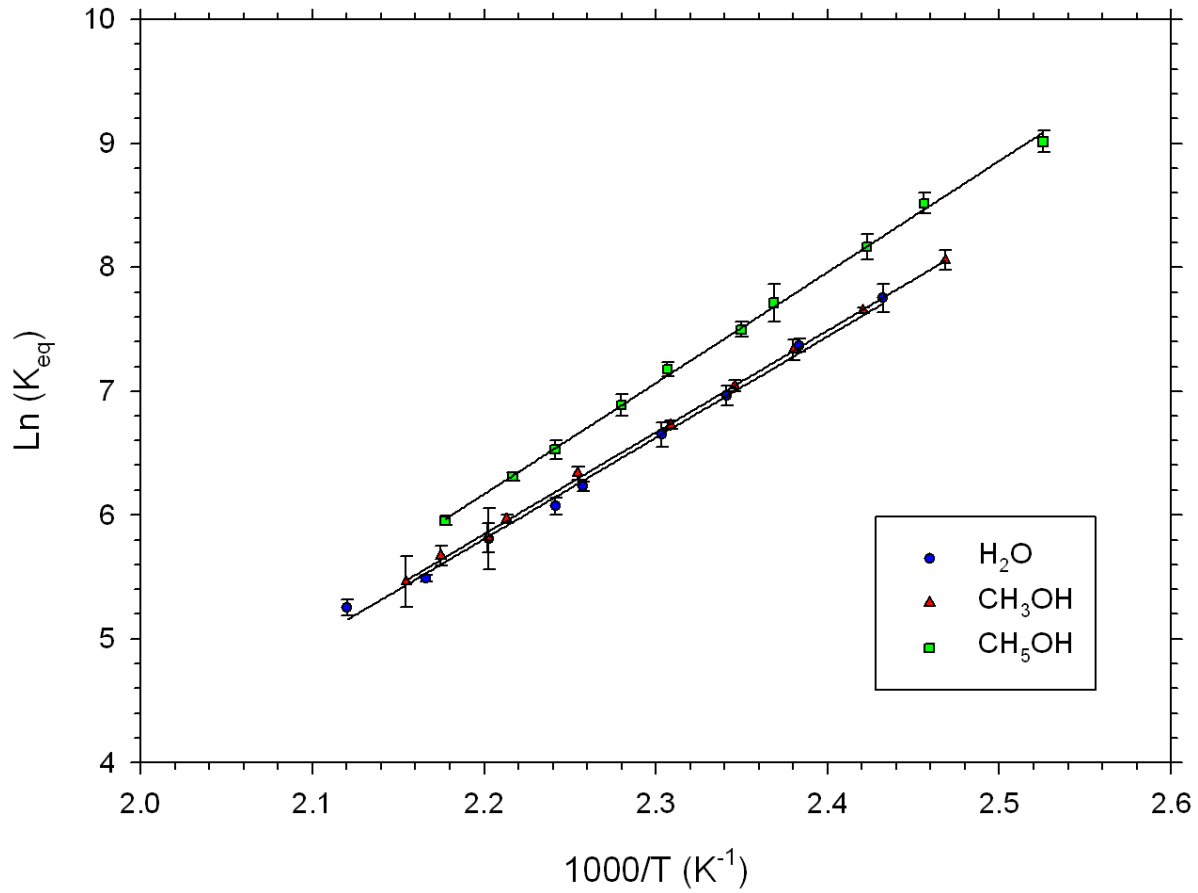


**Figure 5.4:** van't Hoff Plots for the clustering of  $NH_2CH(CH(CH_3)_2)COO^-$  with  $H_2O$ ,  $CH_3OH$  and  $C_2H_5OH$ .

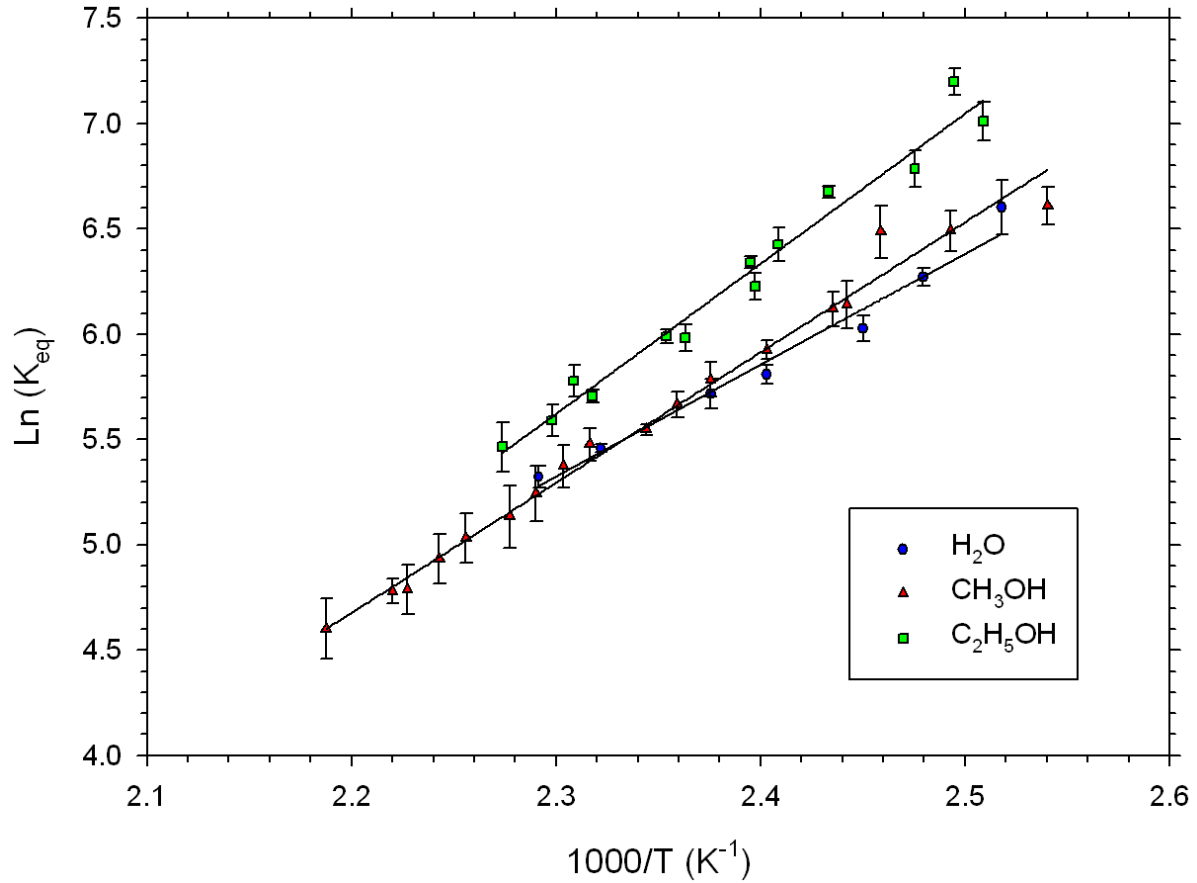


**Figure 5.5:** van't Hoff Plots for the clustering of  $NH_2C(CH_2OH)COO^-$  with  $H_2O$ ,  $CH_3OH$  and  $C_2H_5OH$ .

**Table 5-1: Thermochemical Properties for the Formation of ROH ··· [M – H]<sup>-</sup> (M = Gly, Ala, Val, Ser; R = H, CH<sub>3</sub>, C<sub>2</sub>H<sub>5</sub>) determined via High Pressure Mass Spectrometry**

Cluster		$\Delta H_{obs}^\circ$ ( $\pm 2.0 \text{ kJ}\cdot\text{mol}^{-1}$ )	$\Delta S_{obs}^\circ$ ( $\pm 10.0 \text{ J}\cdot\text{K}^{-1}\cdot\text{mol}^{-1}$ )	$\Delta G_{298,obs}^\circ$ <sup>†</sup> ( $\pm 4.1 \text{ kJ}\cdot\text{mol}^{-1}$ )
[M – H] <sup>-</sup>	ROH			
[Gly – H] <sup>-</sup>	H <sub>2</sub> O	-72.5	-112.7	-38.9
	CH <sub>3</sub> OH	-71.1	-105.5	-39.6
	C <sub>2</sub> H <sub>5</sub> OH	-73.5	-109.0	-41.0
[Ala – H] <sup>-</sup>	H <sub>2</sub> O	-69.1	-107.0	-37.2
	CH <sub>3</sub> OH	-69.9	-101.5	-39.6
	C <sub>2</sub> H <sub>5</sub> OH	-68.6	-95.3	-40.2
[Val – H] <sup>-</sup>	H <sub>2</sub> O	-68.9	-103.3	-38.1
	CH <sub>3</sub> OH	-68.3	-101.6	-38.0
	C <sub>2</sub> H <sub>5</sub> OH	-74.2	-111.9	-40.8
[Ser – H] <sup>-</sup>	H <sub>2</sub> O	-44.7	-58.6	-27.2
	CH <sub>3</sub> OH	-51.1	-73.4	-29.2
	C <sub>2</sub> H <sub>5</sub> OH	-59.5	-90.1	-32.7

<sup>†</sup>  $\Delta G_T^\circ = \Delta H^\circ - T\Delta S^\circ$

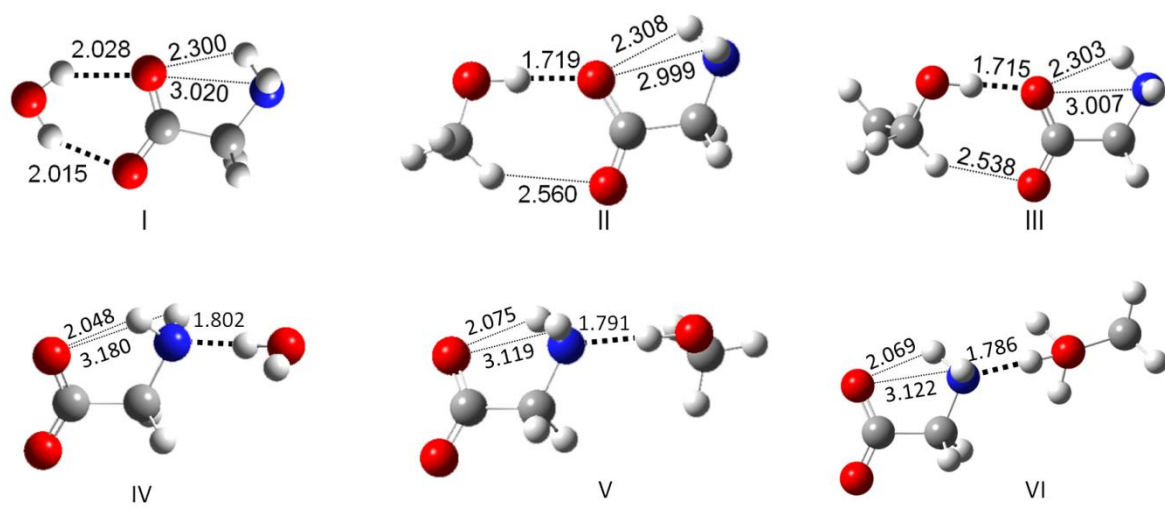


**Figure 5.6:** Lowest energy structures obtained using MP2(full)/6-311++G(d,p) // B3LYP/6-311++G(d,p), for the attachment of ROH to the carboxylate or amine moiety of  $\text{NH}_2\text{CH}_2\text{COO}^-$ . Distances are in units of angstroms.

**Table 5-2: Measured and Calculated Thermochemical Properties for the Formation of ROH ··· [Gly – H]<sup>-</sup>, R = H, CH<sub>3</sub>, C<sub>2</sub>H<sub>5</sub>**

Cluster	$\Delta H^\circ$ (kJ·mol <sup>-1</sup> )	$\Delta S^\circ$ (J·K <sup>-1</sup> ·mol <sup>-1</sup> )	$\Delta G_{298}^\circ$ <sup>†</sup> (kJ·mol <sup>-1</sup> )	method
<i>H</i> <sub>2</sub> O ··· [Gly – H] <sup>-</sup>	-72.5 ± 2.0	-112.7 ± 10.0	-38.9 ± 4.1	a
	-70.3	-113.6	-36.5	b
	-73.1	-122.7	-36.6	c
	-53.7	-110.6	-20.7	d
<i>CH</i> <sub>3</sub> <i>OH</i> ··· [Gly – H] <sup>-</sup>	-71.1 ± 2.0	-105.5 ± 10.0	-39.6 ± 4.1	a
	-68.9	-105.0	-37.6	b
	-71.4	-120.9	-35.4	c
	-57.2	-116.4	-22.5	d
<i>C</i> <sub>2</sub> <i>H</i> <sub>5</sub> <i>OH</i> ··· [Gly – H] <sup>-</sup>	-73.5 ± 2.0	-109.0 ± 10.0	-41.0 ± 4.1	a
	-73.9	-110.1	-41.1	b
	-74.5	-121.0	-38.4	c
	-58.3	-120.5	-22.3	d

<sup>†</sup> -  $\Delta G_T^\circ = \Delta H^\circ - T\Delta S^\circ$

a – HPMS

b – Calculated for distribution of all isomers

c – Calculated for most stable isomer

d – Calculated for solvent attachment to amine group of deprotonated glycine

moiety, such as in the case seen in **5.6I-III**, is considerably more favorable than attachment to the amine group, **5.6IV-VI**. Hence, the amine-bonded clusters would be present in negligible amounts since their relatively higher free energy provides a significant thermodynamic barrier to their formation. In general, the values of  $\Delta H^\circ$  and  $\Delta G_{298}^\circ$  calculated for the most stable isomers were in good agreement to those obtained from experiment, while poorer agreement was observed for  $\Delta S^\circ$ . The average deviation between measured and calculated values of  $\Delta H^\circ$ ,  $\Delta S^\circ$  and  $\Delta G_{298}^\circ$  for all three solvents are 13.3  $\text{kJ}\cdot\text{mol}^{-1}$ , 47.0  $\text{J}\cdot\text{K}^{-1}\cdot\text{mol}^{-1}$  and 2.0  $\text{kJ}\cdot\text{mol}^{-1}$ .

In addition to the lowest energy structures, several other isomers for the attachment of ROH to the carboxylate moiety of deprotonated glycine were also optimized. Geometries and calculated thermochemical values for these other isomers are given in Figure 5.7 and Table 5-3, respectively. In order to probe the feasibility of the presence of these other isomers, potential energy profiles for prototypical rotational and translational isomerizations found within this clustering system have been calculated, Figure 5.8. Given the experimental conditions of the high pressure ion source, it is clear that neither thermodynamic nor kinetic barriers to isomerization exist for the two profiles shown in Figure 5.8, nor would they be expected to exist for any other isomerization process between the isomers shown in Figure 5.6 and Figure 5.7. Hence, a statistical distribution of all isomers shown will be experimentally accessible.

Since the isomeric clusters of Eq. 5.4 are in equilibrium with one another, the relative isomer abundance was determined *via* Eq. 2.8, where  $A_i$  is the relative abundance of isomer i compared to the most stable isomer j, ( $A_j = 1$ ). The relative isomer distributions for the

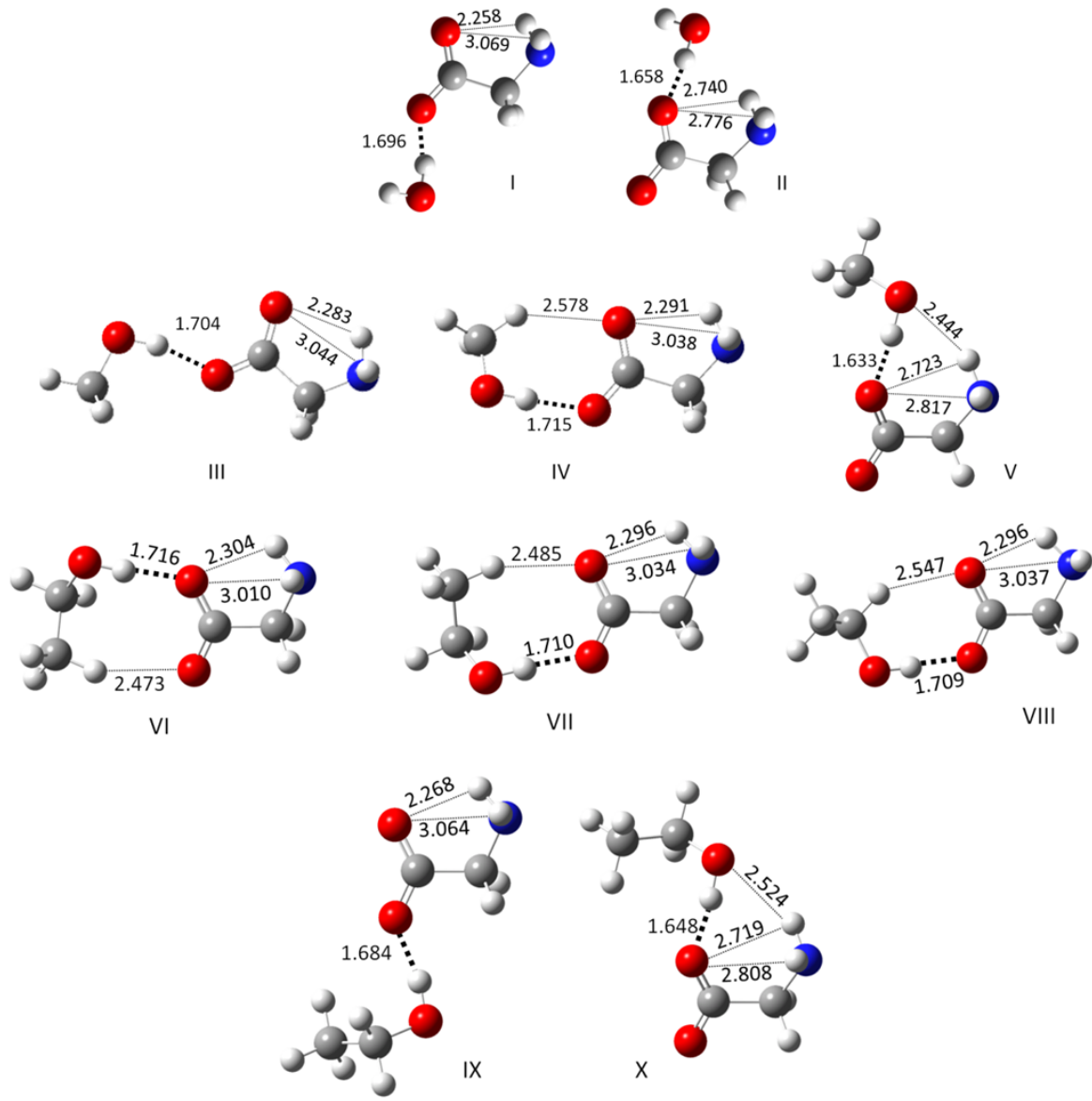


**Figure 5.7: Isomeric forms obtained using MP2(full)/6-311++G(d,p) // B3LYP/6-311++G(d,p), for the attachment of ROH to the carboxylate moiety of  $\text{NH}_2\text{CH}_2\text{COO}^-$ . Distances are in units of angstroms.**

**Table 5-3: Calculated Thermochemical Properties for Higher Energy Isomers of ROH ··· [Gly – H]<sup>-</sup>, R = H, CH<sub>3</sub>, C<sub>2</sub>H<sub>5</sub> obtained using MP2(full)/6-311++G(d,p)//B3LYP/6-311++G(d,p)**

Cluster	$\Delta H_{calc}^\circ$ (kJ·mol <sup>-1</sup> )	$\Delta S_{calc}^\circ$ (J·K <sup>-1</sup> ·mol <sup>-1</sup> )	$\Delta G_{298,calc}^\circ$ <sup>†</sup> (kJ·mol <sup>-1</sup> )	Structure (Figure 5.7)
<i>H</i> <sub>2</sub> O ··· [Gly – H] <sup>-</sup>	-61.0	-105.4	-29.6	<b>I</b>
	-61.1	-116.0	-26.6	<b>II</b>
<i>CH</i> <sub>3</sub> <i>OH</i> ··· [Gly – H] <sup>-</sup>	-66.1	-105.3	-34.7	<b>III</b>
	-71.4	-123.4	-34.6	<b>IV</b>
	-65.7	-121.5	-29.5	<b>V</b>
<i>C</i> <sub>2</sub> <i>H</i> <sub>5</sub> <i>OH</i> ··· [Gly – H] <sup>-</sup>	-75.5	-128.1	-37.4	<b>VI</b>
	-75.5	-130.3	-36.6	<b>VII</b>
	-74.4	-127.0	-36.6	<b>VIII</b>
	-70.1	-115.8	-35.5	<b>IX</b>
	-69.7	-126.1	-32.1	<b>X</b>

<sup>†</sup>  $\Delta G_T^\circ = \Delta H^\circ - T\Delta S^\circ$

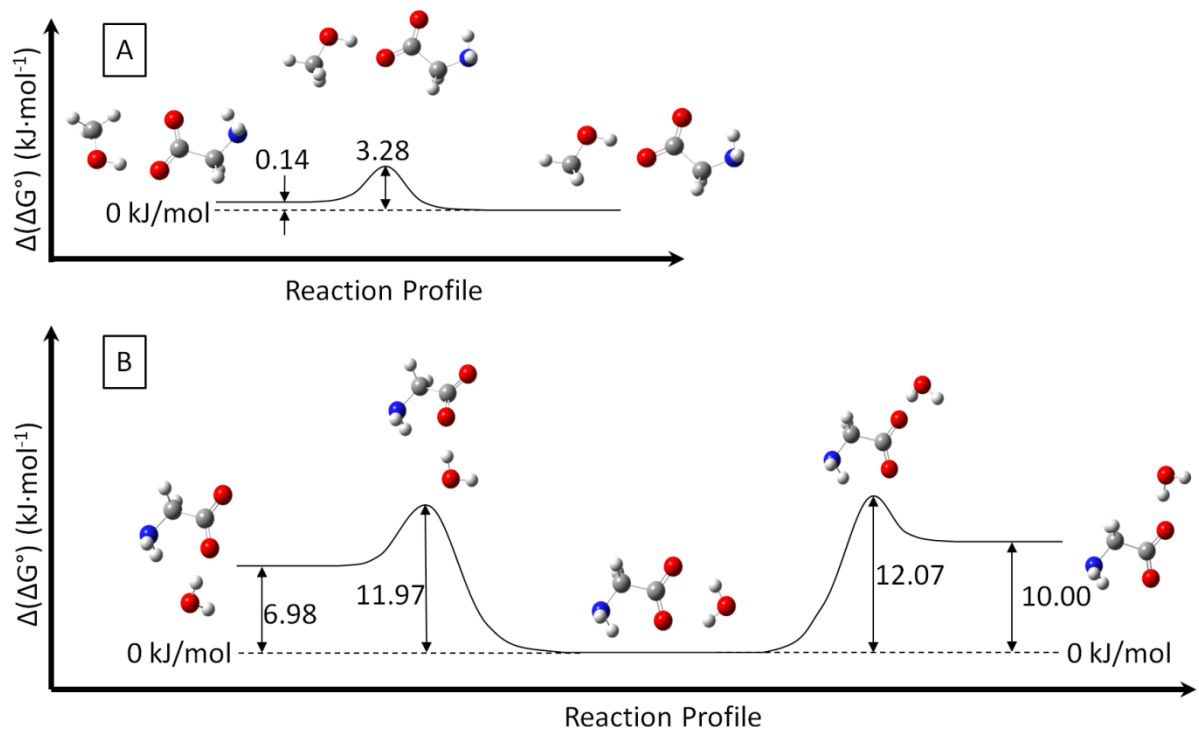


**Figure 5.8: Potential energy profiles for the A) rotational transformation from 4IV to 4III and B) translational transformation from 3I to both 4I and 4II, at 298K. All optimized structures and transition states were calculated via MP2(full)/6-311++G(d,p) // B3LYP/6-311++G(d,p).**

clustering of deprotonated glycine with water, methanol and ethanol have been plotted in Figure 5.9, at each of their respective maximum and minimum experimental temperatures. The isomer number reported along the abscissa correlates to the isomer's ranking in terms of free energy of formation at 298 K,  $\Delta G_{298,calc}^\circ$ , from lowest to highest (most stable to least stable).

In the cases of water and ethanol clustering to deprotonated glycine, Figure 5.9A and Figure 5.9C, it is evident that very little shift in the isomeric distribution takes place over the experimental temperature range. In both of these cases, the most stable isomer found at 298 K remained as the most stable isomer over the course of the experiment, while the additional stable isomers reported maintain a nearly constant relative abundance. The same cannot be said of the clustering of methanol with deprotonated glycine, Figure 5.9B, where notable shifts in the distribution are observed. Due to an increased entropic advantage, structure **5.7III** was predicted to become the most stable isomer within the experimental temperature range. This is in contrast to the case at 298 K, where, at this lower temperature, entropic contributions to free energy were less important and, hence, **5.6II** is predicted to be the most abundant. Also, large shifts in the relative abundance of the significantly populated isomers, as much as by 20%, were observed over the temperature range used in the experiments.

In all cases, since no single isomer was predicted to define the composition of the gaseous mixture, the measured thermochemical properties of the clustering systems will not necessarily be in agreement with those calculated for any one particular isomer, even when shifts in the isomeric distribution are not observed. Using Eq. 5.10, along with the thermochemical properties calculated for structures **5.6I-III** and **5.7I-X**, a plot of  $\mathcal{K}_{exp}$

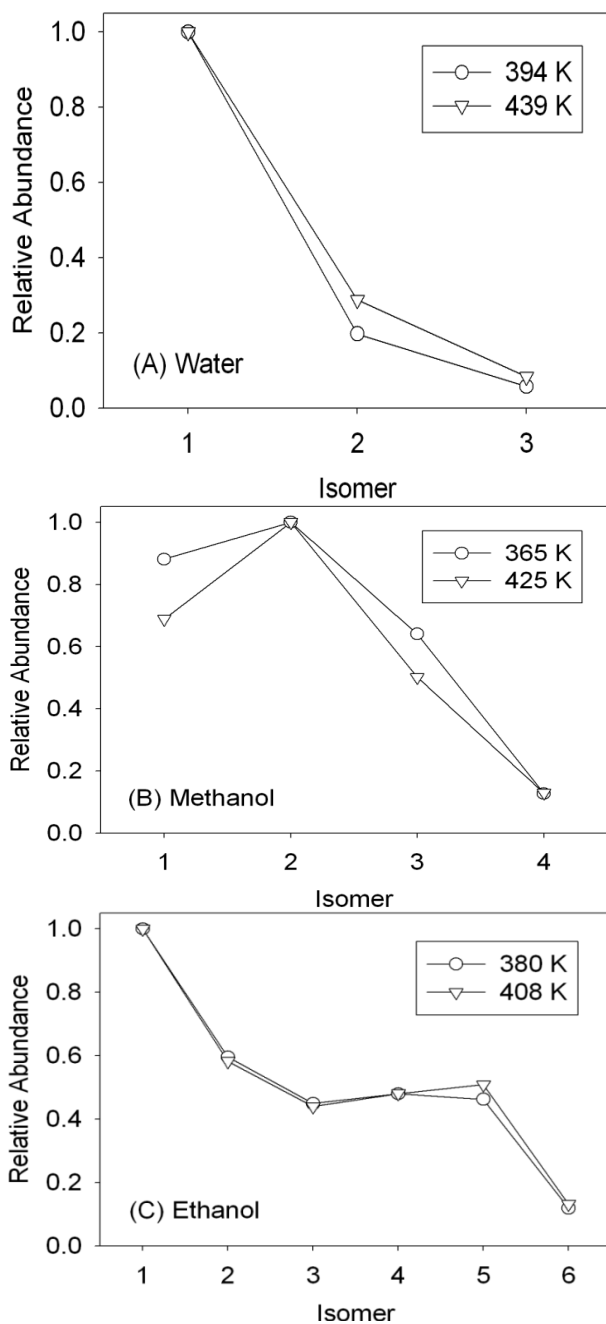


**Figure 5.9: Relative isomer distribution for A) water, B) methanol and C) ethanol clustered to deprotonated glycine at the maximum and minimum experimental temperatures. The isomer number refers to an isomers rank from lowest  $\Delta G_{298,calc}^\circ$ , (1), to highest within each clustering system.**

versus  $T^{-1}$  was calculated for each ROH system over the same temperature range used in the respective experiment. From these calculated plots, least squares fits were made. The slope and intercept of the resulting lines of best fit were used to obtain values of the enthalpy and entropy changes (in a manner similar to that used for the experimentally obtained values) and can be found in Table 5-2.

When the measured thermochemical values are compared to those calculated for a mixture of isomers, excellent agreement is observed for the three thermochemical properties of interest. In the best case a comparison of the values is within  $0.4 \text{ kJ}\cdot\text{mol}^{-1}$  for the enthalpy change,  $0.5 \text{ J}\cdot\text{K}^{-1}\cdot\text{mol}^{-1}$  for the entropy change and  $0.1 \text{ kJ}\cdot\text{mol}^{-1}$  for the free energy change. In the worst case the comparison is within  $2.2 \text{ kJ}\cdot\text{mol}^{-1}$  for the enthalpy change,  $1.1 \text{ J}\cdot\text{K}^{-1}\cdot\text{mol}^{-1}$  for the entropy change and  $2.4 \text{ kJ}\cdot\text{mol}^{-1}$  for the free energy change. The average deviation between measured and calculated values of  $\Delta H^\circ$ ,  $\Delta S^\circ$  and  $\Delta G_{298}^\circ$  for all three solvents was improved to  $1.6 \text{ kJ}\cdot\text{mol}^{-1}$ ,  $0.8 \text{ J}\cdot\text{K}^{-1}\cdot\text{mol}^{-1}$  and  $1.5 \text{ kJ}\cdot\text{mol}^{-1}$ . When the measured thermochemical values were compared to those calculated for the most stable isomers at 298K, **5.6I-III**, excellent agreement could still be observed for the change in enthalpy and Gibbs free energy, but a significant discrepancy can be noted for the change in entropy values. This discrepancy is evidently attributable to the presence of the isomers shown in Figure 5.7, which possess similar thermochemical properties to that of the most stable isomers of Figure 5.6. If the isomers were assumed to have equal thermochemical properties, the discrepancy between the measured entropy change and the value calculated for the lowest energy structure would be solely attributed to  $R\ln N$ , and an estimate of  $N$  could be obtained. Such an analysis has been performed and the results are reported in Table 5-4. Since the

**Table 5-4: Estimate of the number of isomers of the cluster ion,  $N$ , compared to the number found to be feasible from electronic structure calculations,  $N_{observed}$ .  $\Delta S^\circ$  values are reported in  $\text{J}\cdot\text{K}^{-1}\cdot\text{mol}^{-1}$**

Cluster	$\Delta S_{obs}^\circ$	$\Delta S_{calc}^\circ$ <sup>*</sup>	$\Delta S_{obs}^\circ - \Delta S_{calc}^\circ$	$N = e^{\frac{\Delta S_{obs}^\circ - \Delta S_{calc}^\circ}{R}}$	$N_{observed}$ <sup>†</sup>
$H_2O \cdots [Gly - H]^-$	-112.7	-122.7	10	3	3
$CH_3OH \cdots [Gly - H]^-$	-105.5	-120.9	15.4	6	4
$C_2H_5OH \cdots [Gly - H]^-$	-109.0	-121.0	12	4	6

\* – calculated for global minimum structures **3I-III**

† – refers to the number of isomers that were found in which ROH forms a strong hydrogen bond to the carboxylate group (i.e. those isomers present in significant amounts)

isomers do not have identical thermochemical properties, it is no surprise that the deviation of the entropy term does not exactly equal the factor of  $R\ln N$  as predicted above. Nonetheless, in the worst case, the number of isomers predicted is within 2 of the number found to be feasible, based on the computational results described above.

### 5.3.2 Clustering of Deprotonated Alanine, Valine and Serine with ROH

Exploratory geometry optimizations performed indicated that a large number of thermochemically and kinetically accessible isomers will also exist for clusters of deprotonated alanine, valine and serine and ROH. Due to the generally good agreement between comparisons of HPMS values to that of the most stable isomer demonstrated in the deprotonated glycine clustering systems, as well as the cumbersome nature of manually locating all accessible isomers for a clustering system, only the most stable clusters associated with ROH clustering to the carboxylate and amine moieties of alanine, valine and serine were sought after. The optimized geometries for these structures are given in Figure 5.10 - Figure 5.12. The thermochemical properties associated with the formation of these cluster ions are found in Table 5-5 - Table 5-7. As in the case presented for deprotonated glycine, a comparison of  $\Delta H^\circ$ ,  $\Delta S^\circ$  and  $\Delta G_{298}^\circ$  from HPMS experiments to those obtained from calculations provides a wealth of information on the nature of these clustering systems.

In general, the values of  $\Delta H^\circ$  and  $\Delta G_{298}^\circ$  calculated for the most stable isomers were in good agreement to those obtained from experiment. Large discrepancies between the experimental and calculated values of  $\Delta S^\circ$  were observed, just as in the deprotonated glycine

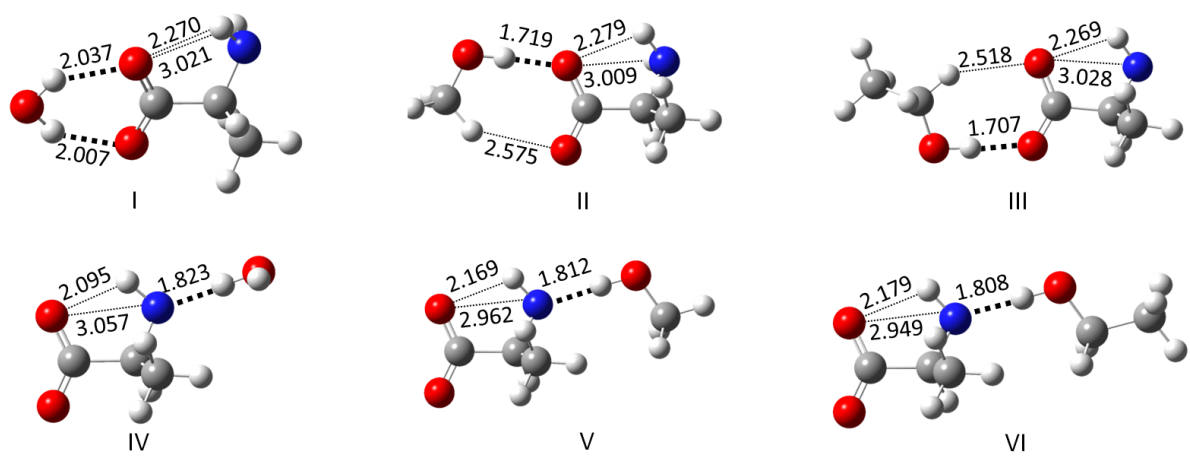


**Figure 5.10:** Lowest energy structures obtained using MP2(full)/6-311++G(d,p) // B3LYP/6-311++G(d,p), for the attachment of ROH to the carboxylate or amine moiety of  $NH_2CH(CH_3)COO^-$ . Distances are in units of angstroms.

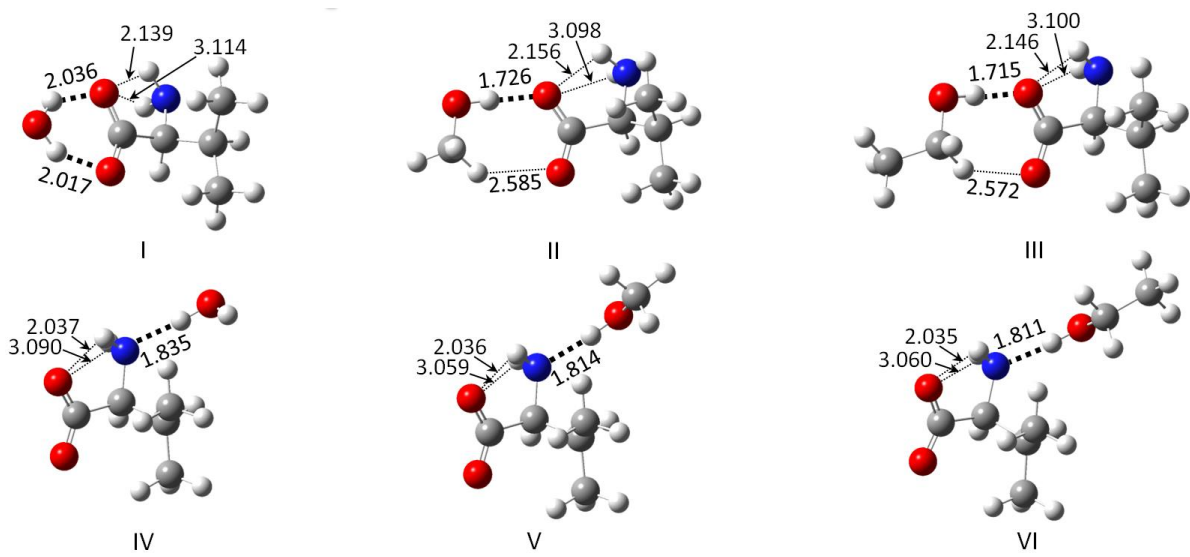


**Figure 5.11: Lowest energy structures obtained using MP2(full)/6-311++G(d,p) // B3LYP/6-311++G(d,p), for the attachment of ROH to the carboxylate or amine moiety of  $NH_2CH(CH(CH_3)_2)COO^-$ . Distances are in units of angstroms.**

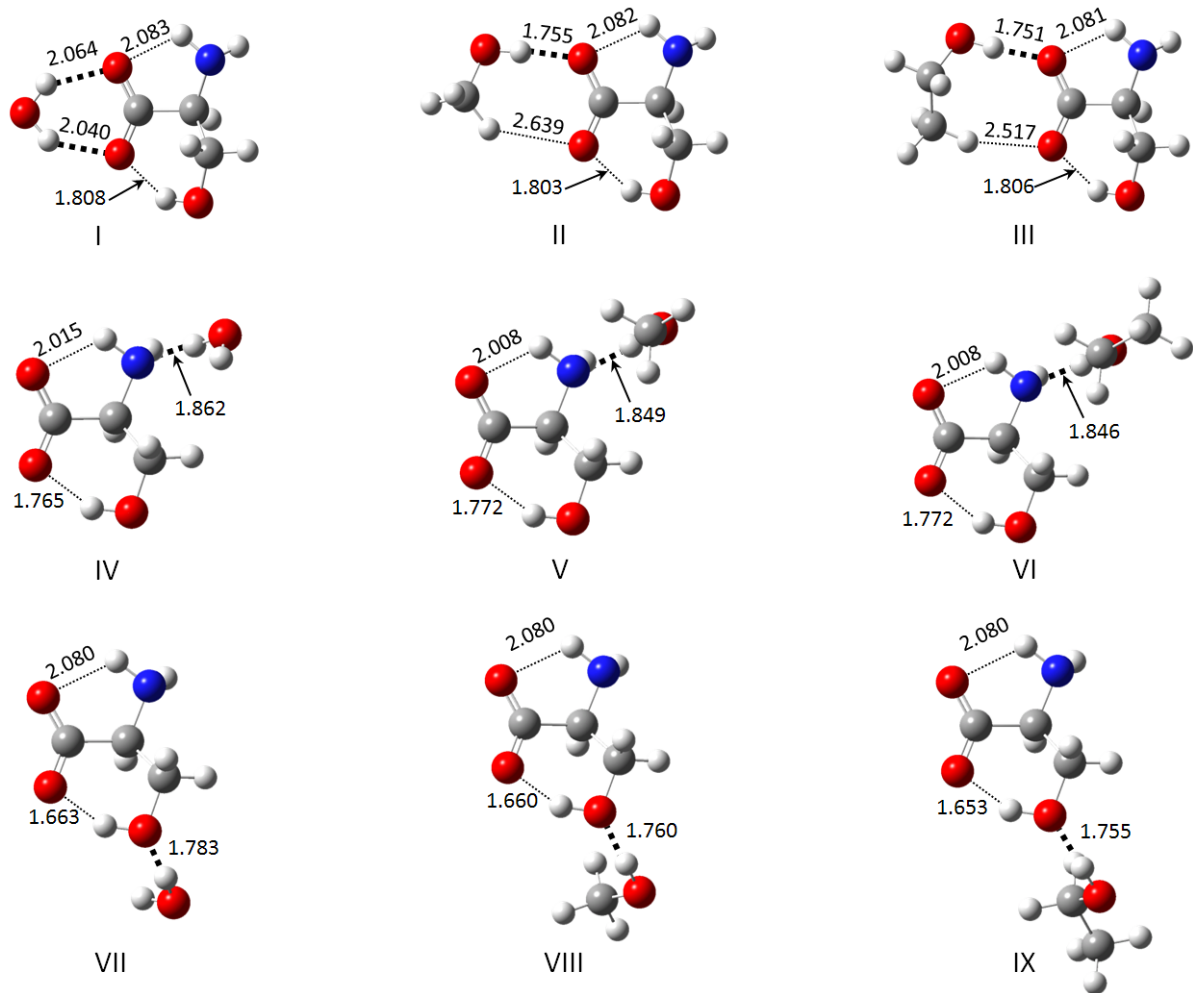


**Figure 5.12: Lowest energy structures obtained using MP2(full)/6-311++G(d,p) // B3LYP/6-311++G(d,p), for the attachment of ROH to the carboxylate or amine moiety of  $\text{NH}_2\text{CH}(\text{CH}_2\text{OH})\text{COO}^-$ . Distances are in units of angstroms.**

**Table 5-5: Measured and Calculated Thermochemical Properties for the Formation of ROH ··· [Ala – H]<sup>-</sup>, R = H, CH<sub>3</sub>, C<sub>2</sub>H<sub>5</sub>**

Cluster [M – H] <sup>-</sup>	ROH	$\Delta H_{calc}^\circ$ (kJ·mol <sup>-1</sup> )	$\Delta S_{calc}^\circ$ (J·K <sup>-1</sup> ·mol <sup>-1</sup> )	$\Delta G_{298,calc}^\circ$ <sup>†</sup> (kJ·mol <sup>-1</sup> )	Structure (Figure 5.10)
[Ala – H] <sup>-</sup>	H <sub>2</sub> O	-69.1	-107.0	-37.2	<b>HPMS</b>
		-72.5	-122.9	-35.9	<b>I</b>
		-53.6	-114.0	-19.6	<b>IV</b>
CH <sub>3</sub> OH		-69.9	-101.5	-39.6	<b>HPMS</b>
		-71.9	-122.0	-35.5	<b>II</b>
		-57.4	-119.3	-21.8	<b>V</b>
C <sub>2</sub> H <sub>5</sub> OH		-68.6	-95.3	-40.2	<b>HPMS</b>
		-73.9	-118.6	-38.5	<b>III</b>
		-57.4	-123.1	-20.7	<b>VI</b>

<sup>†</sup>  $\Delta G_T^\circ = \Delta H^\circ - T\Delta S^\circ$

**Table 5-6: Measured and Calculated Thermochemical Properties for the Formation of ROH ··· [Val – H]<sup>-</sup>, R = H, CH<sub>3</sub>, C<sub>2</sub>H<sub>5</sub>**

Cluster [M – H] <sup>-</sup>	ROH	$\Delta H_{calc}^\circ$ (kJ·mol <sup>-1</sup> )	$\Delta S_{calc}^\circ$ (J·K <sup>-1</sup> ·mol <sup>-1</sup> )	$\Delta G_{298,calc}^\circ$ <sup>†</sup> (kJ·mol <sup>-1</sup> )	Structure (Figure 5.11)
$[Val - H]^-$	H <sub>2</sub> O	-68.9	-103.3	-38.1	<b>HPMS</b>
		-71.1	-122.7	-34.5	<b>I</b>
		-54.2	-116.4	-19.5	<b>IV</b>
CH <sub>3</sub> OH		-68.3	-101.6	-38.0	<b>HPMS</b>
		-70.3	-122.7	-33.7	<b>II</b>
		-58.7	-123.7	-21.8	<b>V</b>
C <sub>2</sub> H <sub>5</sub> OH		-74.2	-111.9	-40.8	<b>HPMS</b>
		-72.0	-126.4	-34.4	<b>III</b>
		-59.0	-126.3	-21.3	<b>V</b>

<sup>†</sup>  $\Delta G_T^\circ = \Delta H^\circ - T\Delta S^\circ$

**Table 5-7: Measured and Calculated Thermochemical Properties for the Formation of ROH ··· [Ser – H]<sup>-</sup>, R = H, CH<sub>3</sub>, C<sub>2</sub>H<sub>5</sub>**

Cluster [M – H] <sup>-</sup>	ROH	$\Delta H_{calc}^\circ$ (kJ·mol <sup>-1</sup> )	$\Delta S_{calc}^\circ$ (J·K <sup>-1</sup> ·mol <sup>-1</sup> )	$\Delta G_{298,calc}^\circ$ <sup>†</sup> (kJ·mol <sup>-1</sup> )	Structure (Figure 5.12)
[Ser – H] <sup>-</sup>	H <sub>2</sub> O	-44.7	-58.6	-27.2	<b>HPMS</b>
		-64.8	-120.0	-29.0	<b>I</b>
		-49.4	-111.7	-16.1	<b>IV</b>
		-48.4	-108.9	-15.9	<b>VII</b>
CH <sub>3</sub> OH	CH <sub>3</sub> OH	-51.1	-73.4	-29.2	<b>HPMS</b>
		-64.1	-122.0	-27.7	<b>II</b>
		-53.9	-121.4	-17.7	<b>V</b>
		-52.3	-115.1	-18.0	<b>VIII</b>
C <sub>2</sub> H <sub>5</sub> OH	C <sub>2</sub> H <sub>5</sub> OH	-59.5	-90.1	-32.7	<b>HPMS</b>
		-66.2	-121.2	-30.0	<b>III</b>
		-53.6	-123.4	-16.9	<b>VI</b>
		-51.9	-114.1	-17.9	<b>IX</b>

<sup>†</sup>  $\Delta G_T^\circ = \Delta H^\circ - T\Delta S^\circ$

systems. The thermochemical properties for the clustering of deprotonated alanine to ROH are reported in Table 5-5. As observed for  $[\text{Gly-H}]\cdots\text{ROH}$ , it is clear that the measured thermochemical properties for this system best agree to the calculated values corresponding to ROH attachment to the carboxylate site. The average deviation between measured and calculated values of  $\Delta H^\circ$ ,  $\Delta S^\circ$  and  $\Delta G_{298}^\circ$  for all three solvents are  $3.6 \text{ kJ}\cdot\text{mol}^{-1}$ ,  $19.9 \text{ J}\cdot\text{K}^{-1}\cdot\text{mol}^{-1}$  and  $2.3 \text{ kJ}\cdot\text{mol}^{-1}$ . Similar observations can be made for the clustering of deprotonated valine to ROH, Table 5-6, where ROH is observed to prefer attachment to the carboxylate moiety, and the average deviation between measured and calculated values of  $\Delta H^\circ$ ,  $\Delta S^\circ$  and  $\Delta G_{298}^\circ$  for all three solvents are  $2.1 \text{ kJ}\cdot\text{mol}^{-1}$ ,  $18.3 \text{ J}\cdot\text{K}^{-1}\cdot\text{mol}^{-1}$  and  $4.8 \text{ kJ}\cdot\text{mol}^{-1}$ .

Inspection of the values obtained for the clustering of deprotonated serine to ROH, Table 5-7, show much larger discrepancies between measured and calculated values of  $\Delta H^\circ$  and  $\Delta S^\circ$ , and due to cancelation of error, good agreement for  $\Delta G_{298}^\circ$ . The average deviation between measured and calculated values of  $\Delta H^\circ$ ,  $\Delta S^\circ$  and  $\Delta G_{298}^\circ$  for all three solvents are  $13.3 \text{ kJ}\cdot\text{mol}^{-1}$ ,  $47.0 \text{ J}\cdot\text{K}^{-1}\cdot\text{mol}^{-1}$  and  $2.0 \text{ kJ}\cdot\text{mol}^{-1}$ . This large discrepancy in the change in enthalpy and entropy terms could indicate that the most stable isomer assumed by the  $[\text{Ser-H}]\cdots\text{ROH}$  cluster is unlike those observed in the others. This larger error could also be an indication that the additional intramolecular hydrogen bond found in the deprotonated serine structure may create too complex of a hydrogen bonding network for this level of theory to describe. It could also possibly indicate error in the experimental data. It is clear that further investigation of this clustering system is needed to shed light into this discrepancy.

### 5.3.3 Thermochemical Trends

The measured and calculated values of Gibbs free energy have been plotted as a function of the gas phase acidity of ROH at 298K, Figure 5.13 -Figure 5.16. It is interesting to note that the expected correlation of Gibbs free energy for the binding of deprotonated glycine to the solvent molecule with gas phase acid strength is not observed. While a small decrease in free energy for the clustering reaction is observed as the solvent is varied from ethanol to methanol, as a consequence of the decreasing gas-phase acid strength of the solvent, no further significant decrease is observed in proceeding from methanol to water. This is in contrast to the experimental observations described above for the clustering of acetate to the same solvent molecules, where a decrease in binding enthalpy with decreasing solvent acid strength was observed. An examination of the optimized geometries of these deprotonated amino acids-solvent clusters provides additional insight into this discrepancy. In the methanol and ethanol systems, the ion and solvent molecule interact through a strong OH…O hydrogen bond, and in some cases, through an additional CH…O interaction. Upon closer inspection of the water system, it is seen that the lowest energy cluster, **5.6I**, which is significantly lower in energy than the next most stable isomer, is composed of two relatively weaker OH…O hydrogen bonds. That is, it possesses a cyclic structure similar to that which was calculated and reported in the literature<sup>122</sup> for the clustering of water and acetate. The two weaker OH…O bonds observed in the deprotonated glycine – water clusters combine to give a stronger than expected interaction, and hence, a measured  $\Delta G_{298}^\circ$  that is comparable to the value observed for clusters involving the stronger gas-phase acid methanol. A similar

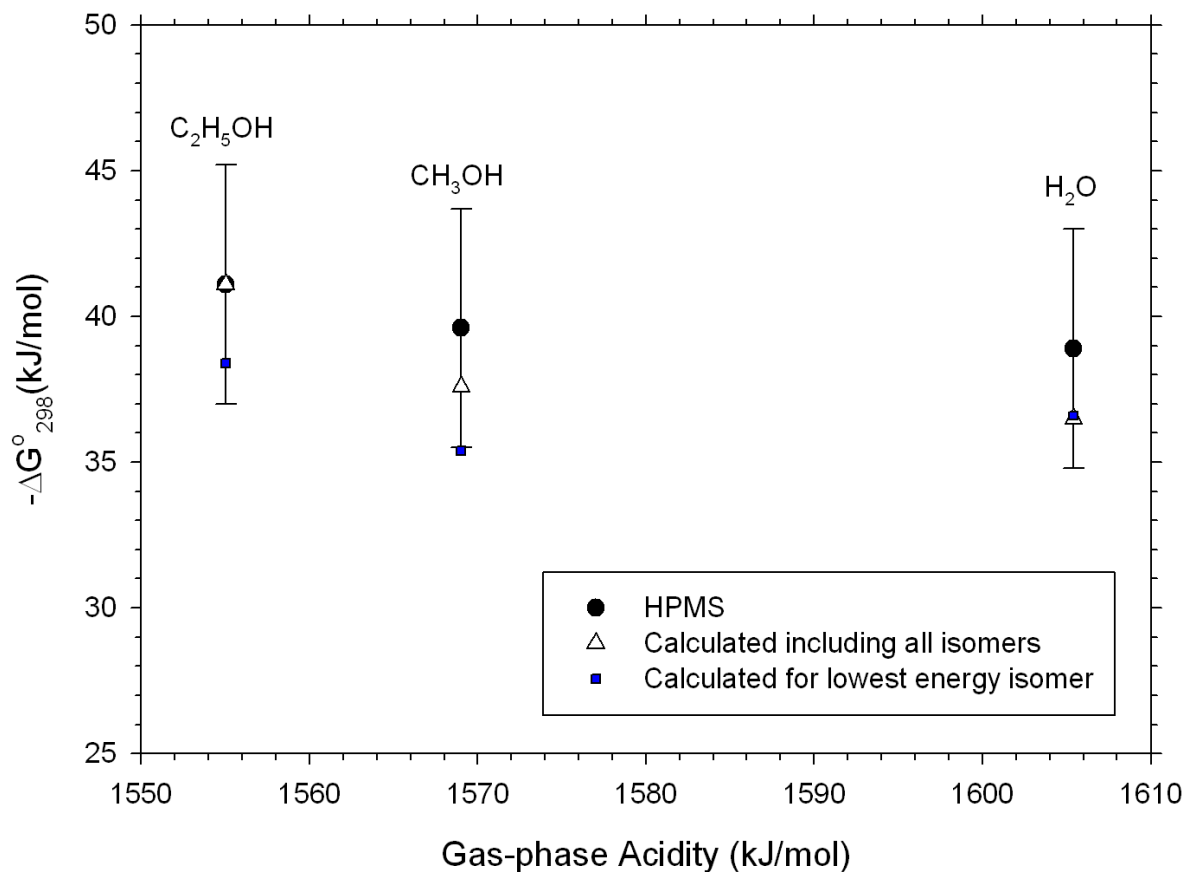


**Figure 5.13: Negative free energy change (298 K) as a function of the gas-phase acidity of solvent molecule, for the formation of clusters of deprotonated glycine with ROH.**

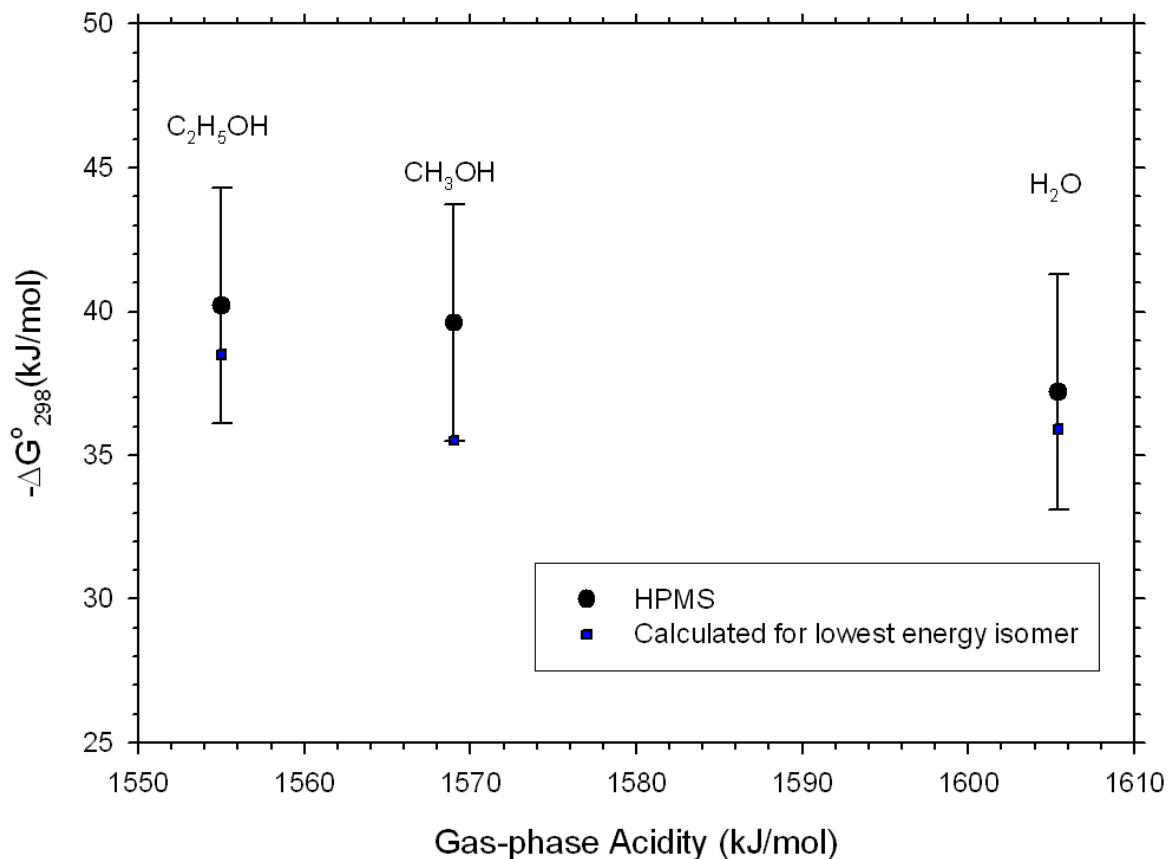


**Figure 5.14:** Negative free energy change (298 K) as a function of the gas-phase acidity of solvent molecule, for the formation of clusters of deprotonated alanine with ROH.

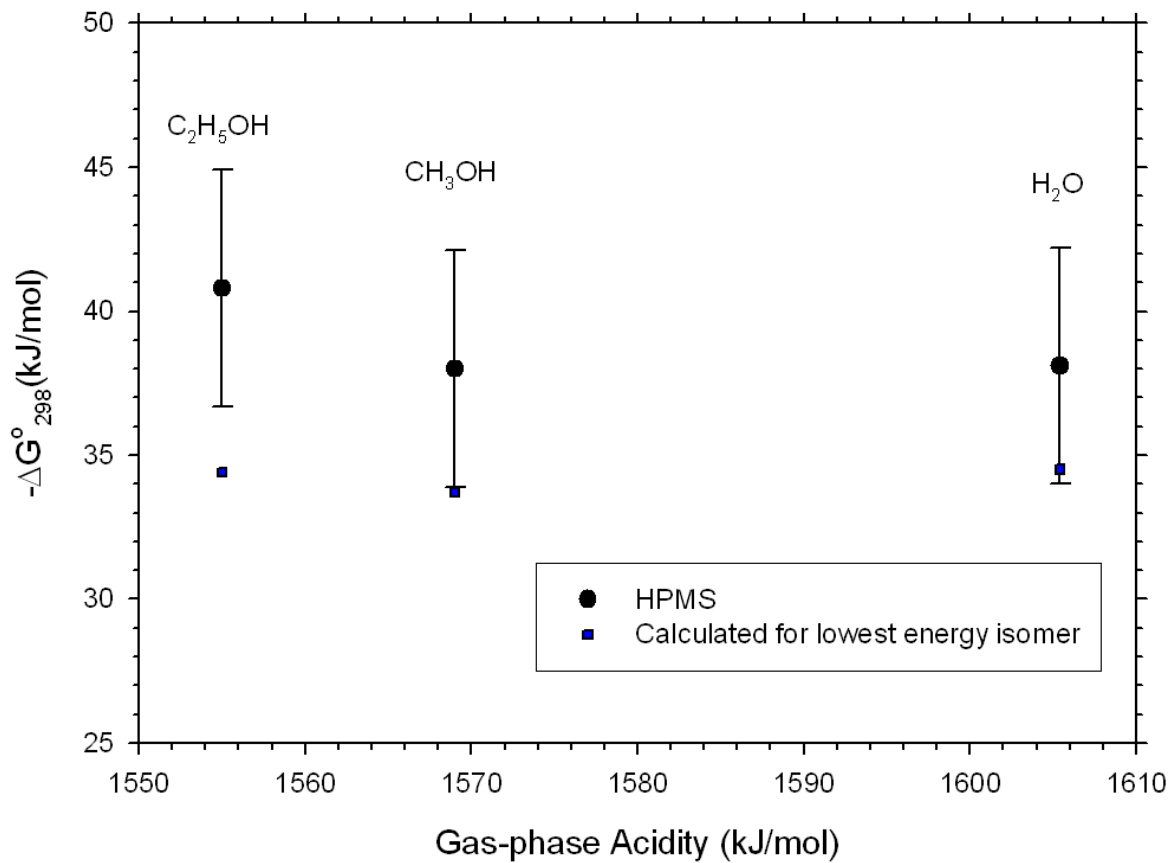


**Figure 5.15:** Negative free energy change (298 K) as a function of the gas-phase acidity of solvent molecule, for the formation of clusters of deprotonated valine with ROH.

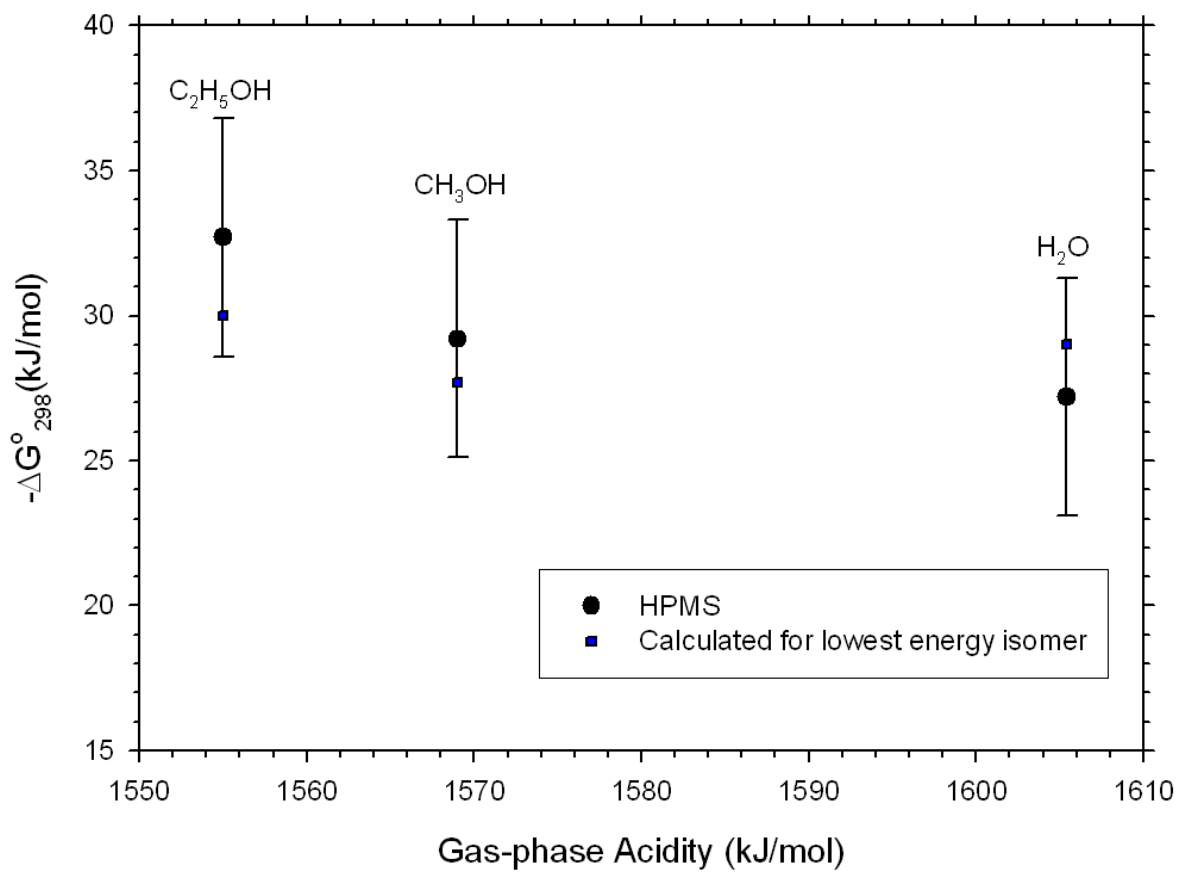


**Figure 5.16:** Negative free energy change (298 K) as a function of the gas-phase acidity of solvent molecule, for the formation of clusters of deprotonated serine with ROH.

trend would be expected for the clustering of acetate with water, methanol and ethanol, but, as noted earlier, this is not observed in the experimental values reported in the literature.

In order to gain insight into the discrepancy between the experimentally observed trends for the clustering of deprotonated glycine and acetate with ROH, the thermochemical properties for clusters of acetate with ROH were calculated. The optimized structures for the most stable isomers of each acetate-ROH cluster are shown in Figure 5.17, while the calculated thermochemical properties are reported in Table 5-8. It can be noted that for the clustering of acetate with water, the value determined here agrees to a high degree of accuracy with that calculated by Markham, *et al.* Moreover, the free energy for the formation of acetate-ROH clusters at 298 K effectively does not change as the gas-phase acid strength of the solvent is increased. These findings are consistent with the observed relationship between free energy and gas-phase acidity of solvent for the clustering of deprotonated glycine, alanine, valine and serine with ROH, indicating that it is likely that the experimentally obtained thermochemical values for the clustering of acetate with ROH reported in the literature may be flawed.

It can be also noted that the measured enthalpies and free energies of interaction in this study are less exothermic and exergonic than the analogous values calculated for the acetate-solvent clusters. As indicated previously, a comparison to acetic acid shows that the lower acidity of the amino acids, combined with the presence of the intramolecular hydrogen bonds in the deprotonated amino acids (which act to decrease the basicity of the carboxylate), results in weaker intermolecular hydrogen bonds.

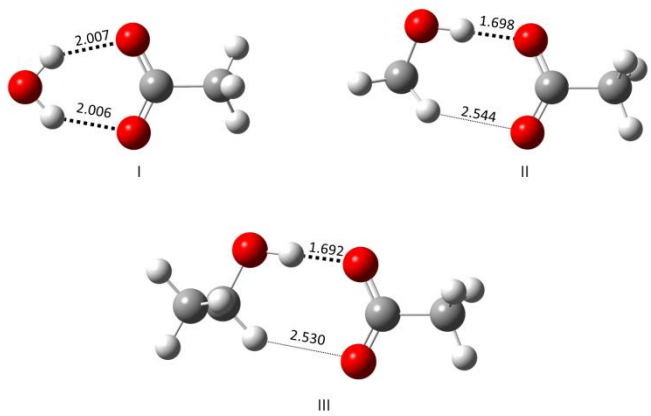


**Figure 5.17: Lowest energy structures obtained using MP2(full)/6-311++G(d,p) // B3LYP/6-311++G(d,p), for the attachment of ROH to CH<sub>3</sub>COO<sup>-</sup>. Distances are in units of angstroms.**

**Table 5-8: Thermochemical Properties for the Clustering of Acetate with ROH, R = H,  
CH<sub>3</sub>, C<sub>2</sub>H<sub>5</sub>**

Cluster	$\Delta H_{calc}^\circ$ (kJ·mol <sup>-1</sup> )	$\Delta S_{calc}^\circ$ (J·K <sup>-1</sup> ·mol <sup>-1</sup> )	$\Delta G_{298,calc}^\circ$ (kJ·mol <sup>-1</sup> )	Structure (Figure 5.17)
$H_2O \cdots [CH_3COO]^-$	-74.7 <sup>a</sup>	-101.4	-44.5	<b>I</b>
	-68.6 <sup>b</sup>			
	-74.9 <sup>c</sup>			
$CH_3OH \cdots [CH_3COO]^-$	-74.3 <sup>a</sup>	-100.0	-44.5	<b>II</b>
	-73.6 <sup>d</sup>			
$C_2H_5OH \cdots [CH_3COO]^-$	-76.3 <sup>a</sup>	-105.6	-44.8	<b>III</b>
	-86.6 <sup>e</sup>			

a – this work, MP2(full)/6-311++G(d,p)//B3LYP/6-311++G(d,p)

b – experimental value, ref [10]

c – calculated value, ref[13]

d – experimental value, ref [11]

e – experimental value, ref [12]

Several other important observations can be made from a closer inspection of the thermochemical values. From the thorough examination of the clustering system of ROH with deprotonated glycine, it can be noted that as the number of isomers present in a clustering system increases, the importance of including all isomers in an attempt to model the thermochemical properties of the system increases. This is seen in Figure 5.13 as a general increase in the accuracy of the calculated value, as well as an increase in the difference between the values obtained from the two calculation methods, as the complexity (i.e. the possible number of isomers) of the clustering system was increased. Another observation can be made from the deprotonated glycine system. Since both values of the calculated  $\Delta G_{298}^\circ$  generally fell within the error limits of the experimental value, it may appear at first glance that there is no added benefit to the rigorous modeling of the thermochemical properties from the HPMS experiments. In fact, a closer inspection of the values of  $\Delta H_{calc}^\circ$  and  $\Delta S_{calc}^\circ$  show that it is a convenient cancellation of errors in these values that leads to the observed high level of accuracy between the measured value of  $\Delta G_{298}^\circ$  and that obtained for the single lowest isomer. Specifically, the enthalpy and entropy changes calculated for the single lowest isomers were typically lower than the measured values, and when combined to calculate  $\Delta G_{298}^\circ$  the error in these two competing terms cancels out. This is in contrast to the case when all isomers are included in the calculations, where consistent accuracy between measured and calculated values for all three thermochemical properties could be observed. This cancellation of error is observed to take place in the other deprotonated amino acid clustering systems as well. The most extreme example of this cancellation of error occurs for the clustering of deprotonated serine with

water. Here the values of  $\Delta H_{calc}^\circ$  and  $\Delta S_{calc}^\circ$  were determined to disagree by 20.1 kJ·mol<sup>-1</sup> and 61.4 J·K<sup>-1</sup>·mol<sup>-1</sup>, yet the measured value of  $\Delta G_{298}^\circ$  only disagreed with the calculated value by a mere 1.8 kJ·mol<sup>-1</sup>.

The final thermochemical trend observed is the relationship between the free energy for the clustering of ROH to the deprotonated amino acids at 298 K and the enthalpy of deprotonation of each amino acid. A plot of the experimentally derived value of  $-\Delta G_{298}^\circ$  obtained for each ROH...[M-H]<sup>-</sup> system as function of the enthalpy of deprotonation of M (M = Gly, Ala, Val, Ser) is given in Figure 5.18. It can be noted that, for a given solvent, as the acid strength of the amino acid it is clustering to decreases (the basicity of its conjugate base increases) an increase in the negative free energy of clustering occurs. Clusters involving water and ethanol follow this trend in a near ideal manner, while a slight scatter in the data points is observed for the clustering of methanol. Despite this scatter, the overall trend of direct proportionality between  $-\Delta G_{298}^\circ$  and the enthalpy of deprotonation is still observed. As noted in the isomeric analysis of deprotonated glycine, calculations show that methanol-solvated deprotonated amino acid clusters are predicted to undergo a large shift in its isomeric distribution over the experimental temperature range. Moreover, the most stable isomer predicted at 298 K was predicted to become the second most stable isomer in the experimental temperature range. For this reason, using the enthalpy and entropy change values collected between 365 K and 425 K to extrapolate a value of the free energy change at 298 K may not be the most appropriate. This shift in the isomer distribution could be one reason for the increased scatter observed, but it should be pointed out that this scatter is well within the experimental error of  $\pm 4.1$  kJ·mol<sup>-1</sup> for the change in free energy.

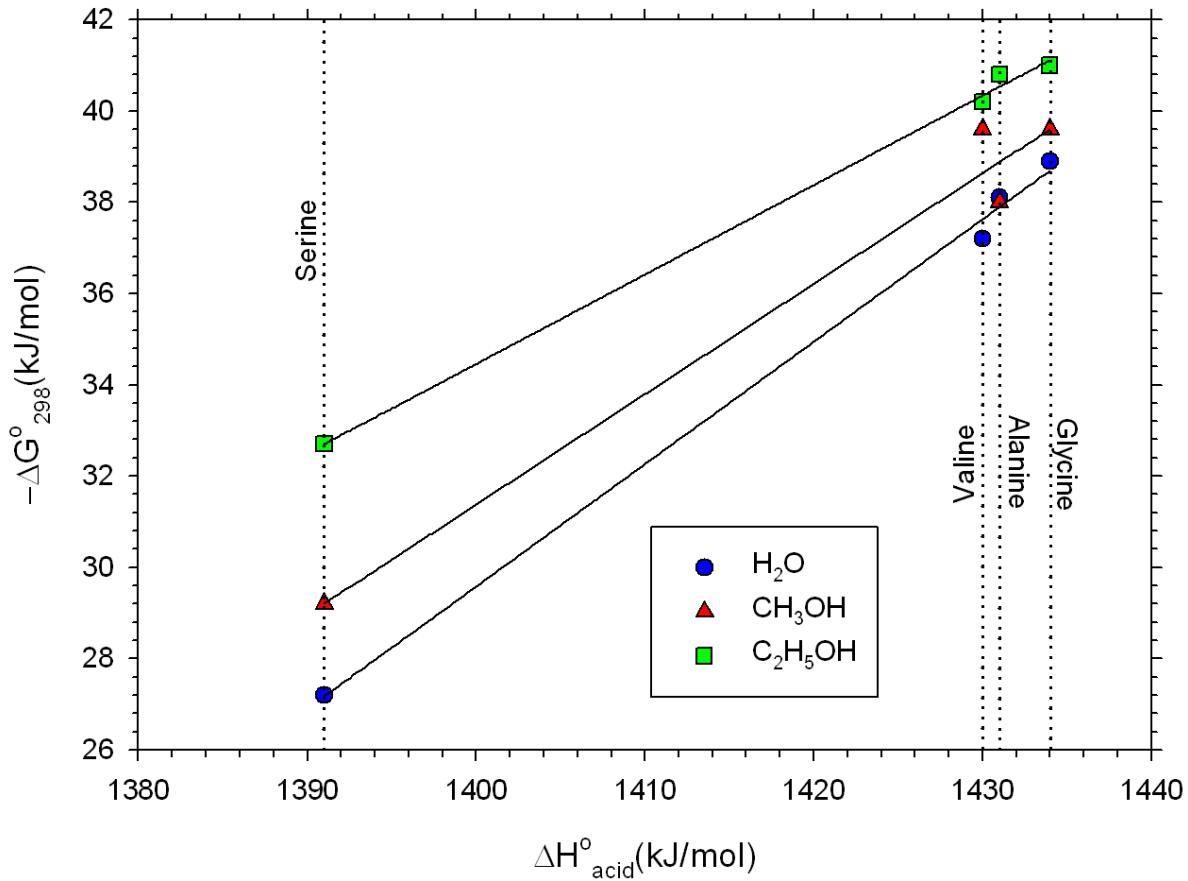


**Figure 5.18:** Negative ergonicity associated with the formation of  $\text{ROH}\cdots[\text{M}-\text{H}]^-$  clusters at 298 K plotted as a function of the enthalpy of deprotonation ( $\text{M} = \text{Gly, Ala, Val, Ser}$ ).

### 5.3.4 Simulated IR Spectra for Deprotonated Glycine Clustered with ROH

Using the vibrational frequencies and intensities calculated at the B3LYP/6-311++G(d,p) level of theory, the line spectrum for each of the isomers shown in Figure 5.6 and Figure 5.7 was obtained. Each of the lines in each spectrum was fitted with a Lorentzian line-shape function (full width at half maximum of  $50\text{ cm}^{-1}$ ), which were then summed to obtain a simulated IR spectrum for each isomer. The IR spectrum for a distribution of isomers at 298 K was also obtained by scaling the intensity of the individual isomer IR spectra according to the respective isomeric relative abundance (at 298 K), and then summing them together. The simulated IR spectrum for each isomer, as well as for a distribution of isomers of the deprotonated glycine – ROH cluster, can be found in Figure 5.19 - Figure 5.21. An analysis of each spectrum calculated for the distribution of isomers provides insight into features which could be used to identify the presence of particular isomers.

The IR spectra shown in Figure 5.19 correspond to the individual isomers, as well the distribution of isomers at 298 K, of deprotonated glycine clustered to water. It is noted that the spectrum simulated for the collection of all isomers closely resembles that of the most stable isomer, **5.6I**. The most intense absorptions for isomer **5.6I** occur at  $1634\text{ and }3655\text{ cm}^{-1}$ . The peak at  $1634\text{ cm}^{-1}$  corresponds to the asymmetric stretch of the carboxylate group and is common to all three isomers ( $1647\text{ cm}^{-1}$  for **5.7I** and  $1651\text{ cm}^{-1}$  for **5.7II**). On the other hand, the peak occurring at  $3655\text{ cm}^{-1}$ , corresponding to the symmetric stretch of both OH bonds in water, can be used to identify the presence of this isomer. Isomer **5.7I** and **5.7II** do possess a similar OH vibration, but the interaction between water and deprotonated glycine in

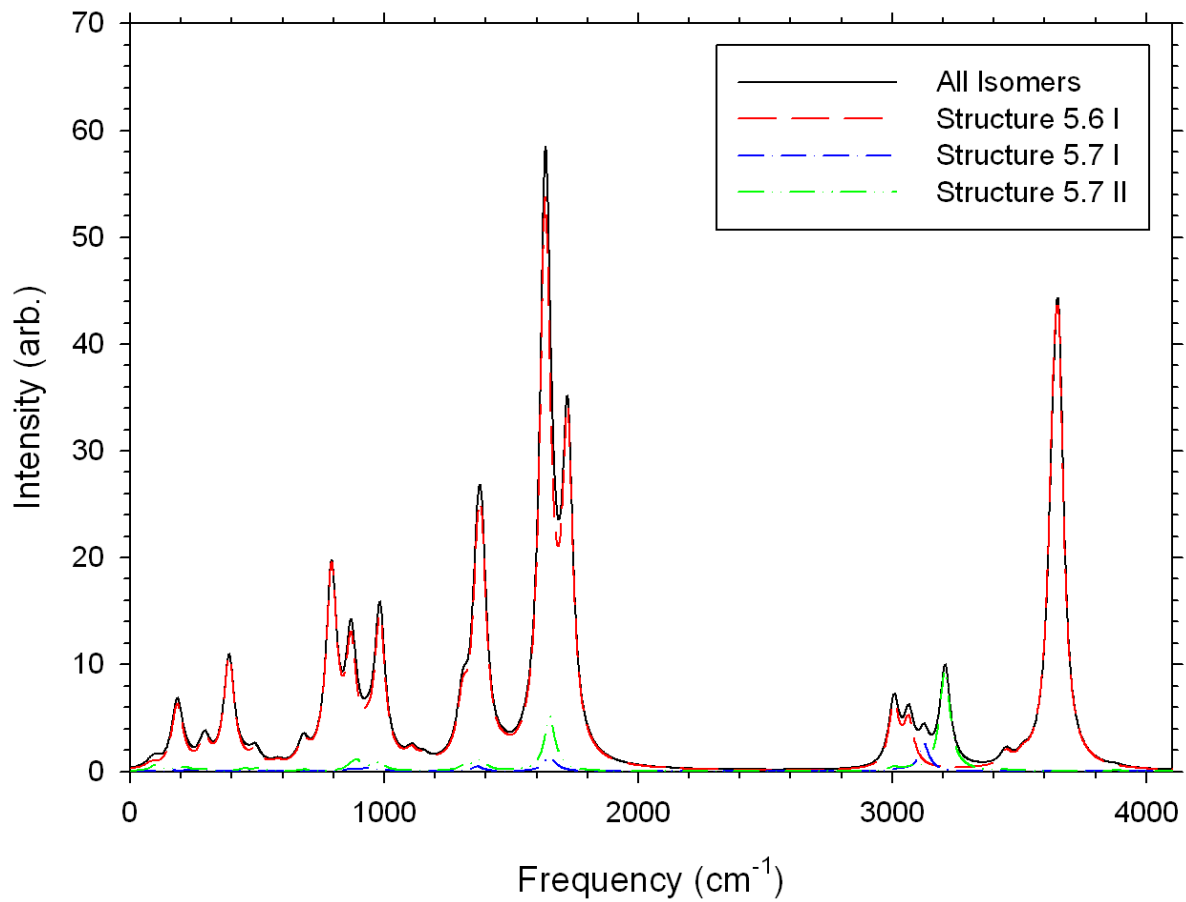


**Figure 5.19:** Simulated spectrum for a distribution of isomers at 298 K. Deprotonated glycine clustered with water.

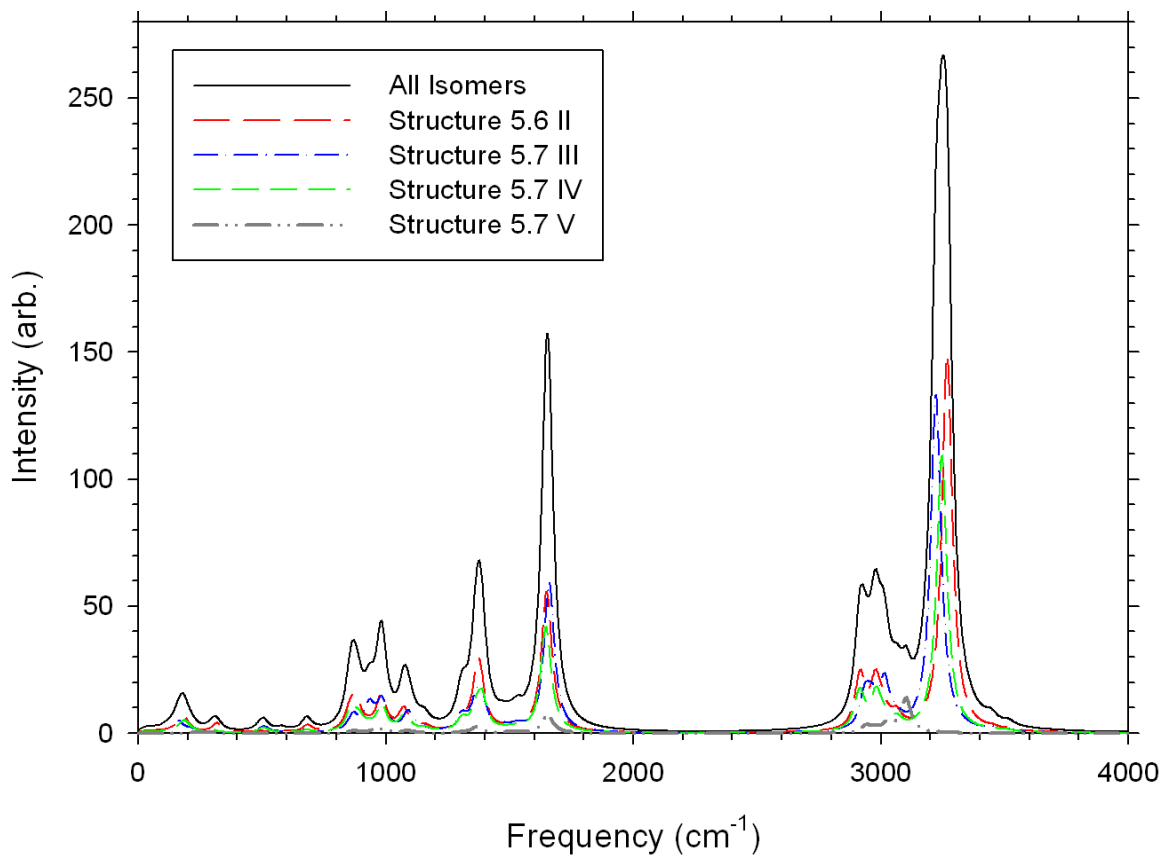


**Figure 5.20:** Simulated spectrum for a distribution of isomers at 298 K. Deprotonated glycine clustered with methanol.

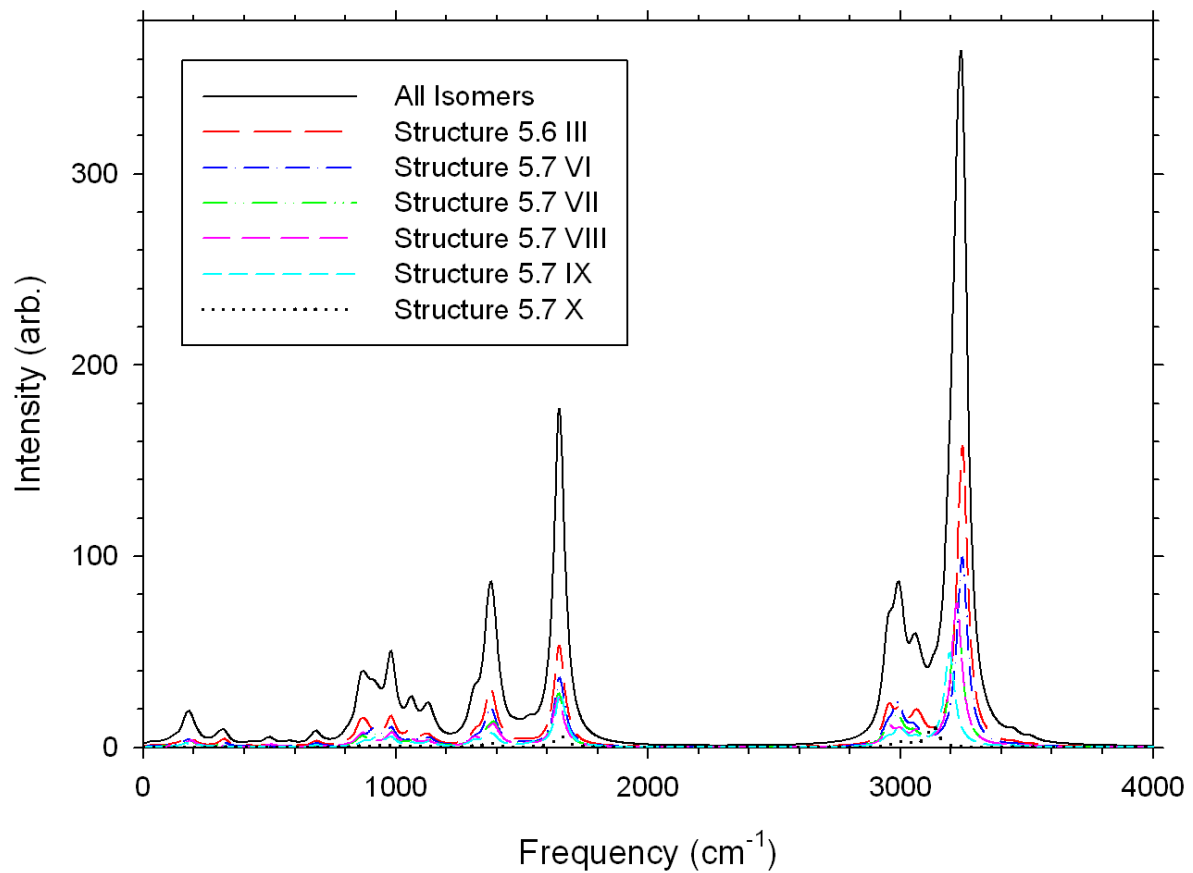


**Figure 5.21: Simulated spectrum for a distribution of isomers at 298 K. Deprotonated glycine clustered with ethanol.**

these structures is through a single OHO hydrogen bond. In the case of **5.7I** this vibration is red-shifted from that of structure **5.6I** to  $3125\text{ cm}^{-1}$  and in **5.7II** it is red-shifted from that of **5.6I** to  $3209\text{ cm}^{-1}$ . Since **5.7I** and **II** are predicted to possess small relative abundance, they do not contribute in any significant way to the overall IR spectrum. The vibrational lines corresponding to the OH vibrations in water are, however, distinguishable in the simulated spectra for the distribution of isomers, and could potentially be used to identify the presence of these two additional isomers.

The IR spectra shown in Figure 5.20 correspond to the individual isomers, as well the distribution of isomers at 298 K, of deprotonated glycine clustered to methanol. While most of the peaks of the individual isomer spectra are superimposed in the spectrum for the distribution of those isomers, a few stand out as unique to one particular isomer. Structure **5.6II** is predicted to possess an absorption peak at  $317\text{ cm}^{-1}$ , corresponding to a scissor mode with the  $\text{CH}_2$  group at the origin and the  $\text{NH}_2$  and  $\text{COO}$  groups defining the “arms” of the scissors. This vibration is found in **5.7III**, **IV** and **V**, but is red-shifted to 299, 298 and  $306\text{ cm}^{-1}$ , respectively, where they are no longer distinctly visible. A distinct pair of vibrations at 932 and  $935\text{ cm}^{-1}$  are predicted for structure **5.7III**, which correspond to proton vibrations in a direction perpendicular to the OHO bond it is contained within. The same proton vibrations can be found in **5.6II** and **5.7IV**, but are no longer distinct since they are red-shifted to 857 and  $881\text{ cm}^{-1}$ , and 861 and  $893\text{ cm}^{-1}$ , while in **5.7V** they are blue-shifted to 958 and  $994\text{ cm}^{-1}$ . It is also noted that these peaks are spaced much closer together for **5.7III**, compared to those observed for any of the other isomers. As in the case presented above for deprotonated glycine clustered to water, the OH vibration of methanol (the OH group

involved in the formation of the OHO bond) can be used to identify an isomer, in this case **5.7V**. A small, yet identifiable peak is predicted at  $3101\text{ cm}^{-1}$ , which is red-shifted in comparison to the same vibrational motion of the other isomers. In **5.6II**, **5.7III** and **IV** the OH vibration of methanol is predicted to be located at 3269, 3223 and  $3247\text{ cm}^{-1}$ , respectively, which are superimposed in the combined spectrum to give the most intense absorption. No single feature of the simulated spectra could be assigned for **5.7IV**.

For the isomerically-rich clustering system of deprotonated glycine with ethanol, a nondescript combined IR spectra is predicted, Figure 5.21. No uniquely identifying features are predicted which would allow for the discrimination of one particular isomer from another, but rather the spectrum could be described as a collection of broad peaks and shoulders, all resulting from the contributions from many isomers. It can, however, be pointed out that the axial OHO proton vibration is once again predicted to be the most intense peak and occurs in the vicinity of  $3200\text{ cm}^{-1}$ .

## 5.4 Conclusion

For the case of deprotonated glycine clustered to various protic solvents, it has been shown that a distribution of isomers within an HPMS ion source will affect the measured thermochemical properties. The manner in which a distribution of isomers impacts observable quantities ultimately depends on the thermochemical nature of each of the constituting isomers, and consequently, any shifts in their relative number density over a given temperature range. In the case of the attachment of ethanol to deprotonated glycine, significant amounts of nearly thermochemically-equivalent isomers were present, which

causes the observed entropy change to be  $11 \text{ J}\cdot\text{K}^{-1}\cdot\text{mol}^{-1}$  higher than that calculated for the formation of the lowest energy cluster, and a  $\Delta G_{298}^\circ$  value differing by  $2.6 \text{ kJ}\cdot\text{mol}^{-1}$ . By taking into account the presence of all significant isomers, the change in entropy value that is measured can be recreated to within  $\sim 1 \text{ J}\cdot\text{K}^{-1}\cdot\text{mol}^{-1}$  and  $\Delta G_{298}^\circ$  in almost exact agreement.

In the case of deprotonated glycine clustered with methanol, while fewer possible isomers exist, an even larger discrepancy between the measured change in entropy and that calculated for the lower energy isomer is observed. Upon closer inspection it becomes evident that a large shift in the isomeric distribution is expected to take place over the experimental temperature range. The consequence of this redistribution negates the guarantee that a comparison of the thermochemical properties of any one isomer would necessarily correlate with that experimentally measured. By taking all isomers into account the agreement between measured and calculated entropy change is improved from 15.4 to 0.5  $\text{J}\cdot\text{K}^{-1}\cdot\text{mol}^{-1}$ , while the agreement in  $\Delta G_{298}^\circ$  is improved from 4.2 to  $2.0 \text{ kJ}\cdot\text{mol}^{-1}$ , bringing the calculated value to within the error limits of the measured value.

Since the isomeric distribution of water, Figure 5.9A, can be characterized as consisting of one major isomer and a small number of less significant isomers (whose number densities are less than 30% of the most abundant isomer), it is no surprise that the measured thermochemical properties for this system have the best agreement to that of the lowest energy isomer, and nearly no change in the agreement between measured and calculated  $\Delta G_{298}^\circ$  is observed when all isomers were included in the analysis.

Measurement of the thermochemical properties of deprotonated alanine, valine and serine have been performed and agreement between the measured values and those calculated

for the most stable isomers of each system and, in general, good agreement could be observed for the changes in enthalpy and free energy, while poor agreement was observed in the change in entropy. Based on the observations made in the deprotonated glycine system, this is an indication of the presence of a distribution of isomers.

Several interesting observations were made when a more rigorous analysis of the thermochemical trends was performed. It was noted that the expected relationship between the free energy of clustering and the solvent acid strength was not observed. This was a result of water interacting with the deprotonated amino acids through two OH<sub>O</sub> hydrogen bonds, while methanol and ethanol interaction through one OH<sub>O</sub> and one CHO hydrogen bond. On the other hand, when the solvent was kept constant and a comparison of the free energy of clustering was made while the deprotonated amino acid was varied, the expected relationship was observed. That is to say that the negative of the free energy of clustering was directly proportional to the enthalpy of deprotonation of an amino acid.

As a further aid to the identification of the presence of a distribution of isomers, the IR spectra for the clustering of deprotonated glycine to water, methanol and ethanol were calculated. Several features of these spectra were identified as being a result of the presence of particular isomers. Should the IR spectra of this system be experimentally measured, a comparison to these simulated spectra would demonstrate the power of this technique to confirm the presence of different isomers.

## **Chapter 6**

### **Summary**

*"If I have perchance omitted anything more or less proper or necessary, I beg indulgence, since there is no one who is blameless and utterly provident in all things."*

- Leonardo (Fibonacci) de Pisa, in his book Liber Abbaci, 1202 a.d. -

By observing systems of  $\text{FHF}^-$ ,  $\text{NF}_2\text{H}\cdots\text{F}^-$  and  $[\text{M}-\text{H}]^-$  in equilibrium with various protic solvents, a wealth of information on the nature of strong charge-assisted hydrogen bonds has been obtained. Trends in hydrogen bond strength, length and angle have been analyzed as a function of the gas-phase acidity/basicity of the proton-donating/accepting moieties of a hydrogen-bonded complex. The effects of multiple bond formation and secondary interactions on the acidity and basicity of a bonding group, and in turn, the structural and energetic properties of the involved bonds, have also been demonstrated. In addition to observations of the specific trends of hydrogen bond properties, insight into the general thermochemical aspects of clusters and distributions of isomers, as measured by high pressure mass spectrometry, have been obtained.

One constant that can be observed throughout this thesis is the direct relationship between the gas-phase acidity and basicity of the  $\text{XH}$  and  $\text{Y}$  moieties involved in a hydrogen bond. Upon examination of the clustering of  $\text{FHF}^-$ , variations in the strength of the  $\text{FHF}$  and  $\text{FHO}$  hydrogen bonds were examined as a function of changes in the acid strength of  $\text{XH}$  (through competitive clustering), as well as through changes in the identity of  $\text{Y}$ . Upon inspection of calculated geometries, trends in the structural indicators of bond strength, namely  $r(\text{F-F})$ ,  $r(\text{F-O})$ ,  $r(\text{F-H})$ ,  $\angle \text{FHF}$  and  $\angle \text{OHF}$ , revealed the importance of considering all

interactions when using these properties as predictors of strength. This was evidenced by the observation that, upon clustering of  $\text{FHF}^-$  with ethanol, or a second molecule of any of the solvents, the competition for electron density between various bonds can alter the acid and base strength of  $\text{XH}$  and  $\text{Y}$ , thus altering the observed bond properties. In the study of fluoroamine-fluoride clusters, the relationship between acidity of  $\text{XH}$  and the strength of a hydrogen bond was demonstrated through a sequential fluorination process of the form  $\text{NF}_n\text{H}_{3-n}$ ,  $n=0, 1, 2$ . In this case, in the absence of perturbing secondary interactions, the relationship between acidity of the fluoroamine and  $\text{NFH}$  bond strength was clearly linear. Finally in the study of deprotonated amino acids this relationship was tested through R-group substitutions. As the gas phase acid strength of an amino acid increased, the general observation that was made was that hydrogen bonds formed to its deprotonated analogue would decrease in the expected fashion. As in the case of  $\text{FHF}^-$ , this trend was not distinctly linear in every case since the number of secondary interactions present within a system was a function of the complexity of the R group.

While the majority of this thesis focused on the observation of structural and thermochemical trends of hydrogen bonds, some interesting observations regarding the properties measured *via* PHPMS were also made. In particular, new insight into the effects associated with the presence of more than one isomer of an ion of interest was obtained. As discussed in Section 2.1, the thermochemical effect of a distribution of isomers can manifest itself in a number of ways. When one isomer is considerably more ergonomically favored than another, the measured thermochemical properties of that reaction will be dependent upon the properties of that particular isomer. This was observed in the case of two water molecules

bound to FHF<sup>-</sup>, where the measured thermochemical “fingerprint” clearly matched that of the ergonomically favored isomer, as opposed to the enthalpically favored species, which was present in significantly lower amounts. In this case, a strong entropic advantage associated with the formation of one particular isomer was responsible for governing the relative isomer distribution. This was not the only case in which entropy information proved to be valuable. In fact, in all systems examined, the deviation of the measured entropy value from that calculated for the ergonomically favored species could be used as an indication of the number of significant isomers present in an equilibrium mixture. In the example of glycine clustered to protic solvents, a thorough investigation of this effect was performed. By correctly accounting for the effects of other significant isomers, the percent difference between measured and calculated values for the change in entropy was improved by a little more than an order of magnitude. While this high level of attention to detail is undoubtedly precise, it is also resource demanding. However, when the identification or quantification of a distribution of isomers is necessary, this technique could prove to be an invaluable complement to other techniques such as IR or NMR spectroscopy.

## References

- (1) Hadzi, D.; Thompson, W. *The hydrogen bond*; Pergamon Press: London, 1959.
- (2) Pauling, L. *The Nature of the Chemical Bond and the Structure of Molecules and Crystals: An Introduction to Modern Structural Chemistry*; 3<sup>rd</sup> ed.; Cornell University Press: Ithaca, 1960.
- (3) Pimentel, G.; McClellan, A. *The hydrogen bond*; Freeman: San Francisco, 1960.
- (4) Vinogradov, S. N.; Linnel, R. H. *The hydrogen bond*; van Nostrand-Reinhold: New York, 1971.
- (5) Joesten, M. D.; Schaad, L. J. *Hydrogen bonding*; Marcel Dekker: New York, 1974.
- (6) Schuster, P.; Zundel, G.; Sandorfy, C. *The hydrogen bond. Recent developments in theory and experiments*; North Holland: Amsterdam, 1976.
- (7) Jeffrey, G. A.; Saenger, W. *Hydrogen Bonding in Biological Structures*; Springer-Verlag: Berlin, 1991.
- (8) *Modelling the hydrogen bond*; Smith, D. A., Ed.; American Chemical Society: Washington, 1994.
- (9) Hadzi, D. *Theoretical treatments of hydrogen bonding*; Wiley: Chichester, 1997.
- (10) Jeffrey, G. A. *An Introduction to Hydrogen Bonding*; Oxford University Press: New York, 1997.
- (11) Scheiner, S. *Hydrogen Bonding. A theoretical Perspective*; Oxford University Press: Oxford, 1997.
- (12) Del Bene, J. E. In *Encyclopedia of Computational Chemistry*; von Ragué Schleyer, P., Allinger, N. C., Clark, T., Gasteiger, J., Kollman, P. A., Schaeffer III, H. F., Schreiner, P. R., Eds.; John Wiley & Sons: Chichester, 1998, p 1263-1271.
- (13) Lii, J.-H. In *Encyclopedia of Computational Chemistry*; von Ragué Schleyer, P., Allinger, N. C., Clark, T., Gasteiger, J., Kollman, P. A., Schaeffer III, H. F., Schreiner, P. R., Eds.; John Wiley & Sons: Chichester, 1998, p 1271-1283.
- (14) Desiraju, G. R.; Steiner, T. *The weak hydrogen bond in structural chemistry and biology*; Oxford University Press: New York, 1999.
- (15) Desiraju, G. R. *Acc. Chem. Res.* **2002**, 35, 565.

- (16) Steiner, T. *Angew. Chem. Int. Ed.* **2002**, *41*.
- (17) Grabowski, S. *J. Phys. Org. Chem.* **2004**, *17*.
- (18) Dunitz, J. D.; Gavezzotti, A. *Angew. Chem. Int. Ed.* **2005**, *44*, 1766.
- (19) Grabowski, S. *Ann. Rep. Prog. Chem., Sect. C* **2006**, *102*, 131-165.
- (20) Wenthold, P. G.; Squires, R. R. *J. Phys. Chem.* **1995**, *99*, 2002-2005.
- (21) DeCorpo, J. J.; Steiger, R. P.; Franklin, J. L.; Margrave, J. L. *J. Chem. Phys.* **1969**, *53*, 936-939.
- (22) Yamdagni, R.; Kebarle, P. *J. Am. Chem. Soc.* **1971**, *93*, 7139-7143.
- (23) Mason, R. S.; Anderson, P. D. *J. Int. J. Mass Spectrom. Ion Processes* **1996**, *161*, L1-L6.
- (24) Kebarle, P. In *Techniques for the Study of Ion-Molecule Reactions*; Farrar, J. M., Saunders, W. H., Eds.; John Wiley & Sons, Inc.: New York, 1988; Vol. 20, p 221-286.
- (25) Pople, J. A. *Angew. Chem. Int. Ed.* **1999**, *38*, 1894-1902.
- (26) Kebarle, P.; Godbole, E. W. *J. Phys. Chem.* **1963**, *39*, 1131.
- (27) Kebarle, P. *Ann. Rev. Phys. Chem.* **1977**, *28*, 445.
- (28) Kebarle, P. *J. Mass Spectrom.* **1997**, *22*, 922.
- (29) McMahon, T. B. In *Energetics of Stable Molecules and Reactive Intermediates*; Minas de Piedade, M. E., Ed.; Kluwer Academic Publishers: Netherlands, 1999, p 259.
- (30) Meot-Ner, M.; Sieck, L. W. *J. Int. J. Mass Spectrom. Ion Processes* **1991**, *109*, 187.
- (31) Sunner, K.; Magnera, T. F.; Kebarle, P. *Can. J. Chem.* **1981**, *59*, 1787.
- (32) VG Gas Analysis Ltd: Cheshire England.
- (33) Hiraoka, K.; Kebarle, P. *J. Am. Chem. Soc.* **1976**, *98*, 6119-6125.
- (34) Sunner, J. A.; Hiraoka, K.; Kebarle, P. *J. Phys. Chem.* **1989**, *93*, 4010-4016.
- (35) Szulejko, J. E.; McMahon, T. B. *Org. Mass Spec.* **1993**, *28*, 1009-1015.

- (36) Norrman, K.; McMahon, T. B. *J. Am. Chem. Soc.* **1996**, *118*, 2449-2457.
- (37) Akroud, A.; Chikh, Z.; Djazi, F.; Elbannay, M.; Berruyer, F.; Bouchoux, G. *Int. J. Mass Spectrom.* **2007**, *267*, 63-80.
- (38) Albert, R. A.; Oppenheim, I. *J. Chem. Phys.* **1984**, *81*, 4603-4609.
- (39) Albert, R. A. *Ind. Eng. Chem. Fundam.* **1983**, *22*, 318-321.
- (40) Brinkley Jr., S. R. *J. Chem. Phys.* **1946**, *14*, 563-564.
- (41) Brinkley Jr., S. R. *J. Chem. Phys.* **1947**, *15*, 107-110.
- (42) Smith, B. D. *A.I.Ch.E.J.* **1959**, *5*, 26-28.
- (43) Dantzig, G. B.; DeHaven, J. C. *J. Chem. Phys.* **1962**, *36*, 2620-2627.
- (44) Duff, R. E.; Bauer, S. H. *J. Chem. Phys.* **1962**, *36*, 1754-1767.
- (45) Smith, W. R.; Missen, R. W. *Can. J. Chem. Eng.* **1974**, *52*, 280-282.
- (46) Frisch, M. J., *et al.* Gaussian, Inc. Wallingford CT, 2004.
- (47) Dennington II, R.; Keith, T.; Millam, J.; Eppinnett, K.; Hovell, W. L.; Gilliland, R.; Semichem, Inc: Shawnee Mission, KS, 2003.
- (48) Foresman, J. B.; Frisch, Ø. *Exploring Chemistry with Electronic Structure Methods*; Second ed.; Gaussian, Inc.: Pittsburgh, 1996.
- (49) Cremer, D. In *Encyclopedia of Computational Chemistry*; von Ragué Schleyer, P., Allinger, N. C., Clark, T., Gasteiger, J., Kollman, P. A., Schaeffer III, H. F., Schreiner, P. R., Eds.; John Wiley & Sons: Chichester, 1998, p 1706-1735.
- (50) Hu, C. H.; Chong, D. P. In *Encyclopedia of Computational Chemistry*; von Ragué Schleyer, P., Allinger, N. C., Clark, T., Gasteiger, J., Kollman, P. A., Schaeffer III, H. F., Schreiner, P. R., Eds.; John Wiley & Sons: Chichester, 1998, p 664-678.
- (51) Gill, P. M. W. In *Encyclopedia of Computational Chemistry*; von Ragué Schleyer, P., Allinger, N. C., Clark, T., Gasteiger, J., Kollman, P. A., Schaeffer III, H. F., Schreiner, P. R., Eds.; John Wiley & Sons: Chichester, 1998, p 678-689.
- (52) Parr, R. G.; Yang, W. *Density-Functional Theory of Atoms and Molecules*; Oxford University Press: Oxford, 1989.
- (53) Lee, C.; Yang, W.; Parr, R. G. *Phys. Rev. B* **1988**, *37*, 785-789.

- (54) Irikura, K. K. In *ACS Symposium Series 667. Computational Thermochemistry: Prediction and Estimation of Molecular Thermodynamics*; Irikura, K. K., Frurip, D. J., Eds.; American Chemical Society: Washington, 1998, p 402-417.
- (55) Jakubikova, E.; Rappe, A. K.; Bernstein, E. R. *J. Phys. Chem. A* **2006**, *110*, 9529-9541.
- (56) Blondel, C.; Delsart, C.; Goldfarb, F. *J. Phys. B. - Atomic and Molecular Optical Physics* **2001**, *34*, 281-288.
- (57) Ramond, T. M.; Davico, G. E.; Schwartz, R. L.; Lineberger, W. C. *J. Chem. Phys.* **2000**, *112*, 1158-1169.
- (58) Weis, P.; Kemper, P. R.; Bowers, M. T.; Xantheas, S. S. *J. Am. Chem. Soc.* **1999**, *121*, 3531-3532.
- (59) Larson, J. W.; McMahon, T. B. *J. Am. Chem. Soc.* **1983**, *105*, 2944-2950.
- (60) Larson, J. W.; McMahon, T. B. *J. Am. Chem. Soc.* **1983**, *105*, 2944-2950.
- (61) Rappe, A. K.; Bernstein, E. R. *J. Phys. Chem. A* **2000**, *104*, 6117-6128.
- (62) Chojnacki, H. *J. Molec. Struc.* **1997**, *404*, 83-85.
- (63) Platts, J. A.; Laidig, K. E. *J. Phys. Chem.* **1996**, *100*, 13455-13461.
- (64) Davidson, E. R. *Int. J. of Quant. Chem.* **2004**, *98*, 317-324.
- (65) Larson, J. W.; McMahon, T. B. *Inorg. Chem.* **1984**, *23*, 2029-2033.
- (66) Yamdagni, R.; Kebarle, P. *Can. J. Chem.* **1974**, *52*, 2449-2453.
- (67) Rauk, A.; Armstrong, D. A. *Int. J. of Quant. Chem.* **2003**, *95*, 683-696.
- (68) Kawaguchi, K.; Hirota, E. *J. Chem. Phys.* **1987**, *87*, 6838-6841.
- (69) Fridgen, T. D.; Zhang, X. K.; Parnis, J. M.; March, R. E. *J. Phys. Chem. A* **2000**, *104*, 3487.
- (70) Rasanen, M.; Seetula, J.; Kunttu, H. *J. Chem. Phys.* **1993**, *98*, 3914.
- (71) Frisch, M. J.; Del Bene, J. E.; Binkley, J. S.; SchaeferIII, H. F. *J. Chem. Phys.* **1986**, *84*, 2279-2289.
- (72) Pivonka, N. L.; Kaposta, C.; Brummer, M.; von Helden, G.; Meijer, G.; Woste, L.; Neumark, D. M.; Asmis, K. R. *J. Chem. Phys.* **2003**, *118*, 5275-5278.

- (73) Pivonka, N. L.; Kaposta, C.; von Helden, G.; Meijer, G.; Woste, L.; Neumark, D. M.; Asmis, K. R. *J. Chem. Phys.* **2002**, *117*, 6493-6499.
- (74) Elghobashi, N.; Gonzalez, L. *J. Chem. Phys.* **2006**, *124*, 1-12.
- (75) Ault, B. S. *Acc. Chem. Res.* **1982**, *15*, 103-109.
- (76) Gomez, H.; Meloni, G.; Madrid, J.; Neumark, D. M. *J. Chem. Phys.* **2003**, *119*, 872-879.
- (77) Kawaguchi, K. *J. Chem. Phys.* **1988**, *88*, 4186-4189.
- (78) Hamilton, I. P.; Li, G. P. *Chem. Phys. Lett.* **2003**, *381*, 623-627.
- (79) Li, G. P.; Hamilton, I. P. *Chem. Phys. Lett.* **2002**, *368*, 236-241.
- (80) Li, G. P.; Reinhart, B.; Hamilton, I. P. *J. Chem. Phys.* **2001**, *115*, 5883-5890.
- (81) Blondel, C.; Delsart, C.; Goldfarb, F. *J. Phys. B - Atomic Molecular And Optical Physics* **2001**, *34*, L281-L288.
- (82) Smith, J. R.; Kim, J. B.; Lineberger, W. C. *Phys. Rev. A* **1997**, *55*, 2036.
- (83) Lawton, E. A.; Weber, J. Q. *J. Am. Chem. Soc.* **1959**, *81*, 4755.
- (84) Hoffman, C. J.; Neville, R. G. *Chem. Rev.* **1962**, *62*, 1-18.
- (85) Lawton, E. A.; Weber, J. Q. *J. Am. Chem. Soc.* **1963**, *85*, 3595-3597.
- (86) Comeford, J. J.; Mann, D. E.; Schoen, L. J.; Lide Jr., D. R. *J. Chem. Phys.* **1963**, *38*, 461-463.
- (87) Lide Jr., D. R. *J. Phys. Chem.* **1963**, *38*, 456-460.
- (88) Colbourne, D.; Frost, D. C.; McDowell, C. A.; Westwood, N. P. C. *Chem. Phys. Letters* **1980**, *72*, 247-251.
- (89) Politzer, P.; Lane, P.; Grice, M. E.; Concha, M. C.; Redfern, P. C. *J. Mol. Struc. (Theochem)* **1995**, *338*, 249-256.
- (90) Ju, X.-H.; Xiao, H.-M. *Propellants, Explosives, Pyrotechnics* **2002**, *27*, 320-326.
- (91) Solimannejad, M.; Boutalib, A. *J. Chem. Phys. A* **2004**, *108*, 10342-10345.
- (92) DeTuri, V. F.; Ervin, K. M. *J. Phys. Chem. A* **1999**, *103*, 6911-6920.

- (93) Bartmess, J. E.; Scott, J. A.; McIver, R. T., Jr. *J. Am. Chem. Soc.* **1979**, *101*, 6046-6056.
- (94) Bogdanov, B.; Peschke, M.; Tonner, D. S.; Szulejko, J. E.; McMahon, T. B. *Int. J. Mass Spectrom.* **1999**, *185/186/187*, 707-725.
- (95) Koppel, I. A.; Taft, R. W.; Anvia, F.; Zhu, S.-Z.; Hu, L.-Q.; Sung, K.-S.; DesMarteau, D. D.; Yagupolskii, L. M.; Yagupolskii, Y. L.; Ignat'ev, N. V.; Kondratenko, N. V.; Volkonskii, A. Y.; Vlasov, V. M.; Notario, R.; Maria, P.-C. *J. Am. Chem. Soc.* **1994**, *116*, 3047-3057.
- (96) Ruckhaberle, N.; Lehmann, L.; Matejcik, S.; Illenberger, E.; Bouteiller, Y.; Periquet, V.; Museur, L.; Desfrancois, C.; Schermann, J.-P. *J. Phys. Chem. A* **1997**, *101*, 9942-9947.
- (97) Wickham-Jones, C. T.; Ervin, K. M.; Ellison, G. B.; Lineberger, W. C. *J. Chem. Phys.* **1989**, *91*, 2762.
- (98) Oxley, J. C.; Smith, J. L.; Zhang, J.; Bedford, C. *J. Phys. Chem. A* **2001**, *105*, 579-590.
- (99) Wenthold, P. G.; Squires, R. R. *J. Phys. Chem.* **1995**, *99*, 2002-2005.
- (100) Koppel, I.; Pikver, R.; Sugis, A.; Suurmaa, E.; Lippmaa, E. *Org. Reac.* **1981**, *18*, 3.
- (101) Graul, S. T.; M.E., S.; Squires, R. R. *Int. J. Mass Spectrom. Ion Proc.* **1990**, *96*, 181.
- (102) Demaison, J.; Margules, L.; Boggs, J. E. *Chemical Physics* **2000**, *260*, 65-81.
- (103) Albrecht, G.; Corey, R. B. *J. Am. Chem. Soc.* **1939**, *61*, 1087-1103.
- (104) Donohue, J. *J. Am. Chem. Soc.* **1950**, *72*, 949-953.
- (105) Levy, H. A.; Corey, R. B. *J. Am. Chem. Soc.* **1941**, *63*, 2095-2108.
- (106) Suenram, R. D.; Lovas, F. J. *J. of Mol. Spec.* **1978**, *72*, 372-382.
- (107) Basch, H.; Stevens, W. J. *Chem. Phys. Lett.* **1990**, *169*, 275-280.
- (108) Kish, M. M.; Ohanessian, G.; Wesdemiotis, C. *Int. J. Mass Spectrom.* **2003**, *227*, 590.
- (109) Wyttenbach, T.; Liu, D.; Bowers, M. T. *Int. J. Mass Spectrom.* **2005**, *240*, 221-232.
- (110) Jones, C. M.; Bernier, M.; Carson, E.; Coyler, K. E.; Metz, R.; Pawlow, A.; Wischow, E. D.; Webb, I.; Andriole, E. J.; Poutsma, J. C. *Int. J. Mass Spectrom.* **2007**, *267*, 54-62.

- (111) Blades, A. T.; Klassen, J. S.; Kebarle, P. *J. Am. Chem. Soc.* **1995**, *117*, 10563.
- (112) Meot-ner, M. *J. Am. Chem. Soc.* **1988**, *110*, 3854.
- (113) Meot-ner, M.; Sieck, L. W. *J. Am. Chem. Soc.* **1986**, *110*, 3854.
- (114) Taft, R. W.; Topsom, R. D. *Prog. Phys. Org. Chem.* **1987**, *16*, 1.
- (115) Topol, I. A.; Burt, S. K.; Russo, N.; Toscano, M. *J. Am. Soc. Mass Spectrom.* **1999**, *10*, 318-322.
- (116) Raspopov, S. A.; McMahon, T. B. *J. Mass Spectrom.* **2005**, *40*, 1536-1545.
- (117) Simon, A.; McMahon, T. B. *Int. J. Mass Spectrom.* **2006**, *255-256*, 301-311.
- (118) Wu, R.; McMahon, T. B. *Can. J. Chem.* **2005**, *83*, 1978-1993.
- (119) Wu, R.; McMahon, T. B. *J. Am. Chem. Soc.* **2007**, *129*, 569-580.
- (120) Locke, M. J.; McIver, R. T. J. *J. Am. Chem. Soc.* **1983**, *105*, 4226.
- (121) Caldwell, G.; Renneboog, R.; Kebarle, P. *Can. J. Chem.* **1989**, *67*, 661.
- (122) Markham, G. D.; Bock, C. L.; Bock, C. W. *Structural Chemistry* **1997**, *8*, 293-307.

## **Appendices**

## Appendix A: Sample GAUSSIAN Input Files

Optimization and frequency calculation at the B3LYP\6-311++G(d,p) level of theory:

```
%nproc=4
%mem=6Gb
# b3lyp/6-311++g(d,p) opt freq=noraman

Deprotonated glycine with water

-1 1
C          -0.67671440   -0.86160728    0.12928879
C           0.65182360   -0.04136828    0.00065279
H          -0.66671040   -1.32659828    1.12348779
H          -0.65810740   -1.68241628   -0.59369221
O           1.69549760   -0.72767628   -0.09485521
N          -1.92119940   -0.07860928   -0.02282821
H          -1.65693840    0.86468572    0.27097979
H          -2.10109940    0.02704972   -1.01855621
O           0.52435630    1.20992383    0.04053646
O           2.82578671    1.20601485   -0.13358471
H           2.75651599    0.24868466   -0.15148633
H           1.94891420    1.58939889   -0.05801168

1 2 1.0 3 1.0 4 1.0 6 1.0
2 5 2.0 9 2.0
3
4
5
6 7 1.0 8 1.0
7
8
9
10 11 1.0 12 1.0
11
12
```

Single Point Electronic Energy Calculation at the MP2(full)\6-311++G(d,p) level of theory:

```
%nproc=4
%mem=6Gb
# mp2(full)/6-311++g(d,p)

Deprotonated glycine with water

-1 1
C          -1.61435800   0.57322200  -0.10718400
C          -0.09357000   0.25457400  -0.03063000
H          -1.79345300   1.02157700  -1.09236900
H          -1.84891400   1.34784200   0.62793700
O           0.66771300   1.25000600   0.06259200
N          -2.52104500  -0.57561600   0.06766200
H          -2.02502700  -1.37120800  -0.33557300
H          -2.55613400  -0.79688900   1.05982700
O           0.22594300  -0.96261800  -0.10218700
O           3.02399900  -0.36845300   0.04457200
H           2.52508700   0.46959100   0.07837600
H           2.25208500  -0.95985400  -0.02476900

1 2 1.0 3 1.0 4 1.0 6 1.0
2 5 2.0 9 2.0
3
4
5
6 7 1.0 8 1.0
7
8
9
10 11 1.0 12 1.0
11
12
```

**Locating a Transition State at the B3LYP\6-311++G(d,p) level of theory:**

---

```
%nproc=4
%mem=6Gb
%chk=watertrans1.chk
# b3lyp/6-311++g(d,p) opt=(qst2, maxcycle=200, noeigentest) freq=noraman

deph2ob

-1 1
C          -1.61435800    0.57322200   -0.10718400
C          -0.09357000    0.25457400   -0.03063000
H          -1.79345300    1.02157700   -1.09236900
H          -1.84891400    1.34784200    0.62793700
O           0.66771300    1.25000600    0.06259200
N          -2.52104500   -0.57561600    0.06766200
H          -2.02502700   -1.37120800   -0.33557300
H          -2.55613400   -0.79688900    1.05982700
O           0.22594300   -0.96261800   -0.10218700
O           3.02399900   -0.36845300    0.04457200
H           2.52508700    0.46959100    0.07837600
H           2.25208500   -0.95985400   -0.02476900

deph2oe

-1 1
C          -0.77537700   -0.84772800    0.25476200
C          -0.35400400    0.63921500    0.05393100
H          -0.61731900   -1.08004900    1.31543100
H          -0.09325500   -1.49496400   -0.30294100
O           0.88847800    0.86732000    0.12307600
N          -2.17194800   -1.15855700   -0.10229300
H          -2.68333300   -0.28965200    0.06053100
H          -2.21855200   -1.28098200   -1.11078600
O           -1.27383800   1.46562000   -0.11881100
O           3.10527400   -0.62659800   -0.07684800
H           2.23069100   -0.16799500    0.06210900
H           3.60237600    0.02387700   -0.57978900
```

## Appendix B:

### MathCad Worksheet – Expected Observable Thermochemical Values for an Isomeric Distribution of a Cluster Ion

If you have calculated many different isomers for a particular cluster ion of interest and are wondering if their presence will be significant enough to alter your expected van't Hoff plot, then the following worksheet is for you!

Simply enter the calculated  $\Delta H$  and  $\Delta S$  values in the respective H and S matrices below, the desired temperature range, and the total number of isomers you have inputed. A plot will be generated that will best represent a van't Hoff plot (and corresponding x,y data points) that you would expect to measure in an HPMS experiment.

**Note to User:** Please only change information in the "Input" sections. The "Constants and Equations" sections are not to be played with. All important information is found within the "Output" sections and can be copied and pasted as much as you like. Enjoy!

**Hint:** Right-clicking on a table gives you the option to select all values within that table. Right-clicking again allows you to copy all of those selected values.

#### INPUT:

Desired Temperature Range (in Kelvin):

$$T_{\min} := 364.96$$

$$T_{\max} := 424.99$$

Number of isomers:

$$N := 4$$

Enter calculated changes in enthalpy (H) in kJ/mol and entropy (S) in J/mol-K for the formation of each isomer:

$$G := H - \frac{\left( T_{\max} + \frac{T_{\min} - T_{\min}}{2} \right) S}{1000}$$

	0
0	-71.401
1	-71.352
2	-66.09
3	-65.743
4	
5	
6	
7	
8	
9	
10	

	0
0	-120.888
1	-123.407
2	-105.29
3	-121.524
4	
5	
6	
7	
8	
9	
10	

$$G = \begin{pmatrix} -23.65287 \\ -22.60971 \\ -24.50333 \\ -17.74425 \end{pmatrix}$$

Constants and Equations:

$$R := 8.314510$$

$$T := T_{\min} \dots T_{\max}$$

$$i := 0 \dots (T_{\max} - T_{\min})$$

$$X_{\text{obs}}(T) := \sum_{i=0}^{N-1} e^{-\frac{H_{i,0} \cdot 1000}{R \cdot T} + \frac{S_{i,0}}{R}}$$

This formula calculates the observable quantity measured in HPMS (as a function of temperature)

$$x_i := \frac{1}{i + T_{\min}} \quad y_i := \ln\left(X_{\text{obs}}\left(\frac{1}{x_i}\right)\right)$$

Assigns  $1/T$  and  $\ln(X)$  to vectors for calculation of slope and intercept

$$\Delta H := -\frac{\text{slope}(x, y) \cdot R}{1000}$$

$$\Delta S := \text{intercept}(x, y) \cdot R$$

$$u_y := \max(y)$$

$$l_y := \min(y)$$

OUTPUT:

Data points for plot of  $\ln(K)$  vs.  $1/T$ :

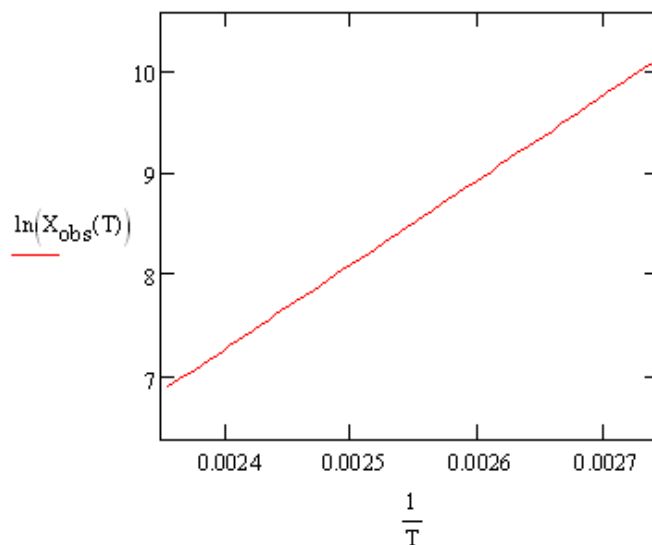
$$\frac{1}{T} =$$

0.00274
0.0027325
0.0027251
0.0027177
0.0027103
0.002703
0.0026957
0.0026885
0.0026813
0.0026741
0.002667

$$\ln(X_{\text{obs}}(T)) =$$

10.09071
10.02848
9.96659
9.90504
9.84383
9.78296
9.72242
9.66221
9.60233
9.54278
9.48355

Plot of  $\ln(K)$  versus  $1/T$ :



$$\text{intercept}(x, y) = -12.63226 \quad \text{slope}(x, y) = 8292.4953$$

$$\Delta H = -68.94804$$

$$\Delta S = -105.03106$$

Numbers to left represent expected measured  $\Delta H$  (kJ/mol) and  $\Delta S$  (J/mol-K) from a straight line fit to the above plot (i.e. if effect of different isomers is not taken into account)

$$\Delta G(T) := \Delta H - \frac{T \cdot \Delta S}{1000}$$

$$\Delta G(298) = -37.64878$$

## Appendix C:

### C++ Program Code – Extracting Infrared Frequencies and Intensities from a GAUSSIAN Output File

```
#include <iostream>
#include <fstream>
#include <string>
using namespace std;

int main () {
    string line;
    int f;
    char inputfile[50], outputfile[50];
    cout<<"Name of the Gaussian output file (with file extension):"<<"\n";
    cin.getline(inputfile,20);
    cout<<"Name for new file to be created (with file extension):"<<"\n";
    cin.getline(outputfile,20);
    cout<<"How many frequencies are there for this molecule/ion?:"<<"\n";
    cin>>f;

    char frequencies[f][15];
    char intensities[f][15];
    int i,j=0,l,m,n=0,o,p,q,r;
    ifstream myfile (inputfile);
    ofstream newfile (outputfile);

    for(q=0;q<f;q++)
    {
        for(r=0;r<15;r++)
        {
            frequencies[q][r]=' ';
            intensities[q][r]=' ';
        }
    }
}
```

```

if (myfile.is_open())
{
    while (! myfile.eof() )
    {
        getline (myfile,line);
        cout << line << endl;

if(line[1]=='F'&&line[2]=='r'&&line[3]=='e'&&line[4]=='q'&&line[5]=='u')
{
    for(i=15;i<28;i++)
    {
        frequencies[j][i-15]=line[i];
    }
    for(i=38;i<49;i++)
    {
        frequencies[j+1][i-38]=line[i];
    }
    for(i=61;i<72;i++)
    {
        frequencies[j+2][i-61]=line[i];
    }
    j=j+3;
}
if(line[1]=='I'&&line[2]=='R'&&line[3]==''
'&&line[4]=='I'&&line[5]=='n')
{
    for(m=15;m<27;m++)
    {
        intensities[n][m-15]=line[m];
    }
    for(m=38;m<49;m++)
    {
        intensities[n+1][m-38]=line[m];
    }
}

```

```

        for(m=61;m<72;m++)
        {
            intensities[n+2][m-61]=line[m];
        }
        n=n+3;
    }

}

newfile<<" Frequencies      Intensities"<<"\n";
for(l=0;l<f;l++)
{
    for(p=0;p<15;p++)
    {
        newfile<<frequencies[l][p];
    }

    newfile<<"\t";

    for(p=0;p<15;p++)
    {
        newfile<<intensities[l][p];
    }

    newfile<<"\n";
}

myfile.close();
}

else
{
    cout << "Unable to open file";
    newfile<<"Unable to open file";
}

return 0;
}

```

Screen shot from running program:

---

```
C:\Documents and Settings\Robbie\Desktop\frequencyextractor.exe
Name of the Gaussian output file <with file extension>:
meohdimerd.log
Name for new file to be created <with file extension>:
test1.txt
How many frequencies are there for this molecule/ion?:
39_-
```

Output file:

---

Frequencies	Intensities
2.8932	3.4607
13.7195	8.2221
18.6826	0.3103
20.8561	4.0151
31.7041	0.0175
91.0347	0.7187
92.2742	0.4140
129.3644	22.8822
134.4365	0.0062
234.1406	0.0219
244.0702	110.5769
638.6000	0.0038
841.0257	173.2837
841.9422	51.4601
1080.8257	151.9016
1081.4734	3.1354
1133.4077	82.0771
1135.7982	0.0090
1169.5757	0.3186
1169.5992	0.1877
1259.1668	140.4570
1316.7762	109.4011
1350.3619	3774.7582
1472.0511	0.0006
1476.2173	114.8902
1481.5327	0.0133
1481.7794	1.3753
1490.4666	0.2042
1492.9927	150.5837
1521.0801	0.2123
1522.3950	51.8268
2951.6544	3.9090
2952.2095	230.6981
2987.8061	22.6865
2988.2450	169.0186
3035.9636	220.3583
3036.4846	1.0649
3400.0766	1736.3019
3408.5989	4.6024

## Appendix D:

### MathCad Worksheet – Application of Lorentzian Line-Shape Function to the Vibrational Line Spectrum of a Single or Distribution of Isomers

This program simulates an IR vibrational spectrum collected for a gaseous sample consisting of a distribution of isomers. This program will take a series of line spectra and fit each peak with a Lorentzian line-shape function. It will weight each spectra according to the relative abundance of the corresponding isomer, and sum them together for a single spectrum.

INPUT: (Please update all of these fields)

Number of Isomers:  $N := 4$

Temperature:  $Temp := 298$

Full width at half maximum:  $v_{half} := 50$

Thermochemical Properties:  
(H goes in column 0 and  
S goes in column 1)

Thermo :=

	0	1
0	-71.401	-120.888
1	-66.09	-105.29
2	-71.352	-123.407
3	-65.743	-121.524

Copy and Paste the vibrational frequencies for the N isomers:  
(Each new isomer gets its own column)

Freq :=

	0	1	2	3
0	27.641	16.784	32.652	26.221
1	50.06	31.882	45.011	42.059
2	65.235	44.565	65.316	64.478
3	86.295	69.724	97.914	86.174

Copy and paste the IR Intensities for the N isomers:  
(make sure the Intensity information for a given isomer  
is in the same column as the corresponding frequency  
information above)

Intensity :=

	0	1	2	3
0	6.439	3.095	4.666	3.474
1	0.469	0.198	3.401	1.814

Constants and Equations: (Do not change)

---

Ideal Gas Constant:  $R := 8.3145$

range variable:  $r := 0..N - 1$

Gibbs Free energy at defined temperature:  $G_r := \text{Thermo}_{r,0} - \text{Temp} \cdot \frac{\text{Thermo}_{r,1}}{1000}$

This finds the free energy of the most stable isomer:

$$G_{ms} := \min(G)$$

Scale factor based on relative abundance of each isomer:

$$\text{Scale}_r := e^{-\frac{(G_r - G_{ms}) \cdot 1000}{R \cdot \text{Temp}}}$$

Number of Frequencies:

$$N_{freq} := \text{rows}(Freq)$$

Determine the maximum frequency and intensity:

$$\text{maxfreq} := \max(\text{submatrix}(Freq, 0, N_{freq} - 1, 0, 3))$$

$$\text{maxInt} := \max(\text{submatrix}(Intensity, 0, N_{freq} - 1, 0, 3))$$

Sets the frequency range:

$$\text{frequency} := 0, 1 .. \text{maxfreq} + 500$$

Sum of the separate isomer spectra constructed with Lorentzian line shape function, scaled for relative abundance:

$$\text{Lorentzian}(x) := \sum_{j=0}^{N-1} \sum_{i=0}^{N_{freq}-1} \left[ \frac{\left( \frac{v_{half}}{2 \cdot \pi} \right)^2}{\left( \frac{v_{half}}{2} \right)^2 + (x - Freq_{i,j})^2} \cdot \text{Intensity}_{i,j} \cdot \text{Scale}_j \right]$$

Individual spectrum for each isomer:

$$y(x, k) := \sum_{i=0}^{N_{freq}-1} \left[ \frac{\left( \frac{v_{half}}{2 \cdot \pi} \right)^2}{\left( \frac{v_{half}}{2} \right)^2 + (x - Freq_{i,k})^2} \cdot \text{Intensity}_{i,k} \cdot \text{Scale}_k \right]$$

Results:

Gibbs Free energy

$$G = \begin{pmatrix} -35.376 \\ -34.714 \\ -34.577 \\ -29.529 \end{pmatrix}$$

Gibbs free energy of most stable isomer:

$$G_{ms} = -35.376$$

Relative Abundance of each isomer:

$$\text{Scale} = \begin{pmatrix} 1 \\ 0.765 \\ 0.724 \\ 0.094 \end{pmatrix}$$

Number of Frequencies:

$$N_{freq} = 39$$

Maximum Frequency:

$$\text{maxfreq} = 3.539 \times 10^3$$

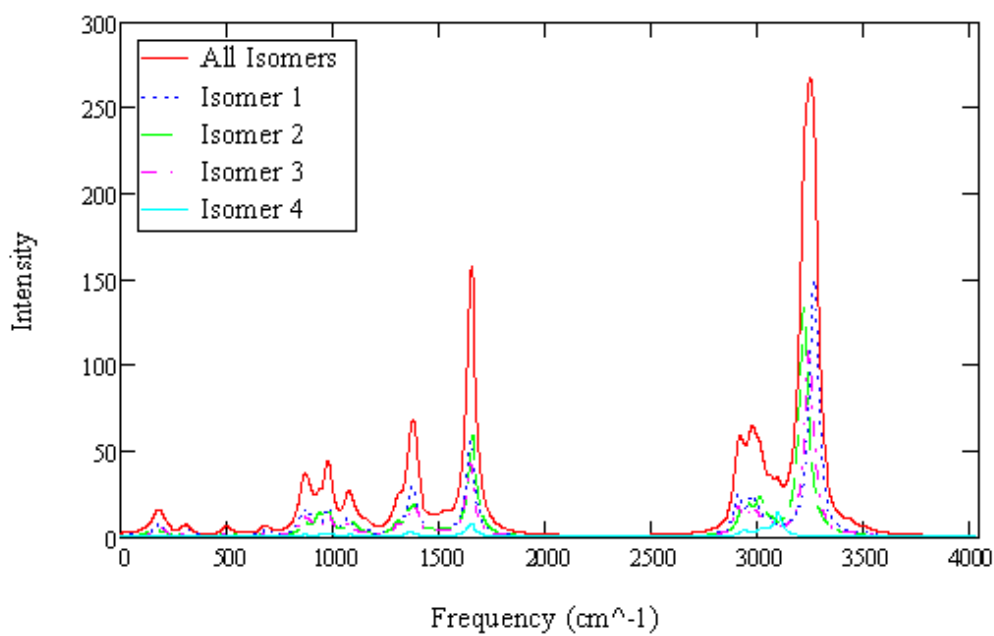
Maximum Intensity:

$$\text{maxInt} = 1.715 \times 10^3$$

X and Y data pairs for exporting the new fitted spectrum to your favorite plotting program:

frequency = Lorentzian(frequency) =

0	1.503
1	1.539
2	1.577
3	1.615
4	1.655



An example of a line spectrum superimposed onto Lorentzian fitted intensity profile for a single isomer:

